CHARACTERIZATION OF LIGHT-META STRUCTURE INTERACTIONS

by

Nitish Chandra

A dissertation submitted to the faculty of
The University of North Carolina at Charlotte
in partial fulfillment of the requirements
for the degree of Doctor of Philosophy in
Optical Science and Engineering

Charlotte

2018

Approved by:

Dr. Michael A. Fiddy

Dr. Glenn D. Boreman

Dr. Gregory J. Gbur

Dr. Tino Hofmann

Dr. Ryan Adams

ABSTRACT

NITISH CHANDRA. Characterization of Light-Meta Structure Interactions.
(Under the direction of DR. MICHAEL A. FIDDY)

The advent of metamaterials has increased the complexity of possible light-matter interactions, creating gaps in knowledge and violating various commonly used approximations and rendering some common mathematical frameworks incomplete. Our forward scattering experiments on metallic shells and cavities have created a need for a rigorous geometry-based analysis of scattering problems and more rigorous current distribution descriptions in the volume of the scattering object. In order to build an accurate understanding of these interactions, we have revisited the fundamentals of Maxwell's equations, electromagnetic potentials and boundary conditions to build a bottom-up geometry-based analysis of scattering. Individual structures or meta-atoms can be designed to localize the incident electromagnetic radiation in order to create a change in local constitutive parameters and possible nonlinear responses. Hence, in next generation engineered materials, an accurate determination of current distribution on the surface and in the structure's volume play an important role in describing and designing desired properties. Multipole expansions of the exact current distribution determined using principles of differential geometry provides an elegant way to study these local interactions of meta-atoms. The dynamics of the interactions can be studied using the behavior of the polarization and magnetization densities generated by localized current densities interacting with the electromagnetic potentials associated with the incident waves. The multipole method combined with propagation of electromagnetic potentials can be used to predict a large variety of linear and nonlinear physical phenomena. This has been demonstrated in experiments that enable the analog detection of sources placed at subwavelength separation by using time reversal of observed signals. Time reversal is accomplished by reversing the direction of the magnetic dipole in bianisotropic metasurfaces while simultaneously providing a method to reduce the losses often observed when light interacts with meta-structures.

ACKNOWLEDGEMENTS

- My thanks goes to my family for providing strong moral and financial support throughout my career.
- I would like to thank my friends for their company, moral support and help in times of bad health.
- I would like to thank Dr. Kedar B. Khare for helping me navigate through my undergraduate studies and providing general knowledge of process of research.
- My thanks goes to my advisor Dr. Michael A. Fiddy for giving me freedom to pursue my ideas during my PhD studies and insights into other aspects of research and professional life.
- I would also like to thank all the other committee members who have helped me throughout my research and help apply for funding.
- I would like to thank UNC Charlotte Graduate Assistant Support Plan (GASP) and Center for Metamaterials for providing financial support.

TABLE OF CONTENTS

LIST OF FIGURES ix

LIST OF TABLES xiii

LIST OF SYMBOLS xvii

CHAPTER 1: INTRODUCTION 1

CHAPTER 2: SCATTERING EXPERIMENTS 20

- 2.1. Experiments 21
  - 2.1.1. Spheres 23
  - 2.1.2. Multiple Scatterers 26
  - 2.1.3. Cylindrical Shells 28
  - 2.1.4. Inference of the Experiments 30
- 2.2. Skin Depth 32
- 2.3. Modal Analysis 34
- 2.4. Conclusions 56

CHAPTER 3: PROPAGATION OF POTENTIALS 61

- 3.1. Gauge Transformations 63
- 3.2. Boundary Conditions 66
- 3.3. Dyadic Green's Functions for Electromagnetic Potentials 69
- 3.4. Conclusions 78

CHAPTER 4: META ELECTRODYNAMICS 81

- 4.1. Distribution 83
  - 4.1.1. Multipolar Analysis 85

4.1.2. Skin Depth Engineering 95

4.1.3. Theory of Curves 95

4.1.4. Asymptotic Skin Depth Formulation 100

4.1.5. Physical Interpretation 111

4.2. Dynamics 112

4.2.1. Dynamical Variables 113

4.2.2. Lagrangian and Hamiltonian Formulations 116

4.2.3. Charge Coupled with External Fields 118

4.2.4. Power-Zienau-Woolley Transformation 119

4.3. Characterization of Interactions 122

4.4. Conclusions 124

CHAPTER 5: TIME REVERSAL USING META-MOLECULES 127

5.1. Time Reversal and Reciprocity 131

5.2. Role of Bianisotropy 133

5.3. Time Reversal using Bianisotropic Metastructures 136

5.4. Importance of Asymmetry 138

5.5. Conclusions 139

CHAPTER 6: CONCLUSIONS 140

6.1. Generalizability 144

6.2. Strong Non-Linearity 145

6.3. Sources 147

REFERENCES 150

APPENDIX A: CALCULATION OF TRADITIONAL SKIN DEPTH 160

APPENDIX B: MANIPULATION OF BESSEL FUNCTIONS 162

APPENDIX C: HELMHOLTZ THEOREM 167

APPENDIX D: LIST OF PUBLICATIONS 169

APPENDIX E: LIST OF PRESENTATIONS 170

LIST OF FIGURES

FIGURE 1.1: Primitive illustration of different types of scattering based on object size and incident wavelength without considering effects such as, absorption. 5

FIGURE 1.2: Building blocks of metamaterials 7

FIGURE 1.3: Various arrangements of meta-structures leading to different kinds of metamaterials. 7

FIGURE 1.4: Evolution of eigenmode: As the geometry of the meta-atom is changed the charge distribution changes which in turn changes the electric and magnetic dipoles asscociate with the structure. The geometry can be further tuned to produce higher multipole moments such as quadrupole. 14

FIGURE 2.1: Simplistic view of general scattering experiment illustrating approximate regions of forward and backward scattering where the red dots show the positions of detector. 21

FIGURE 2.2: Schematic of the setup used in the experiment. 22

FIGURE 2.3: Scattering patterns from spheres of varying sizes and evolution of diffraction lobes with the increase of radius of scattering objects from (a) to (c). 24

FIGURE 2.4: Scattering patterns from solid spheres. 25

FIGURE 2.5: Scattering patterns from golf ball. 26

FIGURE 2.6: Illustration of scattering from multiple scattering objects. 26

FIGURE 2.7: Scattering from multiple scattering objects. 27

FIGURE 2.8: The first setup in which the variation in scattering due to level of fills of liquid was measured. The shell was filled with water and the experiment was repeated several times. 28

FIGURE 2.9: Scattering patterns from cylindrical shells. 29

FIGURE 2.10: Diagram of the setup representing the distance and beam-size at the scattering object location. 30

FIGURE 2.11: Geometry of cylindrical shells. 35

FIGURE 2.12: Cylindrical shells with wall thickness = 500 μm. Blue curve represents the exact solution and orange curve shows approximate solutions. 49

FIGURE 2.13: Cylindrical shells with wall thickness = 100 μm. Blue curve represents the exact solution and orange curve shows approximate solutions.. 50

FIGURE 2.14: Cylindrical shells with wall thickness = 10 μm. Blue curve represents the exact solution and orange curve shows approximate solutions. 51

FIGURE 2.15: Tolerance to change in surrounding medium. 52

FIGURE 2.16: The change in number of resonant frequencies due to change in material inside but same surrounding medium. It is also important to note the values of penetration coefficients change by one and half order of magnitudes for empty and full shell. 53

FIGURE 2.17: The change in position of resonant frequencies due to change radius of the shells. 54

FIGURE 2.18: The penetration is enhanced when the resonance condition is satisfied at these discrete the zeros of the Bessel functions. 55

FIGURE 2.19: The variation in penetration frequencies due to material inside the shell. 57

FIGURE 2.20: Degrees of freedom for designing meta-atoms with responses at discrete frequencies. 58

FIGURE 2.21: Mixing of eigenfrequencies by adding the degree of freedom of angle of incidence. 59

FIGURE 2.22: Examples of other geometry which can be used to design meta-atoms. 60

FIGURE 3.1: Infinitesimal contour for surface integration. 67

FIGURE 3.2: Infinitesimal volume for volume integration. 67

FIGURE 3.3: Illustration of two semi-finite half spaces with source present in medium 1. 72

FIGURE 4.1: Coordinates for finite and continuous charge and current distributions. 86

FIGURE 4.2: Top: Distribution of discrete charge particles leading to dipole, quadrupole, octupole moments. Bottom: Illustration of modes of current distributions or eigen-modes in meta-atoms for multipole moments. 89

FIGURE 4.3: Constructive interference electric and magnetic dipole lead to zero back-scattering and destructive interference leads to zero forward scattering. Later cancellation of radiation pattern leads to a non radiative anapoles. 93

FIGURE 4.4: Parameterization of a curve. 96

FIGURE 4.5: Point P in three dimensional space. 98

FIGURE 4.6: Principal plane and principal curvatures. 100

FIGURE 4.7: Illustration of wavefronts and ray directions. 101

FIGURE 4.8: Illustration of arbitrary geometry of a conducting volume V represented by red. Surrounding dielectric with $\sigma = 0$, represented by gray. The black lines represents volume V_δ of current inside the conductor with thickness δ. Surface of the conductor S is the interface between conductor and dielectric and S_δ is the surface of the penetrated fields. 104

FIGURE 4.9: Pictorial summary of Meta-Electrodynamics. 126

FIGURE 5.1: Detection of scattered field. 128

FIGURE 5.2: Propagation of phase conjugated waves in reverse direction. 129

FIGURE 5.3: Illustration of the change in direction of magnetic dipole moment of meta-atoms under time reversal. The electric moment remains unchanged, hence to create two complimentary resonators or meta-atoms, the dipolar response should follow this scheme. 132

FIGURE 5.4: Schematic of the entire setup. A metasurface composed of bianisotropic scatterers placed in the near field of sources, the encoder. The field propagates and passes through a complimentary surface present in the near field of detector (the decoder) which reverses the multiple scattering events. 137

FIGURE 5.5: Illustration of electric and magnetic dipole moments in meta-atoms. The split resonator posses binanisotripic properties if the thickness of the ring increases. The half cut cylinder is shown to half reciprocal properties for dielectric meta-atoms. 138

FIGURE 5.6: Illustration of the setup and geometry of asymmetric meta-molecule with changing mode of current oscillations. 139

LIST OF TABLES

TABLE 4.1: Charge and current dependence of multipole Moments. 90

TABLE 4.2: Real and reciprocal representation of electromagnetic quantities. 114

LIST OF SYMBOLS

δ	Chapter 2 - Difference between real and imaginary part of wavenumber
δ	Chapter 4 - Distance inside conductor
$\rho(\mathbf{r}, t)$	Charge density
δ_s	Classical Skin Depth
$g_{\alpha\beta}$	Coefficient of metric tensor or fundamental form
σ	Conductivity
$\overleftrightarrow{\mathbb{C}}$	Constitutive matrix
ϵ^{ijk}	Contravariant Levi-Civeta matrix
D_α	Covariant derivative
$\mathbf{j}(\mathbf{r}, t)$	Current density
∇	Del operator
x_s	Dimensionless scattering parameter
$\overleftrightarrow{\xi}$	Electric cross-coupling tensor
$\mathbf{D}(\mathbf{r}, t)$	Electric Displacement
$\mathbf{E}(\mathbf{r}, t)$	Electric field vector
$\chi(\mathbf{r}, t)$	Gauge Function
K	Gaussian Curvature
$\psi_{pqs}(\mathbf{r})$	Generating Function
H	Hamiltonian

$\Im(\cdot)$	Imaginary part of a function
ω	Incident frequency
λ_0	Incident wavelength
$\mathbf{k}$	k - vector of reciprocal space
L	Lagrangian
$\overset{\leftrightarrow}{\zeta}$	Magnetic cross-coupling tensor
$\mathbf{H}(\mathbf{r},t)$	Magnetic field vector
$\mathbf{B}(\mathbf{r},t)$	Magnetic Induction
$\mathbf{M}(\mathbf{r},t)$	Magnetization density
H	Mean Curvature
Π	Momentum conjugate
$\mathbf{p}$	Momentum
$J_n(x)$	n-order Bessel function
$H_n^{(1)}(x)$	n-order Hankel function of first kind
$H_n^{(2)}(x)$	n-order Hankel function of second kind
$N_n(x)$	n-order Neumann function
$\Lambda_{pqs}^{L,M,N}$	Normalization constant of vector wavefunction
Δ_{TM}	Penetration Coefficient for TM waves
$\overset{\leftrightarrow}{\mu}$	Permeability tensor
$\overset{\leftrightarrow}{\epsilon}$	Permittivity tensor

$\mathbf{P}(\mathbf{r},t)$	Polarization density
a_s	Radius of scattering object
$\Re(\cdot)$	Real part of a function
$a_r^{M,N}$	Reflection coefficient of Green's function
ϵ_r	Relative permittivity
μ	Scalar permeability
ϵ	Scalar permittivity
$\Phi(\mathbf{r},t)$	Scalar Potential
$b_{\alpha\beta}$	Second fundamental form
$\mathbf{E}_{\Delta}^{c}(\mathbf{x})$	Series of electric field in conductor region
$\mathbf{E}_{\Delta}^{d}(\mathbf{x})$	Series of electric field in dielectric region
Δ	Small expansion parameter $\frac{\epsilon_0\omega}{\sigma(\omega)}$
$\overset{\leftrightarrow}{\mathbb{C}}(\mathbf{r})$	Spatially carying constitutive matrix
c	Speed of light
$\overset{\leftrightarrow}{\mathbb{T}}$	Tangential component for boundary condition
$\mathbf{R}_\alpha(x_\alpha)$	Tangential component of field in dielectric region
$\mathbf{r}$	Three dimensional position vector
$(\dot{-})$	Time derivative
$\mathcal{T}$	Time Reversal operator
t	Time

$a_t^{M,N}$	Transmission coefficient of Green's function
q	Unit charge
$\overset{\leftrightarrow}{\mathbb{G}}$	Unit dyadic
$\mathbf{A}(\mathbf{r}, t)$	Vector Potential
$\mathbf{L}_{pqs}(\mathbf{r})$	Vector wavefunction
$\mathbf{M}_{pqs}(\mathbf{r})$	Vector wavefunction
$\mathbf{N}_{pqs}(\mathbf{r})$	Vector wavefunction
$\overset{\leftrightarrow}{\mathbb{L}}$	Wave equation operator
k	Wavenumber

CHAPTER 1: INTRODUCTION

The study of origin and behavior of electric ($\mathbf{E}(\mathbf{r},t)$) and magnetic ($\mathbf{H}(\mathbf{r},t)$) field vectors underpins the investigation of interactions between electromagnetic waves and materials. In three dimensional vector notation, Maxwell's equations [1] provide a relationship between the field vectors, electric displacement ($\mathbf{D}(\mathbf{r},t)$), magnetic induction ($\mathbf{B}(\mathbf{r},t)$) and the current density ($\mathbf{j}(\mathbf{r},t)$) allowing a unique determination of field vectors from arbitrary current distribution.

$$\nabla \cdot \mathbf{D}(\mathbf{r},t) = \rho(\mathbf{r},t) \tag{1.1}$$

$$\nabla \cdot \mathbf{B}(\mathbf{r},t) = 0 \tag{1.2}$$

$$\nabla \times \mathbf{E}(\mathbf{r},t) + \frac{\partial}{\partial t}\mathbf{B}(\mathbf{r},t) = 0 \tag{1.3}$$

$$\nabla \times \mathbf{H}(\mathbf{r},t) - \frac{\partial}{\partial t}\mathbf{D}(\mathbf{r},t) = \mathbf{j}(\mathbf{r},t) \tag{1.4}$$

However, these equations have to supplemented with constitutive equations or material equations which describe the behavior of materials under the influence of fields.

$$\mathbf{D}(\mathbf{r},t) = \overset{\leftrightarrow}{\epsilon} \cdot \mathbf{E}(\mathbf{r},t) + \overset{\leftrightarrow}{\xi} \cdot \mathbf{H}(\mathbf{r},t) \tag{1.5}$$

$$\mathbf{B}(\mathbf{r},t) = \overset{\leftrightarrow}{\zeta} \cdot \mathbf{E}(\mathbf{r},t) + \overset{\leftrightarrow}{\mu} \cdot \mathbf{H}(\mathbf{r},t) \tag{1.6}$$

The nature of permittivity ($\overleftrightarrow{\epsilon}$), permeability ($\overleftrightarrow{\mu}$) and cross-coupling ($\overleftrightarrow{\xi}$ & $\overleftrightarrow{\zeta}$) tensors determine the response of materials to incident electromagnetic wave. For an isotropic medium, the permittivity and permeability are scalar quantities and cross-coupling terms are zero. Hence, the electric field vector is parallel to electric displacement and the magnetic field vector is parallel to magnetic induction. A material can be electrically anisotropic if the permittivity is a tensor quantity and permeability is a scalar then electric field vector may not be parallel to electric displacement and if permittivity is a scalar and permeability is a tensor quantity then magnetic field vector may not be parallel to magnetic induction rendering the material magnetically anisotropic. A material can be both electrically and magnetically anisotropic if the both permittivity and permeability are tensor quantities simultaneously and the cross-coupling terms are zero.

For isotropic and anisotropic materials, the constitutive relations relate both electric quantities and magnetic quantities to each other. However, a bianisotropic material provides cross coupling between the electric and magnetic fields as shown by constitutive relations (1.5 & 1.6) re-written as,

$$\begin{bmatrix} \mathbf{D} \\ \mathbf{B} \end{bmatrix} = \begin{bmatrix} \overleftrightarrow{\epsilon} & \overleftrightarrow{\xi} \\ \overleftrightarrow{\zeta} & \overleftrightarrow{\mu} \end{bmatrix} \begin{bmatrix} \mathbf{E} \\ \mathbf{H} \end{bmatrix} = \overleftrightarrow{\mathbb{C}} \begin{bmatrix} \mathbf{E} \\ \mathbf{H} \end{bmatrix} \tag{1.7}$$

The functional dependence of the constitutive matrix ($\overleftrightarrow{\mathbb{C}}$) determines the type of materials, if $\overleftrightarrow{\mathbb{C}}$ depends on field vectors then the material is nonlinear. If $\overleftrightarrow{\mathbb{C}}$ depends on spatial coordinates then medium is inhomogeneous and material is dispersive if $\overleftrightarrow{\mathbb{C}}$ depends on time derivatives [2].

The propagation of electromagnetic waves in vacuum or material medium is governed by wave equations which can be derived from the Maxwell's equations. For an isotropic, homogeneous and non-dispersive medium, the wave equation for electric and magnetic field vectors in presence of source current density is given by

$$\nabla \times \nabla \times \mathbf{E}(\mathbf{r}, t) + \epsilon\mu \frac{\partial^2}{\partial t^2}\mathbf{E}(\mathbf{r}, t) = -\mu \frac{\partial}{\partial t}\mathbf{j}(\mathbf{r}, t) \tag{1.8}$$

$$\nabla \times \nabla \times \mathbf{H}(\mathbf{r}, t) + \epsilon\mu \frac{\partial^2}{\partial t^2}\mathbf{H}(\mathbf{r}, t) = \nabla \times \mathbf{j}(\mathbf{r}, t) \tag{1.9}$$

Using the vector identity, $\nabla \times \nabla \times = \nabla(\nabla \cdot) - \nabla^2$ and equation 1.1, the wave equations describing the propagation of electric and magnetic field vectors originating from the source current and charge densities becomes,

$$\nabla^2\mathbf{E}(\mathbf{r}, t) - \epsilon\mu \frac{\partial^2}{\partial t^2}\mathbf{E}(\mathbf{r}, t) = \frac{1}{\epsilon}\nabla\rho(\mathbf{r}, t) + \mu \frac{\partial}{\partial t}\mathbf{j}(\mathbf{r}, t) \tag{1.10}$$

$$\nabla^2\mathbf{H}(\mathbf{r}, t) - \epsilon\mu \frac{\partial^2}{\partial t^2}\mathbf{H}(\mathbf{r}, t) = -\nabla \times \mathbf{j}(\mathbf{r}, t) \tag{1.11}$$

These equations can be simplified using the continuity equation which provides a relationship between charge and current densities.

$$\nabla \cdot \mathbf{j}(\mathbf{r}, t) + \frac{\partial}{\partial t}\rho(\mathbf{r}, t) = 0 \tag{1.12}$$

It is imperative to realize that the source current density has both space and time dependence, especially in the study of scattering from an object. Usually during calculations, the total fields observed are assumed to be the superposition of incident and scattered fields. The scattered field is calculated by assuming that the scattering object or scatterer acts as the source being driven by the incident fields. Boundary conditions are an essential piece of the puzzle for understanding the propagation of electromagnetic fields through an interface of two media. Using Gauss' and Stokes' theorem boundary conditions for tangential and normal components of the fields can be derived which has been discussed in detail in chapter 3. Boundary conditions play an important role in establishing the general coordinate system for scattering problems as they depend on the geometry of the boundaries. In the simplest case, a boundary can be a plane surface separating two semi-infinite media or much more complex bounded material such as spheres or cylinders. Quite often, the field inside the scattering object is not studied in detail as simplifying approximations such as perfect electrical conductors (PEC) and lossless dielectric medium are used.

In literature the overall size (a_s) of the scattering object relative to the incident wavelength (λ_0) is the main parameter that determines the type of scattering mechanism to study the interaction but geometry of the scattering object is ignored. The type of interactions can be described succinctly by a relative dimensionless scattering parameter which is defined as,

$$x_s = \frac{2\pi}{\lambda_0} a_s \tag{1.13}$$

If the size of the scattering object is much smaller than the incident wavelength or $x_s << 1$, then the interaction is characterized as Rayleigh scattering. Interaction with scattering objects with sizes comparable to the wavelength or $x_s \approx 1$ fall into the category of Mie scattering. The figure 1.1 gives examples of common objects and the category of the scattering depending on the wavelength of interacting fields. It is evident that the same object can fall into Rayleigh or Mie type scattering depending on the variation of the incident wavelength.

In order to solve the scattering problem boundary conditions have to be imposed on the scattering surface which requires continuity of tangential components of the electric and magnetic fields, assuming the surface current is zero. In general, closed form solution for scattering from arbitrary objects does not exist and fields are written in the integral form. However, scattering from simple geometries such as spheres or infinite solid cylinders can be analyzed analytically. Theoretical solution for scattering from spheres are widely known as Mie scattering because of the well known solutions published by Gustav Mie [3] which can be modified to analyze other dielec-

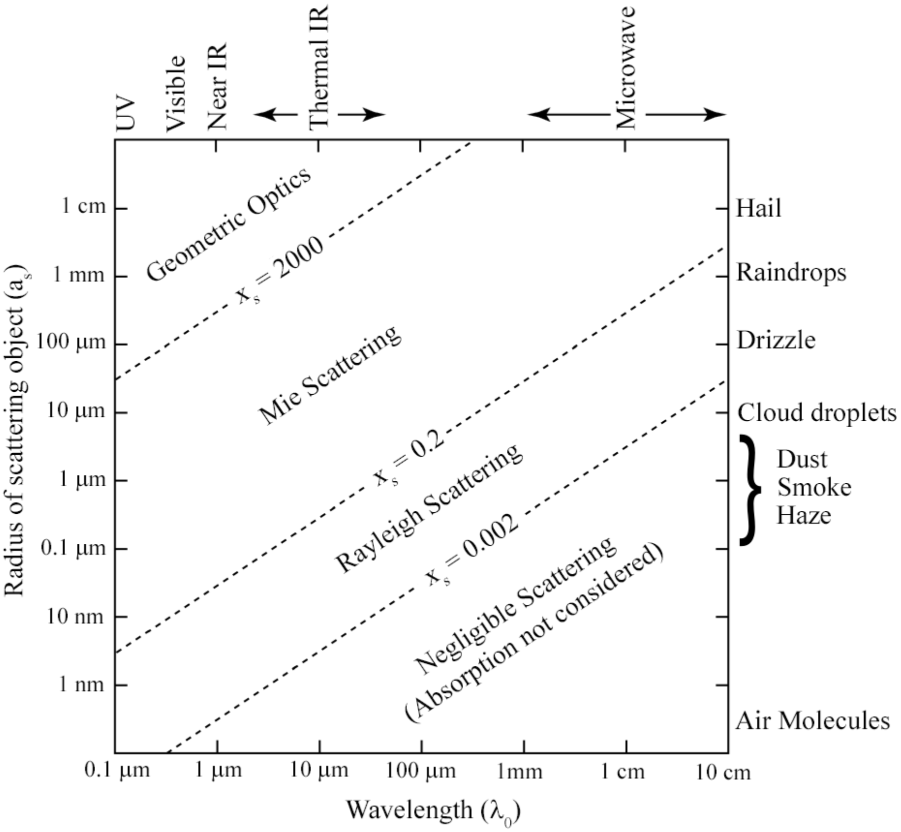

Figure 1.1: Primitive illustration of different types of scattering based on object size and incident wavelength without considering effects such as, absorption.

tric or conducting structures such as infinite solid cylinders. The formulation of the scattering problem can be simplified and generalized by using vector harmonics and electromagnetic potentials discussed in chapter 3.

The effects of geometry and nature of incident electromagnetic waves on scattering becomes very important for the study of metamaterials where the values of constitutive parameters can be engineered. The inception of the idea of negative constitutive parameters for materials can be credited to V. G. Veselago in 1968 [4], who first showed that the principles of electrodynamics do not restrict the permittivity (ϵ) and permeability (μ) to positive values. His work paved the path for the existence of left-handed materials where the permittivity and permeability values can be negative simultaneously. In the simplest case, the phase and group velocity in left handed materials are opposite to each other which was first discussed in 1904 [5]. The interest in negative refractive index was renewed by the research to increase the resolution of a lens and the theoretical evidence that negative index can produce a perfect lens [6]. The modern era of metamaterials was ushered by the first experimental evidence of negative index at microwave frequencies [7] and later at optical frequencies [8]. Similar to every new area of research metamaterials has peaked interest of a large section of the physics and electrical engineering community and a plethora of papers have followed presenting new applications of metamaterials.

The defination of metamaterial is still very vague but can be understood as materials possessing properties that are not available in natural materials such as strong response to magnetic fields at optical frequnecies [9], light trapping structures [10, 11] and slow light propagation [12]. The crucial role of resonances to achieve negative values of permittivity and permeability can be traced back to the work of N. A. Khizhnyzk [13]. Hence, the design of elementary components of metamaterials or meta-atoms (MA) which are essentially resonators to obtain a desired response is crucial to the study of metamaterials. The optimal size of the unit cell compared to the wavelength is still debatable and experiments have shown that the meta-atoms do not have be deeply subwavelength as initially percieved. With careful choice of the geometries of the resonators and material for meta-atoms macroscopic response to incident field can be tailored for specific applications such as negative refraction [14, 15], and optical cloaking [16]. The area of research has been extended to other optical phenomenon which can affect the off-diagonal elements of the constitutive tensor ($\overleftrightarrow{\xi}$ & $\overleftrightarrow{\zeta}$) to achieve optical activity [17], chirality induced negative index [18, 19], and amplification of evanescent waves [20, 21]. Despite the anticipated exotic properties of metamaterials, the design and characterization of these materials can be understood by studying the simple building blocks and thin mutual interactions as shown in figure 1.3. There are three main components to the study of metamaterials, material response ($\overleftrightarrow{\mathbb{C}}$) at operating frequency (ω), effects of geometry on the material response

$(\overset{\leftrightarrow}{\mathbb{C}}(\mathbf{r}))$ and interaction among neighboring meta-atoms or multiple scattering events. In addition, study of metamaterials requires understanding of effects of bandwidth and errors in fabrication to create meta-devices.

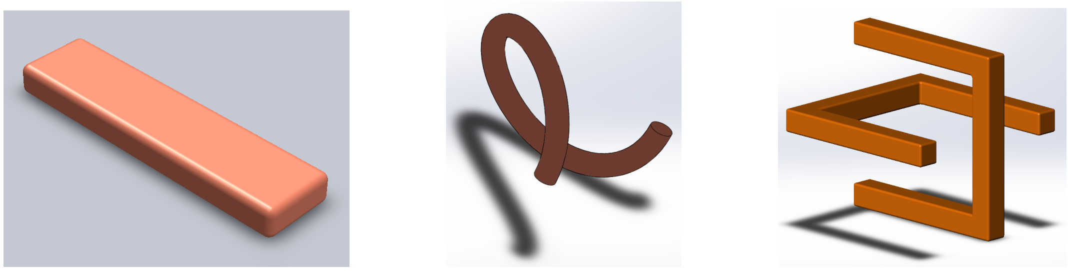

(a) Simple meta-atom (b) Complex meta-atom (c) Meta-molecule

Figure 1.2: Building blocks of metamaterials

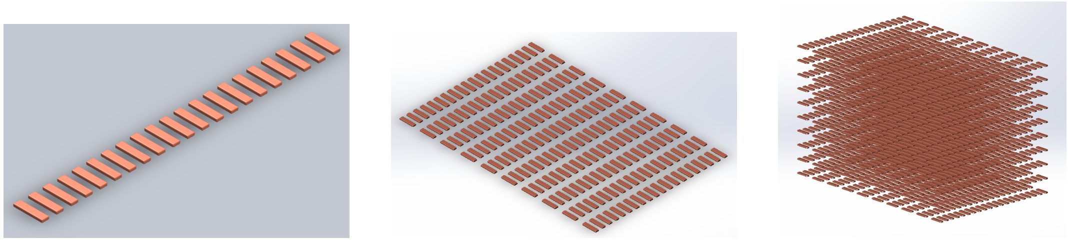

(a) Meta-chain (b) Meta-surface (c) Meta-material

Figure 1.3: Various arrangements of meta-structures leading to different kinds of metamaterials.

At the microscopic level metamaterials are composed of structures or resonators smaller or on order of the wavelength (meso-scale). These structures can be as simple as rods and can be termed as meta-atoms. The complexity of structures can be increased to achieve more exotic properties such as chiral and bianisotropic response to incident fields (see figure 1.2). These structures can be arranged one dimension to design a meta-chain and even though the structures are arranged in one dimension, the entire arrangement still has materials distributed in three dimensions interacting with the electromagnetic waves. Similarly, two dimensional arrangement is called a meta-surface and three dimensional structures are called meta-materials. The dimensionality in the analysis of these systems is very important in order to capture the effects of multiple scattering events on the phase and effects of geometry. The mathematical modeling of a meta-surface in two dimensions is not totally accurate because the meta-atoms may be arranged two dimensions but locally the the interaction occurs in three dimensions. Hence, in order to capture the effects of multiple scattering the modeling has to be done with consideration given to all three dimensions of a meta-atom with the limit of third dimension approaching to zero at the end of calculations as discussed in chapter 4.

The response of metamaterials composed of metallic meta-atoms is largely based on plasmon resonances supported by the structure. On application of electric field, conduction electrons are displaced from their equilibrium position causing polarization and the core ions creating a restoring force. Hence, applying a time varying field the motion can be modelled as Lorentzian oscillator with peak at resonance frequency with phase shift of π across the spectral width of the resonance. For small particles the electric field penetrates the whole volume of the meta-atoms, creating a complete dipolar response with resonant frequency depends on material, and the surrounding environment [22]. However, when the thickness of these structures becomes greater that skin depth the electric field is restricted primarily on the surface giving rise to multipole resonances making the response more sensitive to the geometry. Analytical results for spheres [3] and ellipsoid exists but other complicated shapes, especially shells are largely unexplored. Interesting physical phenomenon can be observed when two meta-atoms are brought closed to each other. The near field interactions can lead to creation of symmetric and asymmetric modes relative to the individual dipoles. The individual modes get altered by the presence of neighbors which alters the field distribution and hence affecting both electric and magnetic polarizabilities. The interaction can be classified in three categories, first the meta-atom separation is of the order of the resonance wavelength which leads to diffractive far-field interactions between the meta-atoms of the array and interfere constructively, leading to collective modes known as surface lattice resonances. Second, the meta-atom separation is smaller than the resonance wavelength, but meta-atoms are still sufficiently well separated that near-field-mediated interactions are small. Third, the meta-atom separation is small compared with the resonance wavelength and near-field interactions become very important. Modeling of these interactions becomes more complicated when the thickness of the meta-atoms are greater than skin depth which requires careful consideration of geometry for accurate calculation of interactions and field induced in the structures. The issue of skin depth in curved geometries is discussed in detail in chapter 4.

There is still an ambiguity about the best method for designing and characterizing metamaterials as the analysis becomes much more difficult near resonances. The excitation of resonances can be studied using circuit theory and can be modeled by LC resonances. There are few fundamental techniques for modeling such as, use of coupled dipole equations [23], and effective medium theory based on inclusions [24]. Transformation optics [25, 26] where the variation in refractive index $n(\mathbf{r})$ is represented as coordinate transformations is also used in design of metamaterials and invisibility cloaks. It provides a way to deal with electromagnetic waves bending in curved spaces but has certain limitations in the formalism such as permittivity and permeability values have to be equal $\epsilon = \mu$. We want to develop a much more robust method where the constitutive parameters are not restricted to certain values and can deal with presence of cross-coupling terms. Theoretical framework presented in this dissertation is inspired by experiments hence, extensive efforts have been made to relate the theory to the experimental observations.

The most common techniques used in metamaterial design are differential Maxwell's equation solvers such as finite difference time domain simulations [27], finite element methods and Fourier modal methods. Effective medium method where local interactions are averaged to calculate effective material parameters are often used to analyze metamaterials. It is assumed that the local interactions are static in nature and the spatial variation is negligible hence, it can be assumed to form a composite making the details of the structure insignificant. Green's functions can be used to solve for the fields originating from the current densities and hence, are capable of capturing the details of individual interactions. In the limited fundamental literature, Green's functions seem to be the thread that ties all the physical phenomenon with the geometry in the study of metamaterials. It provides an elegant way to model field distribution originating from meta-atoms and effects of meta-surfaces of arbitrary shape. It allows to encompass the vast variety of metamaterials being operated at radio-frequencies to quantum metamaterials in single formulations. Hence, Green's functions combined with effect of coupling should provide a good platform to charaterize the response of metamaterials from physical point of view. However, homogenization leads to loss of capability of engineering individually the local interaction for desired global response. Other techniques such as boundary layer method and dipole or multipole approximation methods are also used in metamaterial design. Despite the availability of variety of numerical techniques and software the analytical description of metamaterial design is still not well developed. There are recent publications [28, 29, 30] that point towards the need to develop a better physical understanding of metamaterials in order for the area of research to mature. There has been a growing uncertainty about the accuracy of finite element programs, such as COMSOL [31] to capture all physical phenomenon involved in interaction of meta-atoms with the incident field.

Currently, methods available are not capable of characterizing the whole range of interactions as the dynamical picture of interactions has not been studied and formulations for constitutive parameters based on geometry of structures are non-existent. The torrent of research published in the metamaterials area is largely dependent on software tools to understand the key components of the interaction. An analytical method for mapping structure to function is not available and mesh-dependent finite-element analysis by commercial software is typically used to understand the propagation properties of the problem. Various homogenization methods are used to simplify the computations, such as assuming an infinite lattice and approximating meta-atoms by dipoles averaged over the unit-cell volume [32, 33]. Multiple or recurrent scattering among adjacent meta-atoms are not considered in analytical models and the meta-atoms are assumed to be driven only by incident radiation. No fundamental limits have yet been determined for interactions depending on size and wavelength for metallic and dielectric meta-structures. These structures are considered two dimensional for numerical experiments when dimensions much smaller than the wavelength but physically interactions occur in three dimensions. Bianisotropic properties of structures are typically ignored in order to simplify the framework [34]. The current methodology has numerous limitations, since the different computation-based approaches have led to models approximately describing individual physical problem which are not generalizable. Current methods cannot be used for accurate analysis of bianisotropic structures or to decompose the interaction in to various modes of a multipole response. Effects of size and local surface curvature on power absorbed and emitted, and internal losses and collective effects have not been discussed. Methods for classification of different meta-structures and an overall framework relating all the local phenomena to an observed far-field response are not available. The study of non-linear effects is mostly perturbative in nature but recent work with anapoles [35], oligomers, and toroidal dipoles [36] have showed a path towards modeling strong non-linearities. Metamaterials have thus far been used as a way to manipulate waves but not as a source of radiation. There is lack of holistic methods for analyzing the entire 2D and 3D arrangements incorporating ensemble effects and localization of photons. The approach being built in this dissertation links observed far-field behavior to local resonant/non-resonant light-matter interaction. The main foundations of this multifaceted approach can lead to a classification hierarchy of structures that would be generally useful as a starting point in future analyses.

The advent of metamaterials has increased the complexity of the physics of light-matter interactions creating gaps in knowledge and violating various approximations making the usual mathematical frameworks incomplete. In order to build an accurate understanding of interactions it is necessary to revisit basic frameworks and build a bottom-up analysis of interactions. The individual structures or meta-atoms are designed to localize the incident electromagnetic radiation in order to create a change in local constitutive parameters. Thus, we develop a theoretical framework for the dynamics of the total system which consists of the incident electromagnetic field and the current distribution in meta-atoms. The localized current densities can interact with each other and alter the individual dynamics creating perturbation in global effective constitutive parameters for 2D and 3D arrangements of such meta-atoms. Precise calculation of such interactions can be analyzed by the change in dynamics on an individual meta-atom due to scattered field from adjacent structure. Such detailed description of dynamics of meta-atoms can be used to describe strong non-linear interactions and possibly a way to develop a metamaterial-based radiation source.

The majority of meta-atoms are metallic and the current induced in these structures plays a crucial role in accurate determination of scattered field. The traditional theory of skin depth may not be sufficient to explain the interaction when the size of meta-atoms becomes comparable to the operating wavelength and the thickness of the structures becomes deeply sub-wavelength. In the experiments conducted we have observed some abnormalities in the scattered field from cylindrical shells when the contents are altered which can be inferred as an effect of variations in skin depth. If we are able to excite Fabry-Perot type resonances then the transmission can be increased as evident in Fabry-Perot cavities. This raises a question about the effect of geometry in the distribution of current in conductors with finite conductivity. For ease of calculation in majority of the research, metals are assumed to have infinite conductivity but as we know from calculation of transmission in cavities a slight deviation from 100% reflectivity leads to a large transmission. Hence, similar resonant effects can lead to modification of the skin depth in finite conductivity calculations which opens the avenue for skin depth engineering. Modal analysis has shown the existence of resonances at certain frequencies but the analysis becomes increasingly cumbersome when the geometry becomes more complex which makes it imperative to develop a framework that capable of handling complex geometry using differential geometry. The wave equation in curvillinear coordinates provides a way to deal with propagation of electromagnetic waves through curved spaces and modifying the boundary conditions, a framework to deal with bounded spaces necessary for meta-atoms of arbitrary complexity is developed. Geometry introduces a non-linearity combined with evanescent fields and multi-pole response due to thickness to produce non-linear response. There have been papers showing that negative index can be achieved away from resonances by exploiting chirality and biansotropy. This can pave the path for low loss metamaterials for applications in time reversal and digital circuitry [37].

A simplistic views of light interactions with meta-structures can be understood by studying the eigenmodes supported by antennas which are used to convert localized current density or energy into electromagnetic radiation and *vice versa.* On the other hand, meta-atoms are designed to localize energy from an incoming electromagnetic field to alter the local effective material parameters as the waves propagates through the structures. The size of meta-atoms are dictated by the operating wavelength. At optical wavelengths a sufficiently long rod antenna can support fundamental half-wavelength eigenmode and higher-order modes when it is folded into more complex shapes, see figure 1.4. Deformations have two main effects: shift the resonance frequency due to modified dipolar interactions between the ends of the antenna, adding a degree of tunability, and change the symmetry of the antenna, so that formerly dark modes may couple to incident light for appropriate directions of the incident electric field. Such dipole formulation assumes that field penetrates the entire volume of meta-atoms. The skin effect can be included by using multi-pole approximations but still does not capture all physical phenomenon involved in interaction of field with the structures.

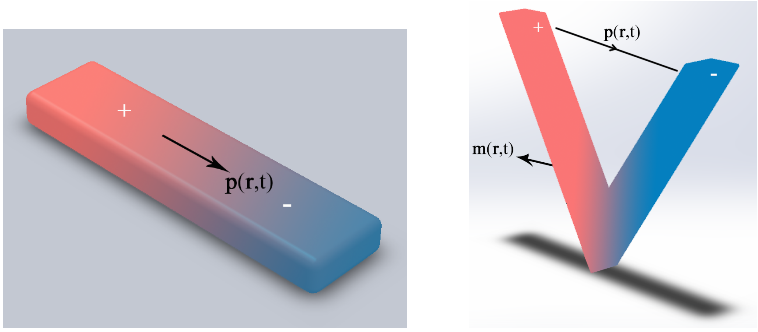

(a) Rod (b) V-shaped

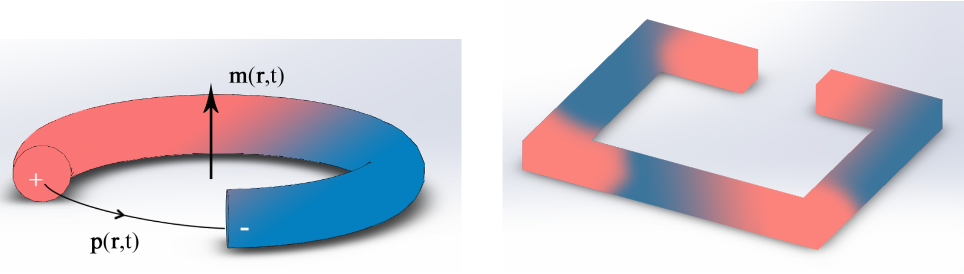

(c) Split ring (d) Split ring

Figure 1.4: Evolution of eigenmode: As the geometry of the meta-atom is changed the charge distribution changes which in turn changes the electric and magnetic dipoles asscociate with the structure. The geometry can be further tuned to produce higher multipole moments such as quadrupole.

The phase shift between the scattered and incident light in an antenna can be qualitatively studied by classifying the size of the antennas (l_a) (shown in figure 1.2a) with surface plasmon wavelength (λ_{sp}). If the antenna is very small ($l_a/\lambda_{sp} << 1$), then the charge distribution instantaneously follows the incident field ($\mathbf{E}_i(\mathbf{r}, t)$),

$$\rho(\mathbf{r}, t) \propto \mathbf{E}_i(\mathbf{r}, t) = \mathbf{E}_i(\mathbf{r}) e^{-i\omega t} \tag{1.14}$$

Hence, using Larmor formula [38], the scattered field ($\mathbf{E}_s(\mathbf{r},t)$) from the antenna is proportional to acceleration of charge density and it can be easily shown from equation 1.15 that the incident and scattered fields are π out of phase.

$$\mathbf{E}_s(\mathbf{r},t) \propto \frac{\partial^2 \rho(\mathbf{r},t)}{\partial t^2} \propto -\omega^2 \mathbf{E}_i(\mathbf{r},t) \tag{1.15}$$

With the increase in the size of antenna ($l_a/\lambda_{sp} \simeq 1/2$), the incident field is in phase with the current density ($\mathbf{j}(\mathbf{r},t)$) at the center of the antenna therefore drives the current most efficiently leading to maximum charge density at the ends of the antenna. Hence the scattered field derived from equation 1.16 is $\pi/2$ out of phase to the incident field.

$$\mathbf{E}_s(\mathbf{r},t) \propto \frac{\partial^2 \rho(\mathbf{r},t)}{\partial t^2} \propto \frac{\partial \mathbf{j}(\mathbf{r},t)}{\partial t} \propto -i\omega \mathbf{E}_i(\mathbf{r},t) \tag{1.16}$$

For long antenna with length of antenna is comparable to the surface plasmon wavelength ($l_a/\lambda_{sp} \simeq 1$) the antenna impedance is primarily inductive, hence the incident and scattered field are in phase.

$$\mathbf{E}_s(\mathbf{r},t) \propto \frac{\partial^2 \rho(\mathbf{r},t)}{\partial t^2} \propto \frac{\partial \mathbf{j}(\mathbf{r},t)}{\partial t} \propto \mathbf{E}_i(\mathbf{r},t) \tag{1.17}$$

Thus for fixed excitation wave, antenna impedance changes from capacitive to resistive to inductive as the size of the antenna changes leading to phase shift of $0 - \pi$. The problem of scattering becomes complex when the incident field does not penetrate the entire volume of the antenna and the charge density experiences force due to incident field and restoring force from the rest of charges.

These systems of oscillating charges can be modeled using Lorentz oscillator model. For analysis, consider localized charge density q of mass m, located at $x(t)$ at certain time t with spring constant k being driven by an incident electric field at frequency (ω) with damping coefficient Γ_i due to internal damping. The equation below shows the force equation in one dimension

$$m\frac{\partial^2\mathbf{x}(t)}{\partial t^2} + \Gamma_i\frac{\partial\mathbf{x}(t)}{\partial t} + k\mathbf{x}(t) = q\mathbf{E}_i(\mathbf{r})e^{-i\omega t} - \Gamma_s\frac{\partial^3\mathbf{x}(t)}{\partial t^3} \tag{1.18}$$

The charge density experiences an additional recoil force called Abraham - Lorentz or radiation reaction force [38] which reduces momentum by emitting radiation, where the force constant is given by $\Gamma_s = q^2/6\pi\epsilon_0 c^3$.

$$\mathbf{F}_s = -\Gamma_s\frac{\partial^3\mathbf{x}(t)}{\partial t^3} \tag{1.19}$$

If the motion of the charge density is harmonic in time $\mathbf{x}(\omega, t) = \mathbf{x}e^{i\omega t}$ where $\omega_0 = \sqrt{k/m}$, then we can control phase over a range of $0 - \pi$.

$$\mathbf{x}(\omega, t) = \frac{q}{m}\frac{\mathbf{E}_i}{(\omega_0^2 - \omega^2) + \frac{i\omega}{m}(\Gamma_a + \omega^2\Gamma_s)} \tag{1.20}$$

In order to obtain control over the entire range of $0 - 2\pi$ and give ability to control the polarization of the scattered field. This requires design of meta-atoms consisting of two independent oscillators oriented orthogonally, for example V-shaped or split ring meta-atoms, see figures 1.4b and 1.4c. But as the complexity of the meta-atoms increases the oscillator model becomes more complex because of increasing dimensionality of oscillators and imperfect penetration of the fields in the volume of meta-atoms.

We have developed a new method of characterizing light-matter-interactions where we determine accurate current distributions in a meta-atom described by multipole moments which are used to develop the model for multipole analysis of the interaction with incident radiation. Interaction between various structures arranged in two or three dimensions can be studied as a consequence of multiple scattering and appropriate approximations can be made to simply the problem based on weak and strong interactions. The dynamics of interactions can be studied by Lagrangian and

Hamiltonian formulations using charge distribution as the canonical variable and displacement field and scalar potential as conjugate momenta under the Power-Zienau-Woolley Transformation [39].

Building a bottom-up approach using principles of quantum electrodynamics helps understand interactions on a minutiae level and set fundamental limits on interactions using energy conservation principles. Introduction of metric tensor, Gaussian and mean curvatures provide a way to study interactions in three-dimensional structures which can be adapted for 2.5-dmesnisonal analysis by changing the metric tensor. Using these fundamental principles, we can analyze interactions of unit structures in metasurfaces and metamaterials. Strong scattering among these unit structures can lead to localization of electromagnetic energy, super- and sub-radiant modes of the ensemble which consequently affects the radiation/decay rate of meta-atoms which can only be accounted by this rigorous method. Studying the dependence of current distribution on curvature provides an opportunity for skin depth engineering in metallic and dielectric structures using curvature and multi-layered materials, respectively.

Decomposition of current densities into time- and space-dependent functions can be used to map structure to function and function to structure. The analysis of eigenmodes that are supported by the structure can be generalized by methods of differential geometry. This approach can be used to map structure to function and the inverse problem of mapping function to structure can be done by exploiting the presence of or lack of symmetry in a structures or ensemble by using group theory. This can form the basis of classification of response to incident radiation based on geometry of the structure [40]. This method can be adapted for metallic or dielectric meta-structures since functional forms for permittivity and permeability have been used for constructing the framework. The parameterization used for calculating the metric tensor of the structure can be changed based on the symmetry of the boundaries. The metric tensor can be defined such that one of the dimensions can be separated, enabling a simplified analysis of 2.5D structures as described in chapter 4.

The method developed is a completely new way to characterize and tailor the linear and non-linear properties of metamaterials where the interaction of incident light and structures expressed by the Lagrangian and Hamiltonian formalism with single dynamic variable with the units of charge. Current distribution in meta-structures of arbitrary geometries represented by multipole moments enabling the multipole expansion of scattered field and providing tools to tailor the collective response. This moves the state-of-the-art forward and away from computational and perturbative models for such interactions. Since the polarization density has a time and space dependent part the modes supported by the structure can directly be determined by eigenmodes corresponding to that geometry. The interaction between various modes can be leveraged to produce novel non-linear effects in materials. Exploiting the presence and lack of symmetry using group theory, inspired by classification molecules in chemistry, provides a way to classify meta-structures and maps observed function to structures.

The multipolar analysis of the interaction opens up an avenue for study of interaction between various modes in order to enhance second or higher order response. We study the effects of surface and bulk discontinuities for time reversal applications. The accurate analysis of multiple scattering can lead to identification of sub-radiant and super-radiant modes of the ensemble, which can be used to create bianisotropic metasurfaces where the reversal of magnetic dipoles can be used to achieve time reversal which is discussed in chapter 5.

This theoretical formalism combined with computational verification can open doors to modeling strong non-linearity and provide a way to move away from perturbative models for non-linear applications. Research has shown their advantages for non-linear applications [41] such as second harmonic generation by exploiting modal interactions. Even though it is not discussed in this work, investigation of the enhancement in magnitude of non-linear processes using epsilon-near-zero materials has been suggested in the literature [42]. The method developed here can be extended with the help of numerical experiments for wave mixing to demonstrate the extreme nonlinearity which can surpass the capabilities of perturbative models [43]. Treatment of meta-atoms as discrete entities can pave the way for design of metamaterial lasers, as certain eigenmodes in a structure can be excited by incident wavelength and the localized electromagnetic energy can in turn excite an eigenmode of a different geometry with gain medium and such composite geometry can be basic building block of lasers. Such hybrid nanoparticle architecture has already been used to demonstrate spaser-based nanolaser [44]. Hence, this bottom-up approach has clear advantage against present computational techniques, since it treats the individual meta-atoms with accurate current distributions and provides clear parameters that can be manipulated in an experiment to verify the method and engineer new properties.

CHAPTER 2: SCATTERING EXPERIMENTS

Theoretical study of scattering is arduous and often cannot be accomplished analytically, hence numerical methods along with experiments are used to analyze scattering from various structures. In practical situations, it is desirable to predict the geometry and composition of the scattering object. Extensive research has been done to solve the inverse problems [45] of obtaining the structure of objects from scattered field data. In general, inverse scattering problems can be divided into two categories depending on the interaction of waves with the scattering object namely, weak and strong scattering. Weak scattering occurs when the incident wave interacts with the object once and undergoes little perturbation as it propagates across the object. In this case, the field inside the scattering object can be approximated as incident waves and can help linearize the problem, which is exploited by Born and Rytov approximation methods to find a solution [46]. In these methods, it is often required that the material parameters or refractive index do not change rapidly on the scale of the wavelength. However, when the incident waves inside the scattering object scatters multiple times and significant perturbation occurs then the interaction is characterized as strong scattering and the formulation becomes nonlinear [47].

In a typical two dimensional scattering experiment there are fixed number of receivers or receiver locations around the center of the scattering object which measure the distribution of fields as a function of angle. In figure 2.1, the scattering object of volume $V(\mathbf{r})$ interacts with a plane wave propagating in $\mathbf{z}$ direction and the scattered field is captured by detectors placed at various locations. Ideally, the scattered field should be measured around the object but in practical situations the measured field is restricted to certain angles for both forward and backward scattering measurements.

The issue of incomplete data along with the issue of convergence and degenerate solutions make inverse problems extremely difficult to solve without linearizing approximations.

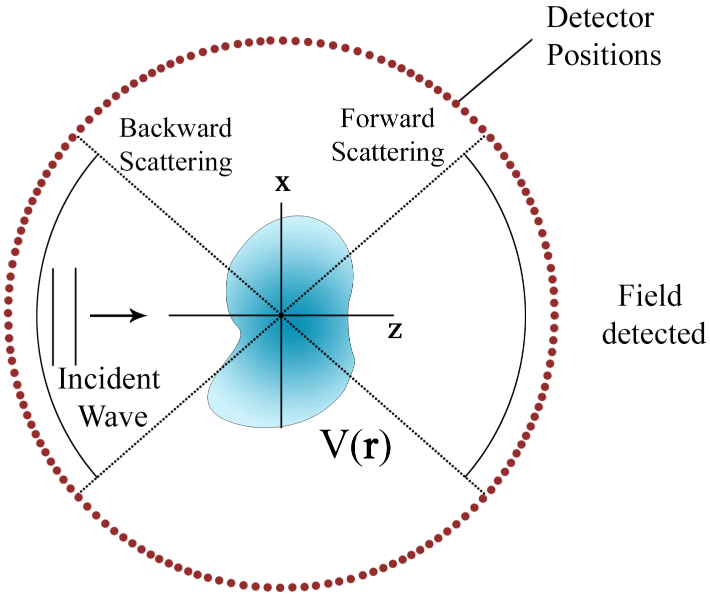

Figure 2.1: Simplistic view of general scattering experiment illustrating approximate regions of forward and backward scattering where the red dots show the positions of detector.

The complexity of the problem increases manifold when the scattering object size becomes comparable to the incident wavelength and the fields starts to interact with the object strongly. The internal fields can no longer be approximated as incident waves but has to be calculated precisely in order to explain the far field patterns at meso-scale. In this chapter, first we will discuss scattering experiments from various objects and then discuss in detail the issue of internal field for a metallic shell and enhancement in skin depth which can produce a large change in far field scattering pattern.

2.1 Experiments

In order to understand the effect of change in geometry on the far field scattering patterns, we have studied scattering patterns from various structures. A standard scattering experiment was performed using spheres, cylinders and other everyday objects as scatterers. Figure 2.2 shows the setup with a Gunn diode microwave source emitting at 10.5 GHz and the detector reading the values of scattered fields in mA during each scan which was later normalized with values without any scattering object. The scattering profiles of several metallic spheres and arrangements were studied. To study the nature of scattering from common objects such as metallic sphere, a concentric dielectric sphere and cylindrical metallic shells were used. The observed far field patterns matched with theoretical predictions for majority of the cases except, cylindrical metallic shells.

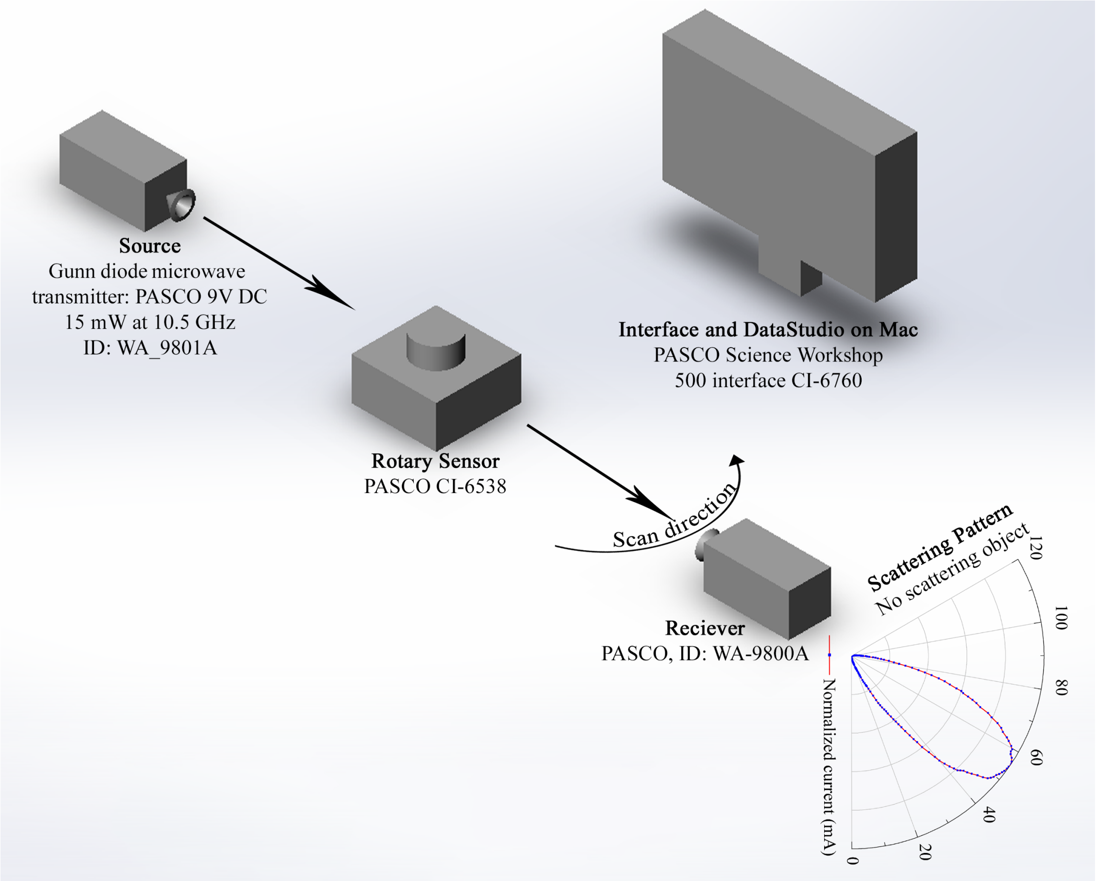

Figure 2.2: Schematic of the setup used in the experiment.

2.1.1 Spheres

The rigorous analysis of scattering from solid spheres with varying radius is described in Born and Wolf [48] hence, we will not discuss the formalism in detail here. In the case of spheres with high conductivity or high dielectric constant; most of the incident wave is scattered backwards or reflected. The intensity and polarization of scattered light depends on the direction of observation of scattering and on three physical quantities, incident wavelength (λ_0), radius of sphere (a_s) and the material parameters which is derived from Mie theory. In case of very small particles where the dimensionless scattering parameter $x_s \rightarrow 0$, the polar diagram of the intensity is maximum at angles of 0 and π with respect to incident waves and minimum at a plane perpendicular to the incident wave passing through the center of scattering object as shown in figure 2.3a. As the radius of sphere increases the symmetry of scattering pattern is broken and the field in forward direction increases which is termed as Mie effect. Increasing the radius of the sphere composed of finite conductivity or dielectric materials as compared to the incident wavelength the higher order scattering modes start to appear as side lobes as shown in figure 2.3c. In the case where the size of the scattering object becomes large as compared to the wavelength ($x_s >> 1$) then the interaction can be studied by geometrical optics.

First, spherical geometry was chosen for scattering experiments as exact solutions are well known and can be used to verify the accuracy and reliability of the experimental setup. The scattering profile of several spheres were measured and patterns from two spheres are shown in figure 2.4 to illustrate the evolution of scattering modes depending on the size of the sphere as expected by Mie type scattering object. Figure 2.4a shows scattering from a solid metallic sphere of diameter of 1.27 *cm* which corresponds to scattering parameter of $x_s = 1.4$ at the incident frequency of 10.5 GHz. Figure 2.4b shows scattering from a solid metallic sphere of diameter of 3.65 *cm*, corresponding to a scattering parameter of $x_s = 4$ at the same frequency. The intensity

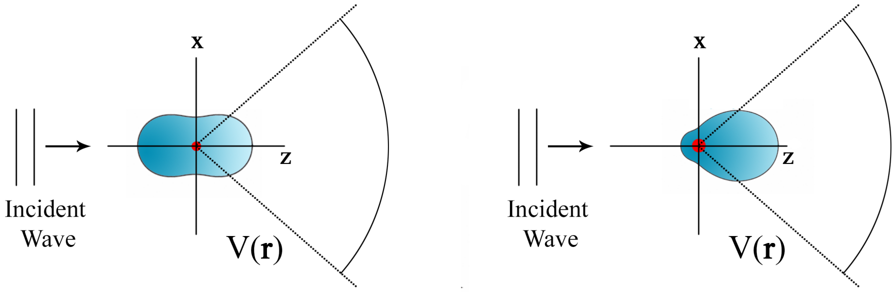

(a) Particle with very small scattering parameter ($x_s << 1$).

(b) Particle with small scattering parameter ($x_s < 1$).

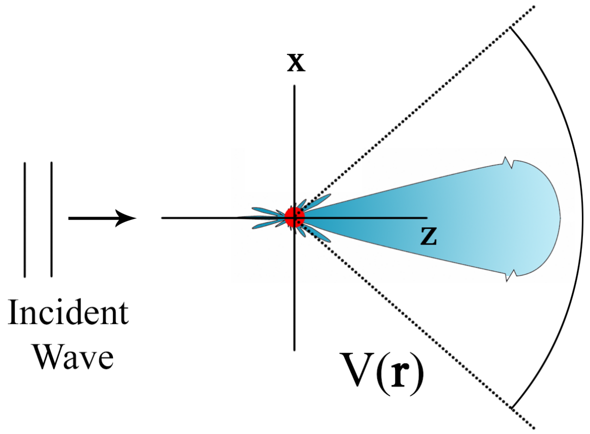

(c) Particle with greater scattering parameter ($x_s \approx 1$).

Figure 2.3: Scattering patterns from spheres of varying sizes and evolution of diffraction lobes with the increase of radius of scattering objects from (a) to (c).

profile of scattering vs angle from smaller sphere shows prominent forward scattering and higher order scattering modes are barely visible. On the other hand, for the sphere with greater radius intensity profile shows prominent forward scattering and much more pronounced higher order scattering modes.

After studying the test case of solid metallic sphere we moved on to dielectric spheres in order to study to effect of penetration of fields in the scattering volume. We have chosen common everyday spherical dielectric objects as we are interested in characterizing them from experimental scattered field data and combing it with existing inverse methods. In order to simulate a concentric dielectric sphere a golf ball was used. Figure 2.5 shows intensity distribution scattering from the golf ball of diameter

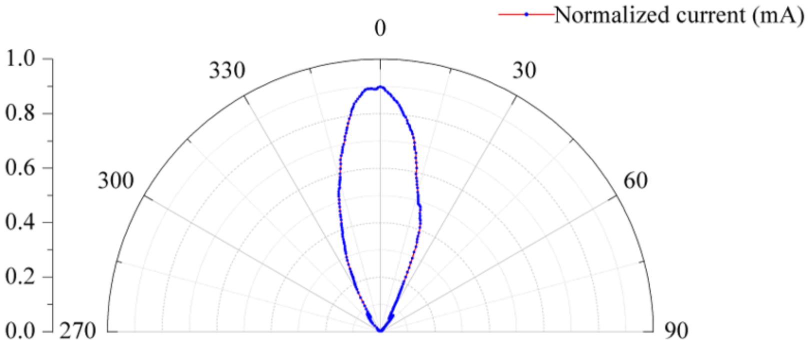

(a) Solid sphere of diameter 1.27cm.

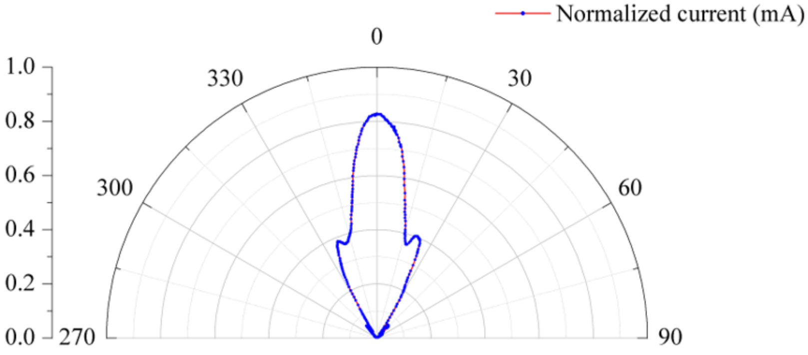

(b) Solid sphere of diameter 3.65cm.

Figure 2.4: Scattering patterns from solid spheres.

4.24 cm, scattering parameter $x_s = 4.66$. Even though there is a small increase in scattering parameter from the solid metallic sphere, the higher order scattering modes become dominant to the zeroth order forward mode. This can be attributed to the superposition of scattering from various concentric layers in the ball. We have also shown scattering from increasing larger dielectric spheres where the effects of increasing the radius becomes evident along with the displacement of scattering from the center of measuring arc translates into angular displacement of zeroth order mode.

The experiments performed on spheres have shown that the experimental setups produce accurate results and can be used to study other geometries and multiple objects.

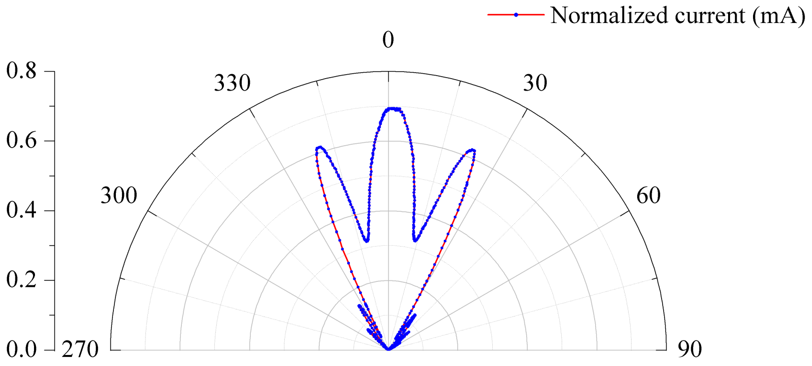

Figure 2.5: Scattering patterns from golf ball.

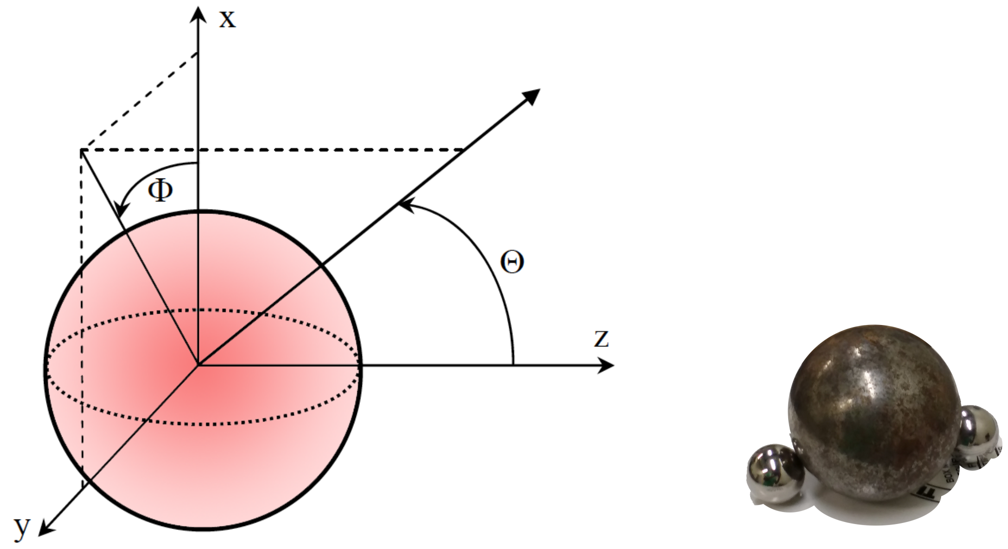

(a) Spherical scattering volume of radius equal to the scattering parameter.

(b) Image of an arrangement with three spheres placed in contact.

Figure 2.6: Illustration of scattering from multiple scattering objects.

2.1.2 Multiple Scatterers

In any scattering or imaging experiment the resolution is determined by incident wavelength which means that any features that are subwavelength cannot be resolved by traditional methods. Figure 2.6a illustrates an approximate spherical volume of radius x_s equal to the scattering parameter where determination of features of subwavelength size i.e. inside the volume of the sphere becomes ambiguous.

In order to verify this experimentally, we used combinations of spheres from previous experiment in various arrangements. It is well known that multiple scattering severly hampers the capability of reconstructing the object from scattered field because individual components cannot be viewed clearly and introduces nonlinearity in the inverse algorithms.

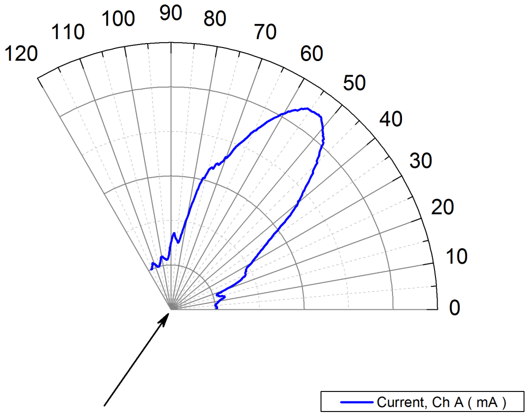

(a) Scattering from two spheres of radius 1.27cm in contact with each other.

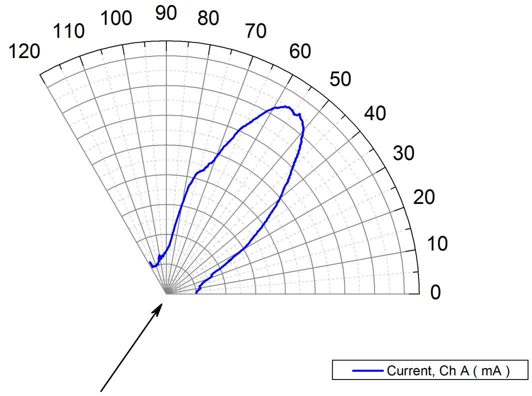

(b) Scattering from spheres of radius 1.27cm placed $\lambda/2$ apart.

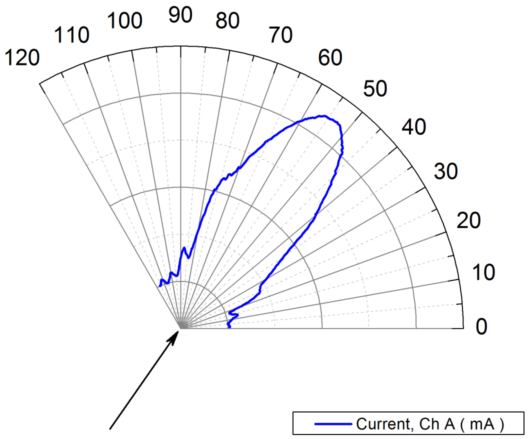

(c) Scattering from spheres of radius 1.27cm placed λ apart.

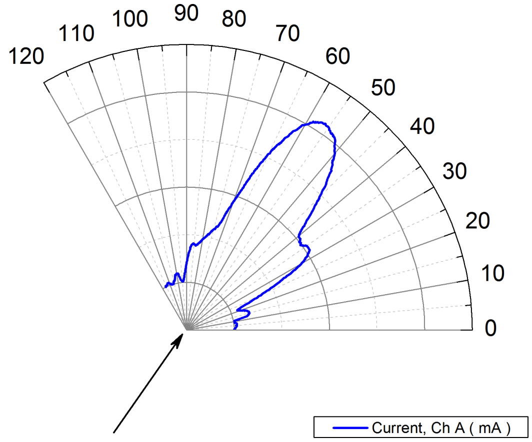

(d) Scattering from two spheres of radius 1.27cm and one sphere of radius 3.65cm in contact, as shown in figure 2.6b.

Figure 2.7: Scattering from multiple scattering objects.

It is evident from the figures 2.7a, 2.7b, 2.7c and 2.7d that scattering profile is very similar to single sphere case. It very difficult to tell the number and position of spheres involved in the process just from visual inspection of scattering pattern. This coincides with the theoretical predictions that multiple scattering from similar objects destroys the information about the arrangement of the object. The entire object behaves as an overall sphere composed of individual elements and the information about subwavelength features is lost. From figure 2.7d, we can see a pronounced side lobe with is due to the loss of symmetry in the setup due to displacement of smaller spheres when larger sphere is placed. The multiple scattering is now evident from the ambiguity in intensity profiles but gives an indication of the object arrangement. The experiments performed show an excellent agreement with theoretical predictions and prove that the setup built and it is configuration with respect to the laboratory can be relied for other scattering experiments.

2.1.3 Cylindrical Shells

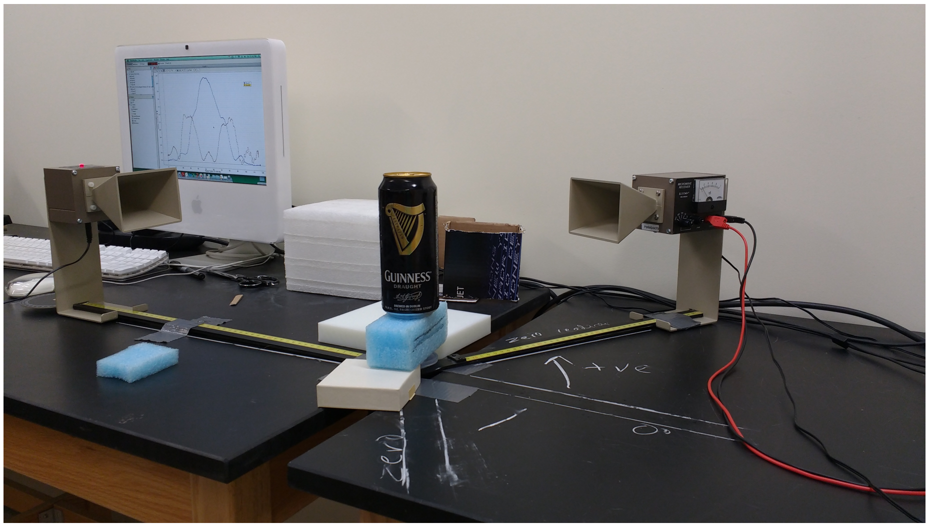

Figure 2.8: The first setup in which the variation in scattering due to level of fills of liquid was measured. The shell was filled with water and the experiment was repeated several times.

In order to study the effects of removal of the overall symmetry of scattering from spherical objects we started to study cylindrical objects. Scattering from cylinders is also well studied analytically but generally under the assumption of infinitely long solid cylinders and perfect conductivity in case of metallic cylinders. In our experiments, we have used cylindrical shells of finite length and radius comparable to the wavelength. Different right circular cylindrical shells (shown in figure 2.8) such as, unopened (sealed), opened, and top cut off with different fill levels of liquid inside the shell were used and results obtained did not match the theoretical predictions. The diameter of the cylinders was 6.6 *cm* and height 15.72 *cm*, corresponding to scattering parameters of $x_r = 7.25$ and $x_l = 17.33$, hence the interaction can be characterized as strong Mie scattering. Scattering patterns from such cylindrical shells have been presented in figure 2.9. The angular position of nodes for the scattering pattern coincides with the theoretical calculations. But when the liquid inside the shell is changed or the quantity is varied the scattering pattern changes as can be seen from figures 2.9a and 2.9b. The value of the zeroth order scattering mode decreases when the shell is full indicating absorption and the first order diffracted beam increases indicating a redirection of energy.

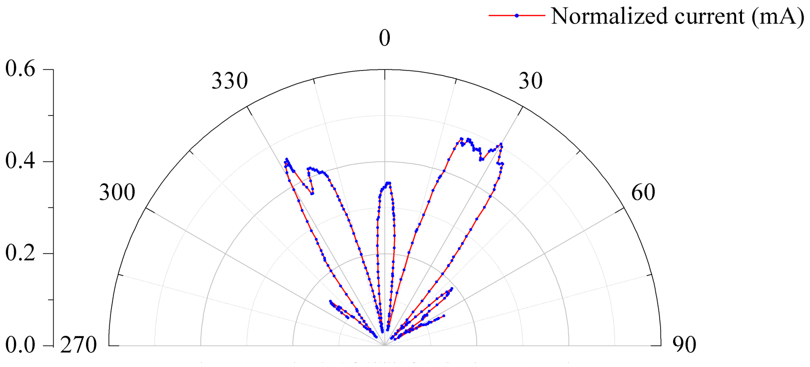

(a) Empty cylindrical shell.

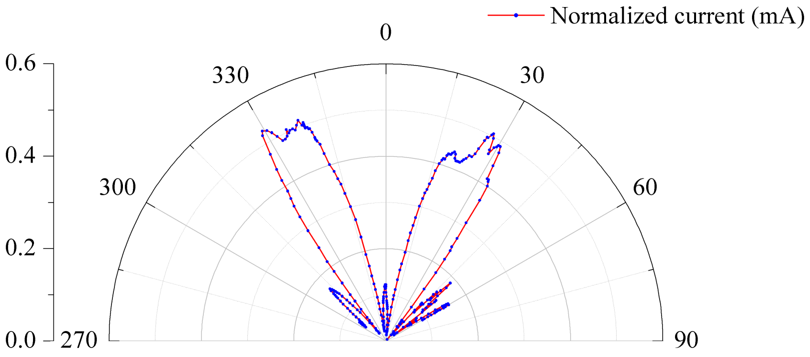

(b) Full cylindrical shell.

Figure 2.9: Scattering patterns from cylindrical shells.

The area under the curve representing the total energy in the scattered fields is greater in the case of empty shell than the shell filled with liquids which can be interpreted as absorption by the liquid. The issue of waves creeping in the shell from the top was resolved by performing experiments on a half filled sealed shell which produced same pattern as half filled taped shell. The experiment was repeated multiple times and same results were obtained which eliminates issues of setup errors.

2.1.4 Inference of the Experiments

The angular vertical and horizontal beamwidth is obtained by

$$\begin{aligned} \phi_v^\circ &= \frac{51\lambda_0}{b} \\ \phi_h^\circ &= \frac{70\lambda_0}{a} \end{aligned} \tag{2.1}$$

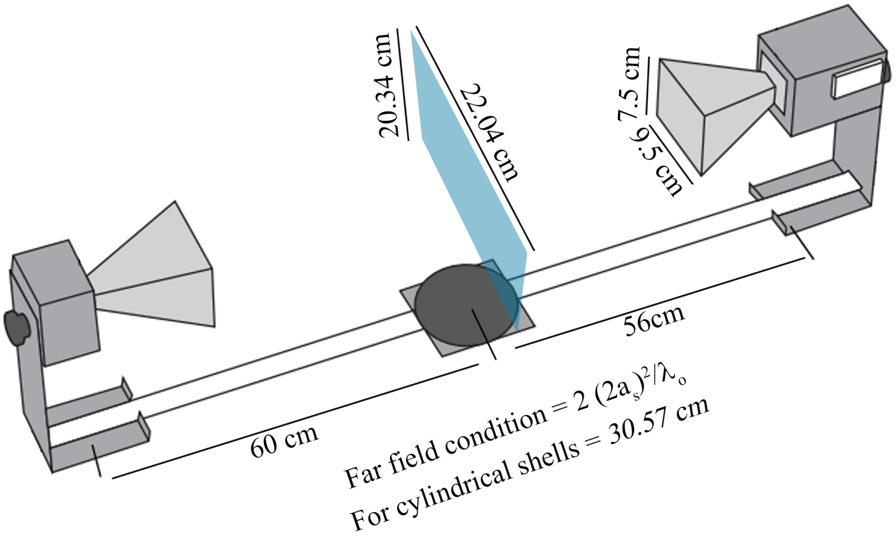

Figure 2.10: Diagram of the setup representing the distance and beam-size at the scattering object location.

The change in the scattering pattern due to change in the contents of the cylindrical shell can be attributed to penetration of fields deeper than skin depth. The wall thickness of the shells are 500 μm and it is composed of an aluminum alloy $Al6061$ with conductivity of 3.57×10^7 $Siemens/m$. It is well known that when an electromagnetic wave is incident on metals, its penetration is limited to the material's skin depth, hence providing some degree of shielding the contents inside the shell. The depth of penetration or skin depth is defined as (see Appendix A for derivation)

$$\delta_s = \sqrt{\frac{2}{\sigma\mu\omega}} \tag{2.2}$$

Skin depth formula is calculated assuming conductor in semi-infinite half plane and substituting the material parameters gives the skin depth 2 μm. Skin depth decreases as frequency increases due to shielding from metallic objects. However, it is known that Fabry-Perot resonances cause increased transmission in conducting plates thicker than the classical skin depth. Similar resonant behavior can be expected for the cylindrical conducting shells. Shells were filled with water up to various levels, hence the entire system is not symmetric which can enhance Fabry-Perot like transmission via frustrated total internal reflection which has been studied in great detail later in the chapter.

The geometry of the cylindrical shell is an important factor in possible perturbation of the penetration of electromagnetic fields. Both radius and length of the cylinders are the order of wavelength making it imperative to solve the full wave problem. The curvature of a scattering structure now becomes important in exciting surface currents. It is clear from a deeper review of literature that the exact solution of the skin effect problem depends on shape of conductor and nature of excitation [49]. The surface currents generated by the incident field can generate additional surface currents which can be represented by series of non interacting basis functions which are independent of each other. For a given geometry, two or more of these propagating and possibly counter propagating currents can be shown to combine leading to enhanced penetration of the scattering structure. The finite length of shells used in the experiments makes the analysis a 3D scattering problem. The solution for the fields and complete description of scattered field requires the calculation of the Green's function. The use of potentials instead of fields makes the calculations easier which has been discussed in chapter 3. In the next section, rigorous calculation has been used to corroborate initial results of resonance induced transmission and the effect of geometry on scattering.

2.2 Skin Depth

Maxwell discovered that the voltage required to force a time varying current through a wire increases more than could be explained by inductive reactance. He explained this phenomenon as being caused by a departure from uniform current density on the surface [50]. The depth of penetration is defined as the depth at which the current density (or magnetic flux) is attenuated by 1 Napier (in the ratio $1/e = 1/2.72$, or -8.7 decibels). At the same depth, its phase lags by 1 radian, so δ_s is $1/2\pi$ wavelength or 1 radian length in terms of the wave propagation in the conductor. This study of this effect was followed up by Heaviside, Rayleigh and Kelvin and came to be known as skin depth because the current is concentrated in the outer surface of the conductor.

In any conductor carrying alternating current, the magnetic field around the axis of the conductor produces variations in current density. In an isolated conductor current tends to flow on the outermost part and this effect becomes enlarged when frequency increases and section of conductor becomes large. In round wire or tube current is concentrated in the outer skin known as skin effect and in flat isolated strips of current is concentrated near the edges known as edge effects [50]. It is shown that at high frequencies current decays towards the center of the conductor, being confined effectively to the surface layer so that the resistance of the conductor was the same as if composed of surface strips of thickness.

A slab of conductive material to be used in describing the skin effect, the current I is concentrated in the upper surface. The total current is given by the integral of the current density in the conductive medium. This integral calculated from the surface into the medium is a decaying spiral in the complex plane, which rapidly approaches its limit if the thickness is much greater than the depth of penetration. The total current is therefore given by the integral for infinite depth, over the width w:

$$I = w \int_0^\infty idz = i_0 w \int_0^\infty \exp(-(1+j)\frac{z}{\delta_s})dz = \frac{i_0 w \delta_s}{1+j} \tag{2.3}$$

The voltage V on the surface along the length of the conductor is obtained from the current density and the volume resistivity $V = i_0 l \rho_V$. The internal impedance or surface impedance is computed from this voltage V and the current I, where $\delta_s = \sqrt{\frac{2}{\omega\mu\sigma}}$ which is traditional skin depth.

$$Z = \frac{V}{I} = (1+j)\frac{\rho l}{w\delta_s} \tag{2.4}$$

The internal inductance is the part of the total inductance which is caused by magnetic flux in conductive medium. It is computed from the internal reactance

$$L = \frac{X}{\omega} = \frac{l}{w}(\mu\frac{\delta_s}{2}) \tag{2.5}$$

This is the inductance of a layer of the conductive material having a thickness of $\delta_s/2$, one half the depth of penetration. This merely means that the mean depth of the current is one-half the thickness of the conducting layer. Some inductance formulas carry the assumption that the current travels in a thin sheet on the surface of the conductor, as if the resistivity were zero. Such assumptions are usual for transmission lines, waveguides, cavity resonators, and piston attenuators. Such formulas can be corrected for the depth of penetration by assuming that the current sheet is at a depth $\delta_s/2$ from the surface. This is the same as assuming that the surface of the conductor recedes by the amount $\frac{\delta_s}{2}\frac{\mu}{\mu_0}$. The current follows the path of least impedance and because the impedance is mainly inductive reactance, in the common cases, the current tends to follow the path of least inductance.

In a ring, for example, the current density is greater on the inner surface. If the effective thickness exceeds twice the depth of penetration, the accuracy of the above impedance formulas is sufficient for most purposes, within two per cent for a plane surface. The incremental-inductance rule is a formula which gives the effective resistance caused by the skin effect, but is based entirely on inductance computations. Its great value lies in its general validity for all metal objects in which the current and magnetic intensity are governed by the skin effect. In other words, the thickness and the radius of curvature of exposed metal surfaces must be much greater than the depth of penetration, say at least twice as great. The incremental-inductance rule states, that the effective resistance in a circuit is equal to the change of reactance caused by the penetration of magnetic flux into metal objects. Experiments on cylindrical shells reveal that the analysis of light interaction with metallic shells maybe missing an important parameter, geometry which has been analyzed in the next section.

2.3 Modal Analysis

The analysis for the ring geometry can be done by dividing the space in three regions (see figure 2.11), region 1: outside the ring ($r > b$), region 2: the ring ($a < r < b$) and region 3: inside the ring ($0 < r < a$). There are no localized charge density in entire system, thus $\rho = 0$ in Maxwell's equations. Here for the ease of calculation, we consider two dimensions in space - frequency domain (x, y, ω) for an incident field which has time harmonic ($e^{-i\omega t}$) dependence and all other fields should have same dependence.

The material equations for scalar, homogeneous, isotropic and non-dispersive material with conductivity (σ) is given by,

$$\begin{aligned}\mathbf{D}(\mathbf{r},t) &= \epsilon\mathbf{E}(\mathbf{r},t)\\ \mathbf{B}(\mathbf{r},t) &= \mu\mathbf{H}(\mathbf{r},t)\\ \mathbf{J}(\mathbf{r},t) &= \sigma\mathbf{E}(\mathbf{r},t)\end{aligned} \tag{2.6}$$

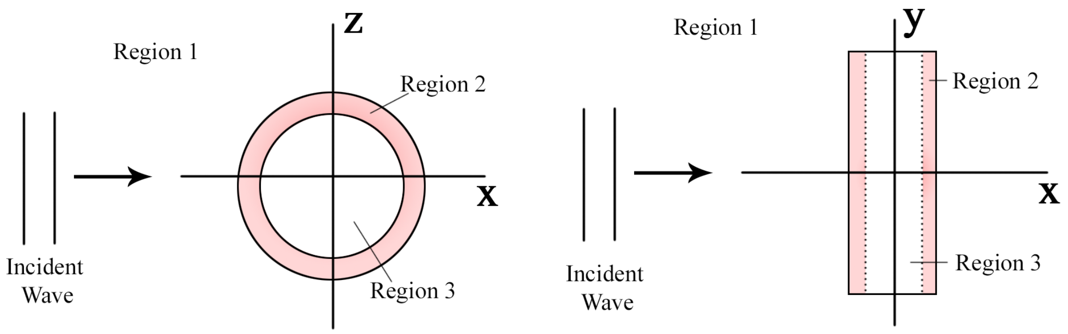

(a) Cross section of cylindrical shell. (b) Cylindrical shell.

Figure 2.11: Geometry of cylindrical shells.

The corresponding Maxwell's equation becomes,

$$\nabla \cdot \mathbf{D}(\mathbf{r}, t) = 0 \tag{2.7}$$

$$\nabla \cdot \mathbf{B}(\mathbf{r}, t) = 0 \tag{2.8}$$

$$\nabla \times \mathbf{E}(\mathbf{r}, t) = -\frac{\partial}{\partial t}\mathbf{B}(\mathbf{r}, t) \tag{2.9}$$

$$\nabla \times \mathbf{H}(\mathbf{r}, t) = \mathbf{J}(\mathbf{r}, t) + \frac{\partial}{\partial t}\mathbf{D}(\mathbf{r}, t) \tag{2.10}$$

The wave equations for electric and magnetic fields vectors can be derived from equations above using vector identities $\nabla \times \nabla \times = \nabla(\nabla \cdot) - \nabla^2$ and replacing the time derivative by $-i\omega$ in the frequency domain,

$$\nabla^2 \mathbf{E}(\mathbf{r}, t) + i\omega\mu(\sigma - i\omega\epsilon)\mathbf{E}(\mathbf{r}, t) = 0 \tag{2.11}$$

$$\nabla^2 \mathbf{H}(\mathbf{r}, t) + i\omega\mu(\sigma - i\omega\epsilon)\mathbf{H}(\mathbf{r}, t) = 0 \tag{2.12}$$

The annular ring is composed of metal with finite conductivity and surrounded by dielectrics. All three regions can be characterized by material parameters,

1. Region 1, free space: $\epsilon_1 = \epsilon_0, \mu_1 = \mu_0, \sigma_1 = 0, k_1^2 = \omega^2\epsilon_1\mu_1$

$$\nabla^2\mathbf{E}(\mathbf{r}, t) + k_1^2\mathbf{E}(\mathbf{r}, t) = 0 \tag{2.13}$$

2. Region 2, metallic annular ring $\epsilon = \epsilon_2, \mu = \mu_0, \sigma_2 = \sigma, k_2^2 = i\omega\mu(\sigma - i\omega\epsilon)$

$$\nabla^2\mathbf{E}(\mathbf{r}, t) + k_2^2\mathbf{E}(\mathbf{r}, t) = 0 \tag{2.14}$$

3. Region 3, inside the ring $\epsilon = \epsilon_3, \mu = \mu_0, \sigma_3 = 0, k_3^2 = \omega^2\epsilon_3\mu_3$

$$\nabla^2\mathbf{E}(\mathbf{r}, t) + k_3^2\mathbf{E}(\mathbf{r}, t) = 0 \tag{2.15}$$

Consider, the incident TM field polarized in $\hat{\mathbf{z}}$ traveling in $\hat{\mathbf{x}}$, $\mathbf{E}(\mathbf{r}, t) = \hat{\mathbf{z}}E_0e^{kx-i\omega t}$. The wave equations for all the regions can be solved in cylindrical coordinates using cylindrical coordinate system, assuming infinite cylinders the electric field can be written as, $E(r, \phi) = \mathbf{R}(r)\Phi(\phi)$.

For azimuthal direction

$$\frac{\partial^2\Phi}{\partial\phi^2} + n^2\Phi = 0 \tag{2.16}$$

For radial direction

$$\frac{\partial^2\mathbf{R}}{\partial r^2} + \frac{1}{r}\frac{\partial\mathbf{R}}{\partial r} + (k_i^2 - \frac{n^2}{r^2})\mathbf{R} = 0 \quad i = 1, 2, 3 \tag{2.17}$$

The solution of the equations are a set of linearly independent solutions called Hankel functions which are sum of Bessel and Neumann functions. Conventionally outgoing waves are represented by Hankel function of first kind ($H_n^{(1)}(x)$) and incoming waves are represented by Hankel function of second kind ($H_n^{(2)}(x)$) because of properties of the functions at infinity.

$$H_n^{(1)}(x) = J_n(x) + iN_n(x) \tag{2.18}$$

$$H_n^{(2)}(x) = J_n(x) - iN_n(x) \tag{2.19}$$

In region 1, the total field is composed of incident field and outgoing scattered field. Bessel functions are used to represent the incident fields under plane wave expansion and Hankel function represent the outgoing scattered field which satisfies the radiation conditions.

$$E_z(r,\phi) = E_0 \sum_{n=-\infty}^{\infty} i^n [J_n(k_1 r) + a_n H_n^{(1)}(k_1 r)] e^{in\phi} \quad r > b \tag{2.20}$$

In region 2, we have to consider both incoming and outgoing waves to capture multiple scattering which is usually ignored in literature to ease calculation. For calculation of metallic shells the argument of Hankel functions become undefined or the value becomes extremely small which requires the series expansion which has been discussed in detail in Appendix B. In the case of dielectric shells the values remain bounded and does not require expansions in general.

$$E_z(r,\phi) = E_0 \sum_{n=-\infty}^{\infty} i^n [b_n J_n(k_2 r) + c_n H_n^{(1)}(k_2 r)] e^{in\phi} \quad a < r < b \tag{2.21}$$

Region 3 contains the origin and since Neumann functions are not defined at origin, fields are defined only by Bessel functions.

$$E_z(r,\phi) = E_0 \sum_{n=-\infty}^{\infty} i^n d_n J_n(k_3 r) e^{in\phi} \quad 0 < r < a \tag{2.22}$$

Magnetic field vectors can be calculated using Maxwell's equations, in region 1,

$$H_r(r,\phi) = \frac{E_0}{i\omega\mu_0}\frac{1}{r}\sum_{n=-\infty}^{\infty} n i^{n+1}[J_n(k_1 r) + a_n H_n^{(1)}(k_1 r)]e^{in\phi} \quad r > b \tag{2.23}$$

$$H_\phi(r,\phi) = -\frac{E_0 k_1}{i\omega\mu_0}\sum_{n=-\infty}^{\infty} i^n[J'_n(k_1 r) + a_n H'^{(1)}_n(k_1 r)]e^{in\phi} \quad r > b \tag{2.24}$$

In region 2, both incoming and outgoing magnetic waves

$$H_r(r,\phi) = \frac{E_0}{i\omega\mu_0}\frac{1}{r}\sum_{n=-\infty}^{\infty} n i^{n+1}[b_n J_n(k_2 r) + c_n H_n^{(1)}(k_2 r)]e^{in\phi} \quad b \geq r \geq a \tag{2.25}$$

$$H_\phi(r,\phi) = -\frac{E_0 k_2}{i\omega\mu_0}\sum_{n=-\infty}^{\infty} i^n[b_n J'_n(k_2 r) + c_n H'^{(1)}_n(k_2 r)]e^{in\phi} \quad b \geq r \geq a \tag{2.26}$$

In region 3, Magnetic fields inside the shell

$$H_r(r,\phi) = \frac{E_0}{i\omega\mu_0}\frac{1}{r}\sum_{n=-\infty}^{\infty} n i^{n+1} d_n J_n(k_3 r)e^{in\phi} \quad a > r > 0 \tag{2.27}$$

$$H_\phi(r,\phi) = -\frac{E_0 k_3}{i\omega\mu_0}\sum_{n=-\infty}^{\infty} i^n d_n J'_n(k_3 r)e^{in\phi} \quad a > r > 0 \tag{2.28}$$

All the solutions in different regions can be stitched together using boundary conditions for metals with finite conductivity with normal vector $\hat{\mathbf{n}} = \hat{\mathbf{r}}$ and coefficients for each mode can be determined as follows,

$$\hat{\mathbf{n}} \times (\mathbf{E}_2(\mathbf{r},t) - \mathbf{E}_1(\mathbf{r},t)) = 0 \tag{2.29}$$

$$\hat{\mathbf{n}} \times (\mathbf{H}_2(\mathbf{r},t) - \mathbf{H}_1(\mathbf{r},t)) = 0 \tag{2.30}$$

For the boundary at $r = b$,

$$J_n(k_1 b) + a_n H_n^{(1)}(k_1 b) = b_n J_n^{(1)}(k_2 b) + c_n H_n^{(1)}(k_2 b) \tag{2.31}$$

For the boundary at $r = a$

$$b_n J_n(k_2 a) + c_n H_n^{(1)}(k_2 a) = d_n J_n(k_3 a) \tag{2.32}$$

Continuity of tangential magnetic field vector $r = b$

$$k_1[J_n'(k_1 b) + a_n H_n'^{(1)}(k_1 b)] = k_2[b_n J_n'(k_2 b) + c_n H_n'^{(1)}(k_2 b)] \tag{2.33}$$

Continuity of tangential magnetic field vector $r = a$

$$k_2[b_n J_n'(k_2 a) + c_n H_n'^{(1)}(k_2 a)] = k_3 d_n J_n'(k_3 a) \tag{2.34}$$

The coefficients can be found by solving the system of equations in four variables using Cramer's rule and determinants.

$$\begin{bmatrix} H_n^{(1)}(k_1 b) & -J_n^{(1)}(k_2 b) & -H_n^{(1)}(k_2 b) & 0 \\ 0 & J_n(k_2 a) & H_n^{(1)}(k_2 a) & -J_n(k_3 a) \\ k_1 H_n'^{(1)}(k_1 b) & -k_2 J_n'(k_2 b) & -k_2 H_n'^{(1)}(k_2 b) & 0 \\ 0 & k_2 J_n'(k_2 a) & k_2 H_n'^{(1)}(k_2 a) & -k_3 J_n'(k_3 a) \end{bmatrix} \begin{bmatrix} a_n \\ b_n \\ c_n \\ d_n \end{bmatrix} = \begin{bmatrix} -J_n(k_1 b) \\ 0 \\ -k_1 J_n'(k_1 b) \\ 0 \end{bmatrix} \tag{2.35}$$

Using the principles of linear algebra the system of equations $\mathbf{A}\tilde{x} = \mathbf{b}$ can be solved for coefficients represented in vector $\tilde{x}$.

$$a_n = \frac{\begin{vmatrix} -J_n(k_1b) & -J_n(k_2b) & -H_n^{(1)}(k_2b) & 0 \\ 0 & J_n(k_2a) & H_n^{(1)}(k_2a) & -J_n(k_3a) \\ -k_1J_n'(k_1b) & -k_2J_n'(k_2b) & -k_2H_n'^{(1)}(k_2b) & 0 \\ 0 & k_2J_n'(k_2a) & k_2H_n'^{(1)}(k_2a) & -k_3J_n'(k_3a) \end{vmatrix}}{\begin{vmatrix} H_n^{(1)}(k_1b) & -J_n(k_2b) & -H_n^{(1)}(k_2b) & 0 \\ 0 & J_n(k_2a) & H_n^{(1)}(k_2a) & -J_n(k_3a) \\ k_1H_n'^{(1)}(k_1b) & -k_2J_n'(k_2b) & -k_2H_n'^{(1)}(k_2b) & 0 \\ 0 & k_2J_n'(k_2a) & k_2H_n'^{(1)}(k_2a) & -k_3J_n'(k_3a) \end{vmatrix}} \tag{2.36}$$

$$b_n = \frac{\begin{vmatrix} H_n^{(1)}(k_1b) & -J_n(k_1b) & -H_n^{(1)}(k_2b) & 0 \\ 0 & 0 & H_n^{(1)}(k_2a) & -J_n(k_3a) \\ k_1H_n'^{(1)}(k_1b) & -k_1J_n'(k_1b) & -k_2H_n'^{(1)}(k_2b) & 0 \\ 0 & 0 & k_2H_n'^{(1)}(k_2a) & -k_3J_n'(k_3a) \end{vmatrix}}{\begin{vmatrix} H_n^{(1)}(k_1b) & -J_n(k_2b) & -H_n^{(1)}(k_2b) & 0 \\ 0 & J_n(k_2a) & H_n^{(1)}(k_2a) & -J_n(k_3a) \\ k_1H_n'^{(1)}(k_1b) & -k_2J_n'(k_2b) & -k_2H_n'^{(1)}(k_2b) & 0 \\ 0 & k_2J_n'(k_2a) & k_2H_n'^{(1)}(k_2a) & -k_3J_n'(k_3a) \end{vmatrix}} \tag{2.37}$$

$$c_n = \frac{\begin{vmatrix} H_n^{(1)}(k_1b) & -J_n(k_2b) & -J_n(k_1b) & 0 \\ 0 & J_n(k_2a) & 0 & -J_n(k_3a) \\ k_1H_n'^{(1)}(k_1b) & -k_2J_n'(k_2b) & -k_1J_n'(k_1b) & 0 \\ 0 & k_2J_n'(k_2a) & 0 & -k_3J_n'(k_3a) \end{vmatrix}}{\begin{vmatrix} H_n^{(1)}(k_1b) & -J_n(k_2b) & -H_n^{(1)}(k_2b) & 0 \\ 0 & J_n(k_2a) & H_n^{(1)}(k_2a) & -J_n(k_3a) \\ k_1H_n'^{(1)}(k_1b) & -k_2J_n'(k_2b) & -k_2H_n'^{(1)}(k_2b) & 0 \\ 0 & k_2J_n'(k_2a) & k_2H_n'^{(1)}(k_2a) & -k_3J_n'(k_3a) \end{vmatrix}} \tag{2.38}$$

$$d_n = \frac{\begin{vmatrix} H_n^{(1)}(k_1 b) & -J_n(k_2 b) & -H_n^{(1)}(k_2 b) & -J_n(k_1 b) \\ 0 & J_n(k_2 a) & H_n^{(1)}(k_2 a) & 0 \\ k_1 H_n'^{(1)}(k_1 b) & -k_2 J_n'(k_2 b) & -k_2 H_n'^{(1)}(k_2 b) & -k_1 J_n'(k_1 b) \\ 0 & k_2 J_n'(k_2 a) & k_2 H_n'^{(1)}(k_2 a) & 0 \end{vmatrix}}{\begin{vmatrix} H_n^{(1)}(k_1 b) & -J_n(k_2 b) & -H_n^{(1)}(k_2 b) & 0 \\ 0 & J_n(k_2 a) & H_n^{(1)}(k_2 a) & -J_n(k_3 a) \\ k_1 H_n'^{(1)}(k_1 b) & -k_2 J_n'(k_2 b) & -k_2 H_n'^{(1)}(k_2 b) & 0 \\ 0 & k_2 J_n'(k_2 a) & k_2 H_n'^{(1)}(k_2 a) & -k_3 J_n'(k_3 a) \end{vmatrix}} \tag{2.39}$$

This is the complete and exact solution of TM electromagnetic field being scattered from a two dimensional annular ring or an infinitely long cylinder of finite conductivity. Similar calculation can be performed for TE case by assuming the magnetic field is propagating in x direction and polarized in $\hat{\mathbf{z}}$, then $\mathbf{H}(\mathbf{r}, t) = \hat{\mathbf{z}} H_0 e^{\mathbf{k}x - i\omega t}$. From Maxwell's equations 1.3 we obtain the electric fields,

$$E_r = \frac{1}{\sigma - i\omega\epsilon} \frac{1}{r} \frac{\partial H_z}{\partial \phi} \tag{2.40}$$

$$E_\phi = \frac{-1}{\sigma - i\omega\epsilon} \frac{\partial H_z}{\partial r} \tag{2.41}$$

Thus, full electromagnetic solution in region 1:

$$H_z(r, \phi) = H_0 \sum_{n=-\infty}^{\infty} i^n [J_n(k_1 r) + e_n H_n^{(1)}(k_1 r)] e^{in\phi} \quad r > b \tag{2.42}$$

$$E_r(r, \phi) = \frac{H_0}{i\omega\epsilon_1} \frac{1}{r} \sum_{n=-\infty}^{\infty} n i^{n+1} [J_n(k_1 r) + e_n H_n^{(1)}(k_1 r)] e^{in\phi} \quad r > b \tag{2.43}$$

$$E_\phi(r, \phi) = -\frac{H_0 k_1}{i\omega\epsilon_1} \sum_{n=-\infty}^{\infty} i^n [J_n'(k_1 r) + e_n H_n'^{(1)}(k_1 r)] e^{in\phi} \quad r > b \tag{2.44}$$

In Region 2:

$$H_z(r,\phi) = H_0 \sum_{n=-\infty}^{\infty} i^n [f_n J_n(k_2 r) + g_n H_n^{(1)}(k_2 r)] e^{in\phi} \quad b \geq r \geq a \tag{2.45}$$

$$E_r(r,\phi) = \frac{H_0}{\sigma - i\omega\epsilon_2} \frac{1}{r} \sum_{n=-\infty}^{\infty} n i^{n+1} [f_n J_n(k_2 r) + g_n H_n^{(1)}(k_2 r)] e^{in\phi} \quad b \geq r \geq a \tag{2.46}$$

$$E_\phi(r,\phi) = -\frac{H_0 k_2}{\sigma - i\omega\epsilon_2} \sum_{n=-\infty}^{\infty} i^n [f_n J_n'(k_2 r) + g_n H_n'^{(1)}(k_2 r)] e^{in\phi} \quad b \geq r \geq a \tag{2.47}$$

In Region 3:

$$H_z(r,\phi) = H_0 \sum_{n=-\infty}^{\infty} i^n h_n J_n(k_3 r) e^{in\phi} \quad a > r > 0 \tag{2.48}$$

$$E_r(r,\phi) = \frac{H_0}{i\omega\epsilon_3} \frac{1}{r} \sum_{n=-\infty}^{\infty} n i^{n+1} h_n J_n(k_3 r) e^{in\phi} \quad a > r > 0 \tag{2.49}$$

$$E_\phi(r,\phi) = -\frac{H_0 k_3}{i\omega\epsilon_3} \sum_{n=-\infty}^{\infty} i^n h_n J_n'(k_3 r) e^{in\phi} \quad a > r > 0 \tag{2.50}$$

In the same manner as TM case, using the boundary conditions and continuity of tangential magnetic field vector at $r = b$ implies,

$$J_n(k_1 b) + e_n H_n^{(1)}(k_1 b) = f_n J_n^{(1)}(k_2 b) + g_n H_n^{(1)}(k_2 b) \tag{2.51}$$

For the boundary at $r = a$

$$f_n J_n(k_2 a) + g_n H_n^{(1)}(k_2 a) = h_n J_n(k_3 a) \tag{2.52}$$

Continuity of tangential electric field vector $r = b$

$$\frac{k_1}{i\omega\epsilon_1}[J_n'(k_1 b) + e_n H_n'^{(1)}(k_1 b)] = \frac{-k_2}{\sigma - i\omega\epsilon_2}[f_n J_n'(k_2 b) + g_n H_n'^{(1)}(k_2 b)] \tag{2.53}$$

Continuity of tangential electric field vector $r = a$

$$\frac{-k_2}{\sigma - i\omega\epsilon_2}[f_n J_n'(k_2 a) + g_n H_n'^{(1)}(k_2 a)] = \frac{k_3}{i\omega\epsilon_3} h_n J_n'(k_3 a) \tag{2.54}$$

Similarly, the coefficients can be determined

$$\begin{bmatrix} H_n^{(1)}(k_1 b) & -J_n(k_2 b) & -H_n^{(1)}(k_2 b) & 0 \\ 0 & J_n(k_2 a) & H_n^{(1)}(k_2 a) & -J_n(k_3 a) \\ \frac{k_1}{i\omega\epsilon_1} H_n'^{(1)}(k_1 b) & \frac{k_2}{\sigma - i\omega\epsilon_2} J_n'(k_2 b) & \frac{k_2}{\sigma - i\omega\epsilon_2} H_n'^{(1)}(k_2 b) & 0 \\ 0 & \frac{-k_2}{\sigma - i\omega\epsilon_2} J_n'(k_2 a) & \frac{-k_2}{\sigma - i\omega\epsilon_2} H_n'^{(1)}(k_2 a) & \frac{-k_3}{i\omega\epsilon_3} J_n'(k_3 a) \end{bmatrix} \begin{bmatrix} e_n \\ f_n \\ g_n \\ h_n \end{bmatrix} = \begin{bmatrix} -J_n(k_1 b) \\ 0 \\ \frac{-k_1}{i\omega\epsilon_3} J_n'(k_1 b) \\ 0 \end{bmatrix} \tag{2.55}$$

Using principles of linear algebra the exact and complete solution of electromagnetic scattering of TE waves from cylinders can be obtained. In order to visualize the propagation of fields described by the equations above have to be programmed. The arguments of Bessel and Hankel functions in are complex for the metallic region, hence we have to use series and asymptotic expansion of these functions as they become small for an large argument. Using series expansions that are available in standard textbooks [51, 52, 53] we can simplify the problem. A detailed analysis of series expansion of Bessel and Hankel functions has been presented in Appendix B. In the case of waves in a metallic object the wavenumber becomes complex and can be represented as $x_c = p + iq$, then equation B.21 and B.22 becomes

$$J_m(x) \approx \sqrt{\frac{1}{2\pi x}}[e^{i(p-\frac{m\pi}{2}-\frac{\pi}{4})}e^{-q} + e^{-i(p-\frac{m\pi}{2}-\frac{\pi}{4})}e^{+q}] \tag{2.56}$$

$$H_m^{(1)}(x) = \sqrt{\frac{2}{\pi x}}e^{i(x-\frac{m\pi}{2}-\frac{\pi}{4})}e^{-q} \tag{2.57}$$

Using the values of conductivity, a rough estimate of the imaginary part of wavenumber $k_2 = \sqrt{\omega\mu_0\sigma} \approx 10^6$, hence the first term of Bessel function expansion can be neglected for ease of calculations and the asymptotic expansion is valid as k_2b & $k_2a \geq 10^3$.

$$J_m(x) = \sqrt{\frac{1}{2\pi x}}e^{-i(p-\frac{m\pi}{2}-\frac{\pi}{4})}e^{+q} \tag{2.58}$$

Another important consequence of the real values the phase of the complex quantity k_2

$$Arg[k_2] = \frac{1}{2}\arctan[\frac{\sigma}{\epsilon_0\omega}] \approx \frac{\pi}{4} \tag{2.59}$$

Our main concern is the field in the region inside the ring hence, calculation of d_n is important. We start with the calculation of zeroth order denominator for the coefficient d_{0d} given by the determinant,

$$\begin{aligned} d_n = H_n^{(1)}(k_1b) &\begin{vmatrix} J_n(k_2a) & H_n^{(1)}(k_2a) & -J_n(k_3a) \\ -k_2J_n'(k_2b) & -k_2H_n'^{(1)}(k_2b) & 0 \\ k_2J_n'(k_2a) & k_2H_n'^{(1)}(k_2a) & -k_3J_n'(k_3a) \end{vmatrix} \\ +k_1H_n'^{(1)}(k_1b) &\begin{vmatrix} -J_n(k_2b) & -H_n^{(1)}(k_2b) & 0 \\ J_n(k_2a) & H_n^{(1)}(k_2a) & -J_n(k_3a) \\ k_2J_n'(k_2a) & k_2H_n'^{(1)}(k_2a) & -k_3J_n'(k_3a) \end{vmatrix} \end{aligned} \tag{2.60}$$

It implies,

$$\begin{aligned} d_{0d} = k_2 H_0^{(1)}(k_1 b)[k_2 J_0(k_3 a)[J_0'(k_2 b) H_0'^{(1)}(k_2 a) - J_0'(k_2 a) H_0'^{(1)}(k_2 b)]_{\mathbf{1}} + \\ k_3 J_0'(k_3 a)[J_0(k_2 a) H_0'^{(1)}(k_2 b) - J_0'(k_2 b) H_0^{(1)}(k_2 a)]_{\mathbf{2}}] + \\ -k_1 H_0'^{(1)}(k_1 b)[k_2 J_0(k_3 a)[J_0(k_2 b) H_0'^{(1)}(k_2 a) - J_0'(k_2 a) H_0^{(1)}(k_2 b)]_{\mathbf{3}} + \\ k_3 J_0'(k_3 a)[J_0(k_2 b) H_0^{(1)}(k_2 b) - J_0(k_2 a) H_n^{(1)}(k_2 b)]_{\mathbf{4}}] \end{aligned} \tag{2.61}$$

We will take a look at each bracket $[\ ]_i$ in detail and use asymptotic forms to simplify the results because of the value of the arguments of the functions.

$$\begin{aligned} [\ ]_{\mathbf{1}} &= J_0'(k_2 b) H_0'^{(1)}(k_2 a) - J_0'(k_2 a) H_0'^{(1)}(k_2 b) \\ &= J_1'(k_2 b) H_1'^{(1)}(k_2 a) - J_1'(k_2 a) H_1^{(1)}(k_2 b) \end{aligned} \tag{2.62}$$

Representing the arguments as $k_2 a = p_1 + i q_1$ and $k_2 b = p_2 + i q_2$ and equation 2.59, we get

$$[\ ]_{\mathbf{1}} = \frac{e^{i\frac{\pi}{4}}}{\pi} \sqrt{\frac{1}{(k_2 a)(k_2 b)}} [e^{-i(p_2 - p_1)} e^{(q_2 - q_1)} - e^{i(p_2 - p_1)} e^{-(q_2 - q_1)}] \tag{2.63}$$

Manipulating the complex $k_2 = |k_2| e^{-iArg[k_2]} = |k_2|(\cos(Arg[k_2]) - i \sin(Arg[k_2]))$, we get

$$p_2 - p_1 = q_2 - q_1 = \delta = \frac{1}{\sqrt{2}} |k_2| (b - a) \tag{2.64}$$

Hence, the first bracket becomes,

$$\begin{aligned} [\ ]_{\mathbf{1}} &= \frac{e^{i\frac{\pi}{4}}}{\pi} \sqrt{\frac{1}{(k_2 a)(k_2 b)}} [e^{i\delta} e^{\delta} - e^{i\delta} e^{-\delta}] \\ &= \frac{1}{\pi} \sqrt{\frac{2}{(k_2 a)(k_2 b)}} [(\cos(\delta) \sinh(\delta) - \sin(\delta) \cosh(\delta)) \\ &\quad -i(\cos(\delta) \sinh(\delta) + \sin(\delta) \cosh(\delta))] \end{aligned} \tag{2.65}$$

The second bracket becomes

$$\begin{aligned}[\ ]_{\mathbf{2}} &= J_0(k_2a)H_0'^{(1)}(k_2b) - J_0'(k_2b)H_0^{(1)}(k_2a)\\ &= J_1(k_2b)H_0^{(1)}(k_2a) - J_0(k_2a)H_1^{(1)}(k_2b)\\ &= \frac{ie^{i\frac{\pi}{4}}}{\pi}\sqrt{\frac{1}{(k_2a)(k_2b)}}[e^{-i\delta}e^{\delta} - e^{i\delta}e^{-\delta}]\\ = \frac{1}{\pi}\sqrt{\frac{2}{(k_2a)(k_2b)}}&[[\cos(\delta)\cosh(\delta) + \sin(\delta)\sinh(\delta)]+\\ &i[\cos(\delta)\cosh(\delta) - \sin(\delta)\sinh(\delta)]]\end{aligned} \tag{2.66}$$

Similarly, third bracket,

$$\begin{aligned}[\ ]_{\mathbf{3}} &= J_0^{(1)}(k_2b)H_0'^{(1)}(k_2a) - J_0'(k_2a)H_0^{(1)}(k_2b)\\ &= J_1(k_2a)H_0^{(1)}(k_2b) - J_0^{(1)}(k_2b)H_1^{(1)}(k_2a)\\ &= \frac{ie^{i\frac{\pi}{4}}}{\pi}\sqrt{\frac{1}{(k_2a)(k_2b)}}[e^{i\delta}e^{-\delta} - e^{-i\delta}e^{\delta}]\\ = \frac{1}{\pi}\sqrt{\frac{2}{(k_2a)(k_2b)}}&[[\cos(\delta)\cosh(\delta) + \sin(\delta)\sinh(\delta)]+\\ &i[\cos(\delta)\cosh(\delta) - \sin(\delta)\sinh(\delta)]]\end{aligned} \tag{2.67}$$

For bracket 4,

$$\begin{aligned}[\ ]_{\mathbf{4}} &= J_0^{(1)}(k_2b)H_0^{(1)}(k_2b) - J_0(k_2a)H_0^{(1)}(k_2b)\\ &= \frac{e^{i\frac{\pi}{4}}}{\pi}\sqrt{\frac{1}{(k_2a)(k_2b)}}[e^{i\delta}e^{-\delta} - e^{-i\delta}e^{\delta}]\\ = \frac{1}{\pi}\sqrt{\frac{2}{(k_2a)(k_2b)}}&[(\sin(\delta)\cosh(\delta) - \cos(\delta)\sinh(\delta))\\ &-i(\cos(\delta)\sinh(\delta) + \sin(\delta)\cosh(\delta))]\end{aligned} \tag{2.68}$$

Thus, to recap the calculation of the denominator it is helpful to realize that

$$\begin{aligned}[\;]_{\mathbf{1}} &= -[\;]_{\mathbf{4}} = \Lambda \\ [\;]_{\mathbf{2}} &= [\;]_{\mathbf{3}} = \Pi\end{aligned} \tag{2.69}$$

Thus, the denominator can be defined as,

$$\begin{aligned}d_{0d} = {} & k_2 H_0^{(1)}(k_1 b)[k_2 J_0(k_3 a)\Lambda + k_3 J_0'(k_3 a)\Pi] \\ & -k_1 H_0'^{(1)}(k_1 b)[k_2 J_0(k_3 a)\Pi - k_3 J_0'(k_3 a)\Lambda]\end{aligned} \tag{2.70}$$

Rearranging the terms and using the first derivative of Bessel functions, we get

$$\begin{aligned}d_{0d} = {} & \Lambda[k_2^2 H_0^{(1)}(k_1 b) J_0(k_3 a) + k_1 k_3 H_1'^{(1)}(k_1 b) J_1'(k_3 a)] \\ & -k_2 \Pi[k_3 H_0^{(1)}(k_1 b) J_1(k_3 a) - k_1 H_1^{(1)}(k_1 b) J_0(k_3 a)] \\ & = \Lambda A + \Pi B\end{aligned} \tag{2.71}$$

Now, let's calculate the numerator using the same procedure

$$d_{0n} = k_1 k_2 [H_0^{(1)}(k_1 b) J_0'(k_1 b) - J_0(k_1 b) H_0'^{(1)}(k_1 b)][J_0(k_2 a) H_0'^{(1)}(k_2 a) - H_0^{(1)}(k_2 a) J_0'(k_2 a)] \tag{2.72}$$

$$d_{0n} = k_1 k_2 [H_0^{(1)}(k_1 b) J_1(k_1 b) - J_0(k_1 b) H_1^{(1)}(k_1 b)][J_0(k_2 a) H_1^{(1)}(k_2 a) - H_0^{(1)}(k_2 a) J_1(k_2 a)] \tag{2.73}$$

Using the definition of Hankel functions, we get

$$d_{0n} = k_1 k_2 [J_1(k_1 b) N_0(k_1 b) - J_0(k_1 b) N_1(k_1 b)][J_0(k_2 a) N_1(k_2 a) - N_0(k_2 a) J_1(k_2 a)] \quad (2.74)$$

The recursion relation between Bessel and Neumann functions leads to the following identity

$$J_n(x) N_{n+1}(x) - J_{n+1}(x) N_n(x) = -\frac{2}{\pi x} \quad (2.75)$$

Thus, the numerator becomes

$$d_{0n} = \frac{4}{\pi^2 ab} \quad (2.76)$$

Thus, the exact result using series expansions of Bessel and Hankel function for the coefficient of fields inside the ring is given by

$$d_0 = \frac{4}{\pi^2 ab} \frac{1}{\Lambda A + \Pi B} \quad (2.77)$$

After calculating the coefficient of fields inside the metallic shell, we can calculate the fields

$$E_z(r, \phi) = E_0 \sum_{n=-\infty}^{\infty} i^n d_n J_n(k_3 r) e^{in\phi} \quad 0 < r < a \quad (2.78)$$

In the simplest case, at the axis of the shell with $J_0(0) = 1$ and penetration coefficient for TM incidence in dB can be defined as

$$\Delta_{TM} = 20 log |\frac{E_z(r=0)}{E_0}| \quad (2.79)$$

Similarly, the penetration coefficient for TE incidence is defined as,

$$\Delta_{TE} = 20log|\frac{H_z(r=0)}{H_0}| \tag{2.80}$$

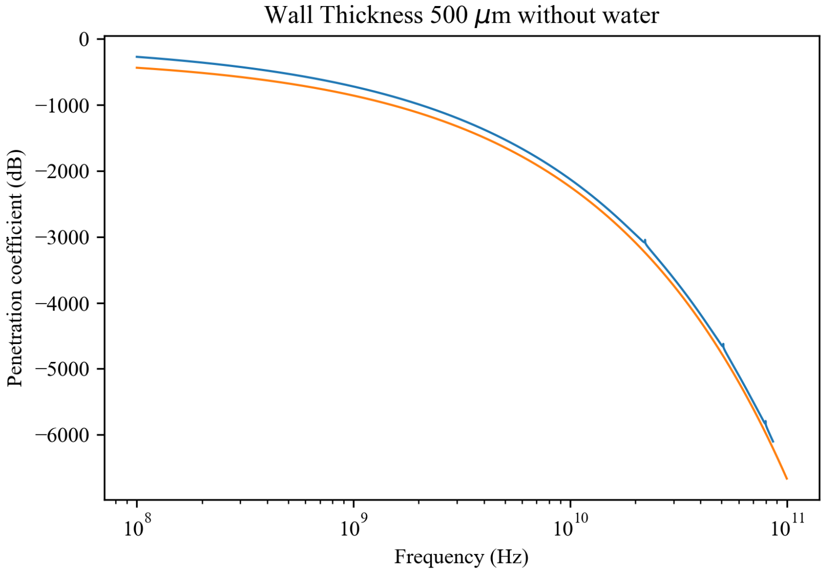

(a) Δ_{TM} for empty shell.

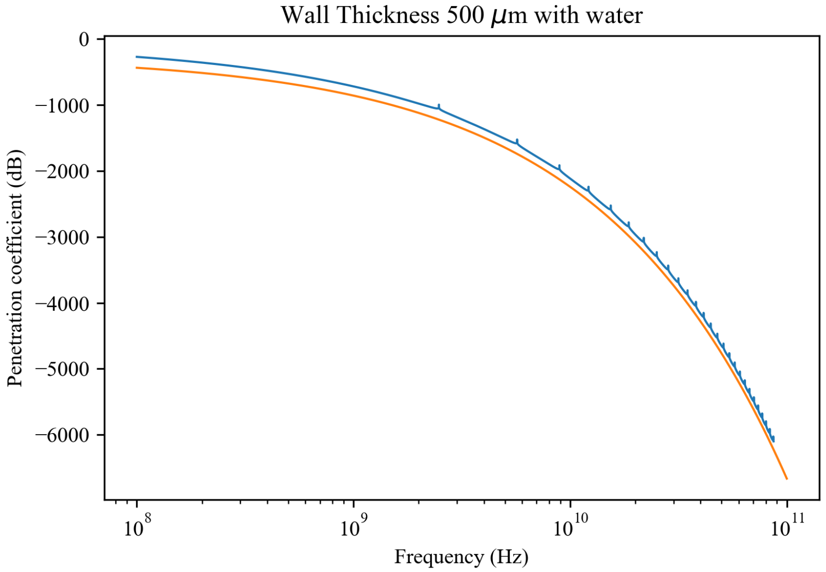

(b) Δ_{TM} for shell with water $\epsilon_r = 80$.

Figure 2.12: Cylindrical shells with wall thickness $= 500\ \mu m$. Blue curve represents the exact solution and orange curve shows approximate solutions.

In the figure 2.12, 2.13 and 2.14 we have demonstrated the importance of using

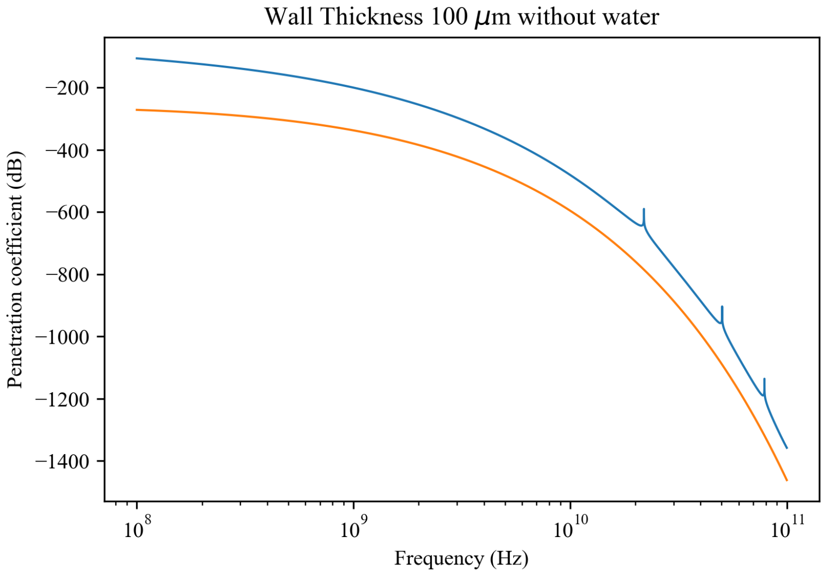

(a) Δ_{TM} for empty shell.

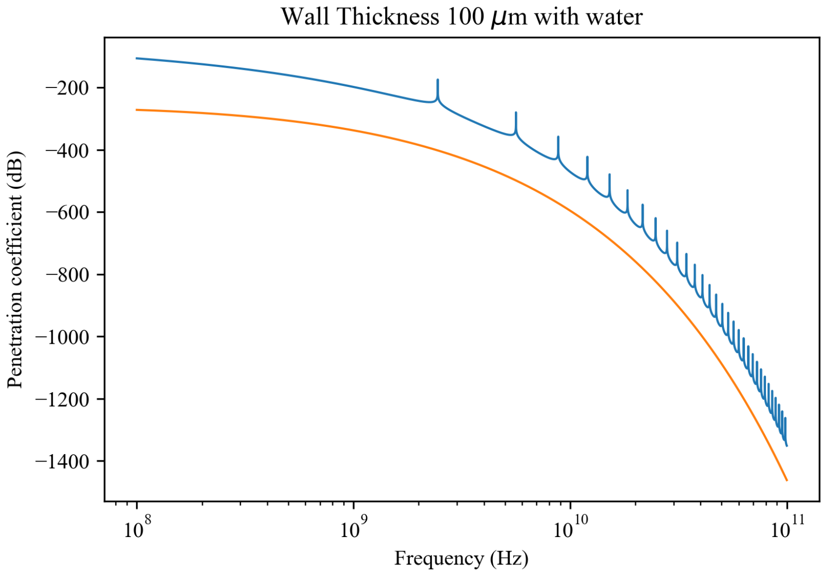

(b) Δ_{TM} for shell with water $\epsilon_r = 80$.

Figure 2.13: Cylindrical shells with wall thickness $= 100\ \mu m$. Blue curve represents the exact solution and orange curve shows approximate solutions..

exact solutions for scattering from cylindrical shells. It is evident that the features of where the field penetrates deeper that the skin depth calculated from the assumption of infinite medium or infinite conductivity solution are missed.

As expected the magnitude of fields inside the shell decrease as the wall thick-

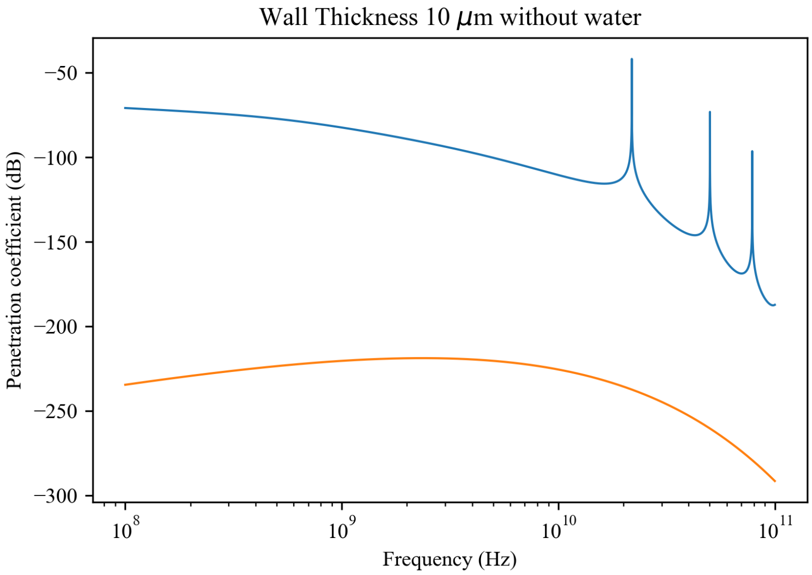

(a) Δ_{TM} for empty shell.

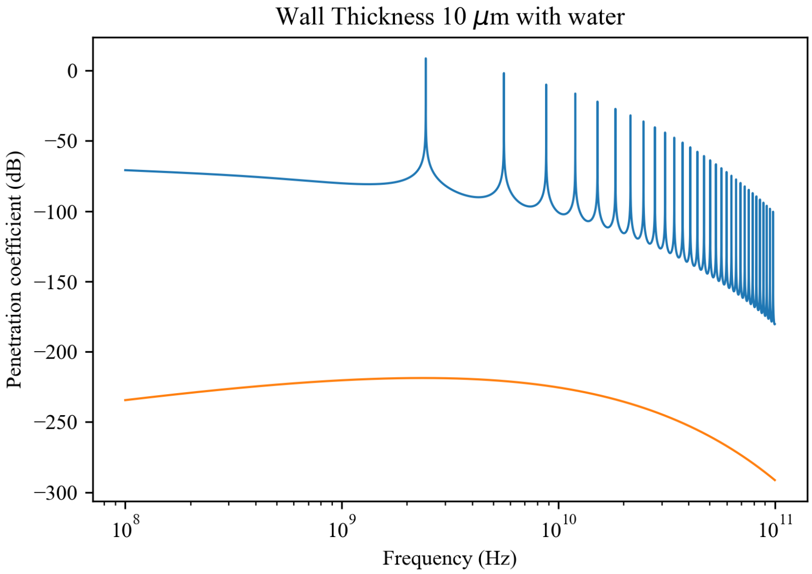

(b) Δ_{TM} for shell with water $\epsilon_r = 80$.

Figure 2.14: Cylindrical shells with wall thickness $= 10\ \mu m$. Blue curve represents the exact solution and orange curve shows approximate solutions.

ness increases but the penetration is still greater than the fields calculated by the approximate formula. This method also enables us to study the effects of varying the material inside the shells. The presence of water in the changes the profile of penetration allowing higher number of frequency with increased transmission.

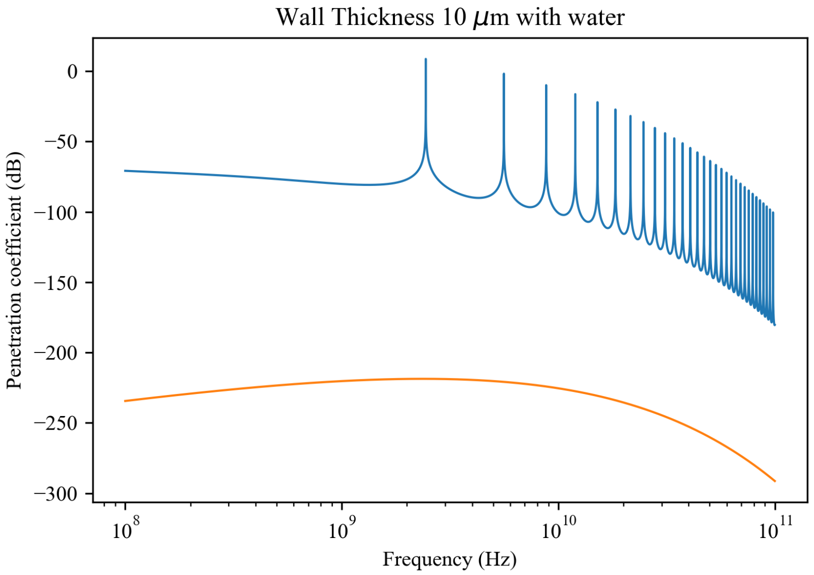

(a) Δ_{TM} for shell with water $\epsilon_r = 80$.

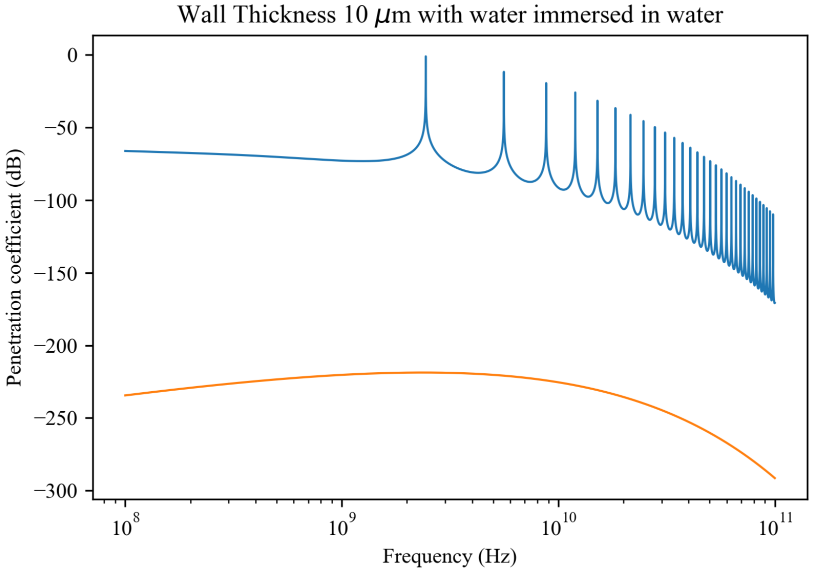

(b) Δ_{TM} for shell with water $\epsilon_r = 80$ immersed in water.

Figure 2.15: Tolerance to change in surrounding medium.

It is well known that that transmission of electromagnetic fields is greatly enhanced in Fabry-Perot cavities when a resonance condition is satisfied. Similar effects can be expected in case of cylinders and once the resonance is achieved the transmission is increased which enables the wave to interact with contents of the shell. The calculation

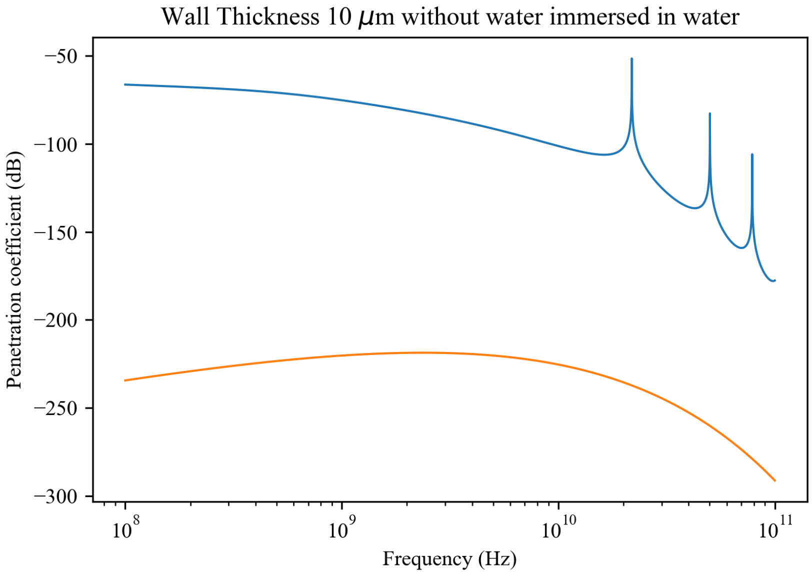

(a) Δ_{TM} for empty shell immersed in water.

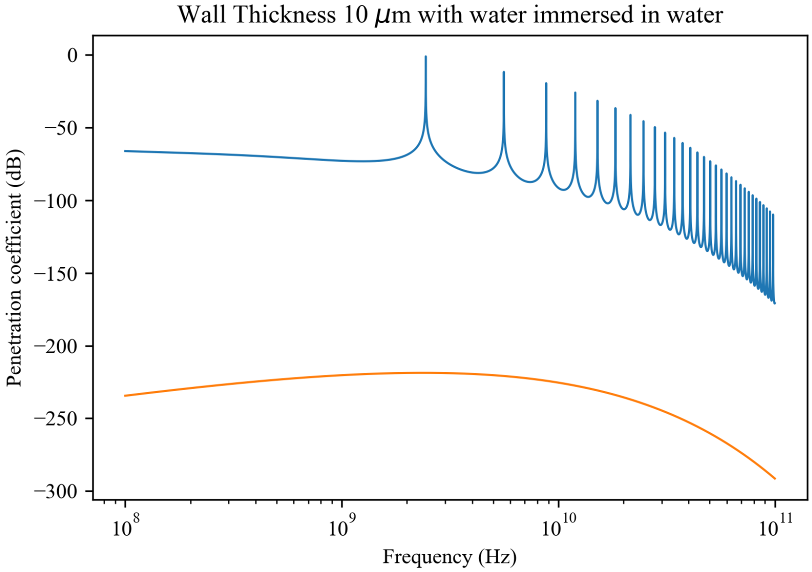

(b) Δ_{TM} for shell with water $\epsilon_r = 80$ immersed in water.

Figure 2.16: The change in number of resonant frequencies due to change in material inside but same surrounding medium. It is also important to note the values of penetration coefficients change by one and half order of magnitudes for empty and full shell.

of resonance condition for infinitely long cylindrical shells or two dimensional rings we consider linearly polarized plane-wave incident on the cylinder with its direction of

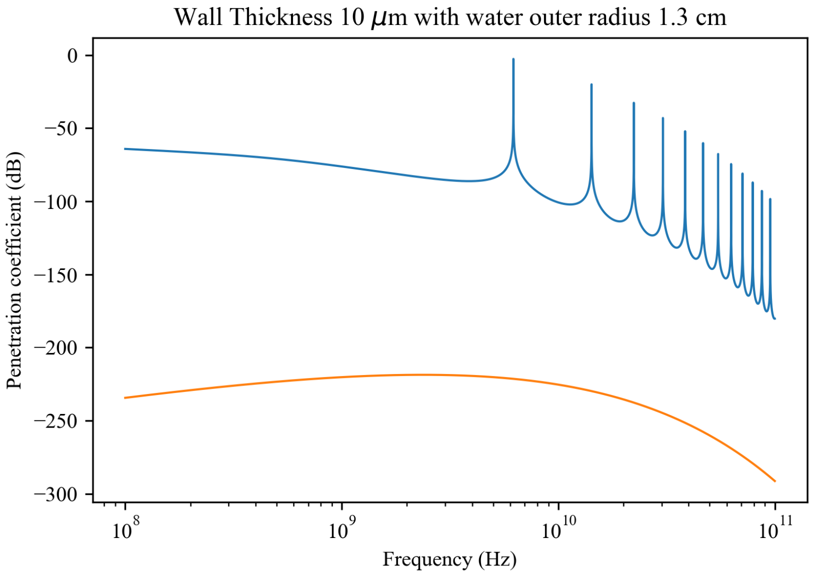

(a) Δ_{TM} for shell with water $\epsilon_r = 80$ and outer radius $1.3cm$.

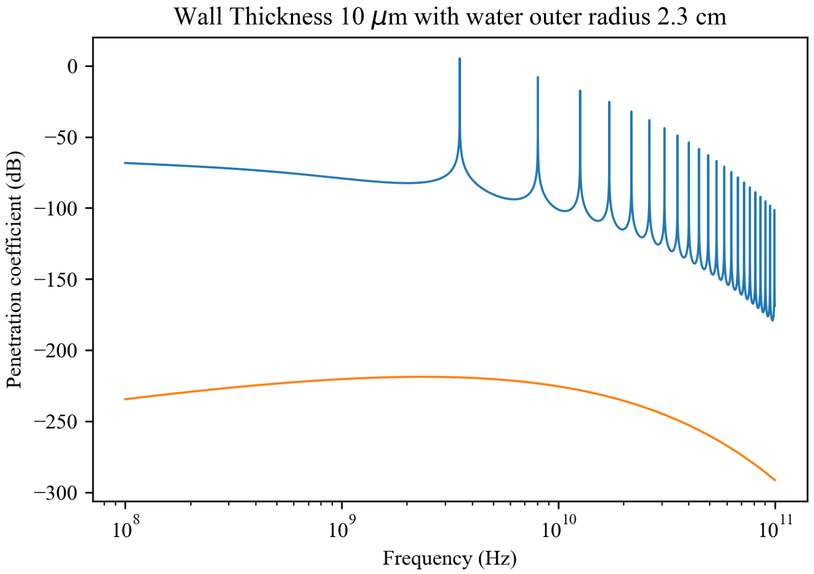

(b) Δ_{TM} for shell with water $\epsilon_r = 80$ and outer radius $2.3cm$.

Figure 2.17: The change in position of resonant frequencies due to change radius of the shells.

propagation perpendicular to the cylinder axis. In these calculations, two polarization states shall be analyzed separately: one state of linear polarization of the incident wave with the **E**-vector parallel to the cylinder axis (TM), and one polarization state with the **H**-vector parallel to the cylinder axis (TE). The resonance for TE occurs

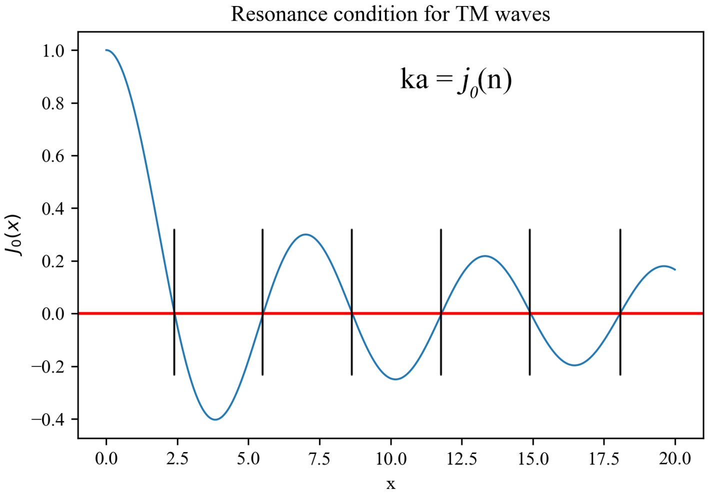

(a) Resonance condition for TM mode for empty shell.

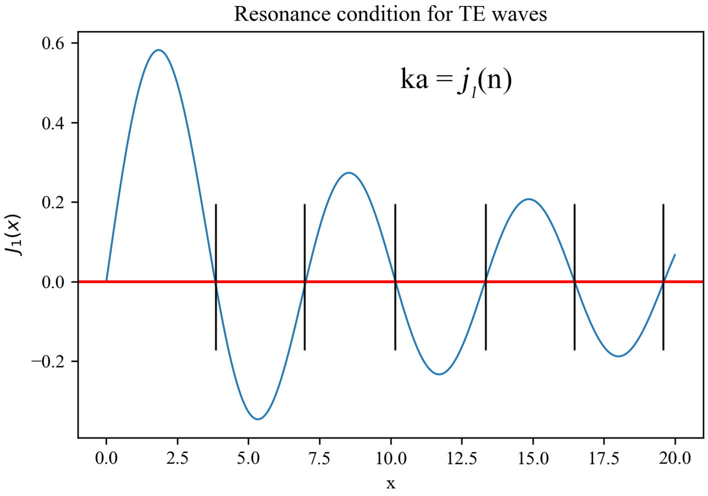

(b) Resonance condition for TE mode for empty shell.

Figure 2.18: The penetration is enhanced when the resonance condition is satisfied at these discrete the zeros of the Bessel functions.

when $ka = j_1(n)$ where $j_1(n)$ are the nth zeros of $J_1(x)$ and for TM $ka = j_0(n)$ where $j_0(n)$ are the nth zeros of $J_0(x)$. These conditions are valid for an empty shell and has been plotted in figures 2.18a and 2.18b which shows the such response can only be obtained for certain discrete values and form a basis for design of accurate meta-atoms. In the next section, we summarize the mathematical framework and discuss its implications on design and characterization of light meta-structure interactions.

2.4 Conclusions

Mathematical Framework 1: Scattering from annular ring.

```
Input: Incident Electric field: $\mathbf{E}(\mathbf{r},t) = \hat{\mathbf{z}} E_0 e^{kx-i\omega t}$
case Region 1 do
    For $r \geq b$ use Bessel functions and Hankel functions of first kind.
    $E_z(r,\phi) = E_0 \sum_{n=-\infty}^{\infty} i^n [J_n(k_1 r) + a_n H_n^{(1)}(k_1 r)] e^{in\phi} \quad r > b$    (2.81)
case Region 2 do
    For $b \geq r \geq a$ use Bessel functions and Hankel functions of first kind.
    $E_z(r,\phi) = E_0 \sum_{n=-\infty}^{\infty} i^n [b_n J_n(k_2 r) + c_n H_n^{(1)}(k_2 r)] e^{in\phi} \quad b \geq r \geq a$    (2.82)
case Region 3 do
    For $a \geq r \geq 0$ use Bessel functions only.
    $E_z(r,\phi) = E_0 \sum_{n=-\infty}^{\infty} i^n d_n J_n(k_3 r) e^{in\phi} \quad a > r > 0$    (2.83)
for Boundary Condition do
    Use $\hat{\mathbf{r}} \times (\mathbf{E}_2 - \mathbf{E}_1) = \hat{\mathbf{r}} \times (\mathbf{H}_2 - \mathbf{H}_1) = 0$, $\mathbf{H}$ is obtained by Faraday's Law
    Use $\mathbf{A}\tilde{x} = \mathbf{b}$ and $\tilde{x}_i = \frac{det(\mathbf{A}_i)}{det(\mathbf{A})}$
    Series and asymptotic expansions of Bessel and Hankel functions
    Plot the field at the center of the annular ring
    $\Delta_{TM} = 20log|\frac{E_z(r=0)}{E_0}|$    (2.84)
Result: Penetration coefficient for transverse magnetic case ($\Delta_{TM}$)
```

We have shown that rigorous analysis of light interaction with metallic cylindrical shells we have shown that the geometry is very important to the analysis of scattering. This explains the higher penetration of fields in the shells and the influence of liquid inside the shell. The number of frequencies where the coefficient of penetration increase by two order of magnitudes increase when the permittivity value of material inside increases but is unaffected when by the change outside. The analysis using fields is cumbersome due to the presence of two boundaries. We summarize the method developed to analyze TM electromagnetic wave interactions with cylindrical shells in mathematical framework 1. This method can easily be modified for analysis of TM waves.

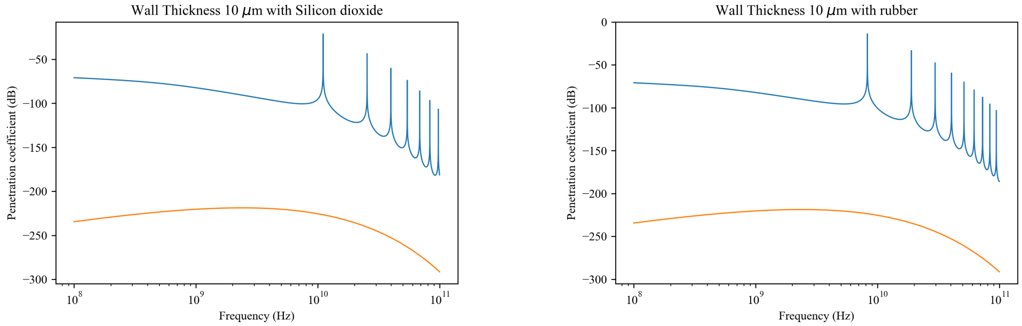

(a) Δ_{TM} for shell with $\epsilon_r = 3.9$. (b) Δ_{TM} for shell with $\epsilon_r = 7$.

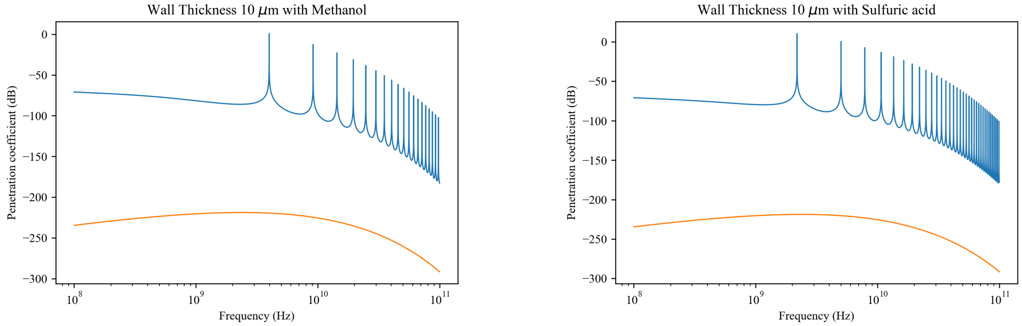

(c) Δ_{TM} for shell with $\epsilon_r = 30$. (d) Δ_{TM} for shell with $\epsilon_r = 100$ at 25° C.

Figure 2.19: The variation in penetration frequencies due to material inside the shell.

The discrete frequencies increased penetration change due to variation in the dielectric constant of the material inside the shell (see figure 2.19). Hence, these structures can be engineered to interact with the incident wave of certain discrete frequencies, similar to quantized energy levels of a atom. Since, wave can interact with the material inside it provides another degree of freedom to design meta-atom, where the electromagnetic energy can be localized inside the shell. This method can used to detect the material inside container because theoretical calculations would predict the frequencies at which the wave to detect the material and any variation would change the response of the meta-atom. The material inside can be linear, non-linear or active gain medium which would produce a new generation of non-linear meta-structures.

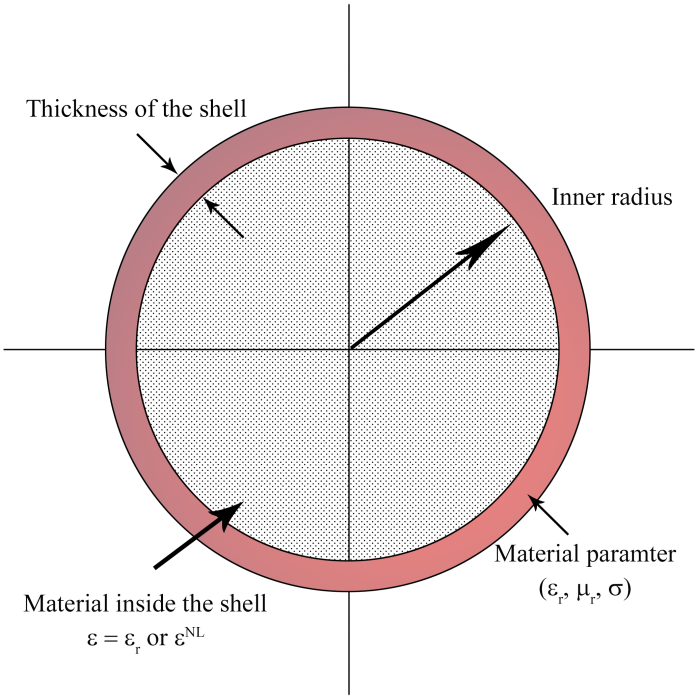

Figure 2.20: Degrees of freedom for designing meta-atoms with responses at discrete frequencies.

Lets consider an example where the material inside the shell is anisotropic in nature with weak $\chi^{(3)}$ non-linearity leading to a response to incident wave $\mathbf{E}(t) = \Re[\mathbf{E}_\omega e^{-i\omega t}]$ is given by,

$$\mathbf{D}(t) = \Re[\epsilon_0(\epsilon_1 + \frac{3}{4}\chi^{(3)}|\mathbf{E}_\omega|^2)\mathbf{E}_\omega e^{-i\omega t}] \tag{2.85}$$

Remembering that the fields can only penetrate at certain frequencies, a particle of this geometry can act as linear as well as non-linear structure depending only on the incident frequency. In the cases where the frequencies can be altered by ϵ^{NL}, the field coupled inside the shell may not be able to propagate out which in theory should localization of electromagnetic energy and hence introduce thermal effects and observation of light. Another interaction analysis would be interactions of pulsed waves with these structures and its temporal dynamics of localization of the electromagnetic energy.

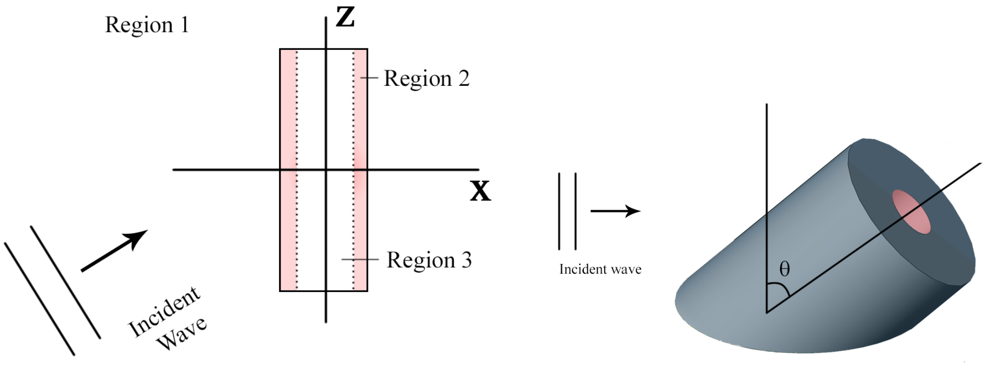

(a) Wave incident at certain angle to the normal of cylinders.

(b) Normal wave incident at the angle angled cylinders.

Figure 2.21: Mixing of eigenfrequencies by adding the degree of freedom of angle of incidence.

Using the properties of scattering by waves incident angle where a TM fields produces both TE and TM scattered fields and the knowledge that the resonance conditions (figure 2.18) for TE and TM modes are different, we design a meta-atoms which has response which cannot be obtained by one filed only. The penetration coefficient has to be combination of both d_n and h_n hence will provide another design parameter. In addition to engineering meta-atoms, the results obtained have implications fundamental limits of the response [54], such as absorption per volume is incomplete because it does not consider the geometry.

$$\frac{P_{abs}}{V} \leq \omega E_{in} \frac{|\chi(\omega)|^2}{\Im[\chi(\omega)]} \tag{2.86}$$

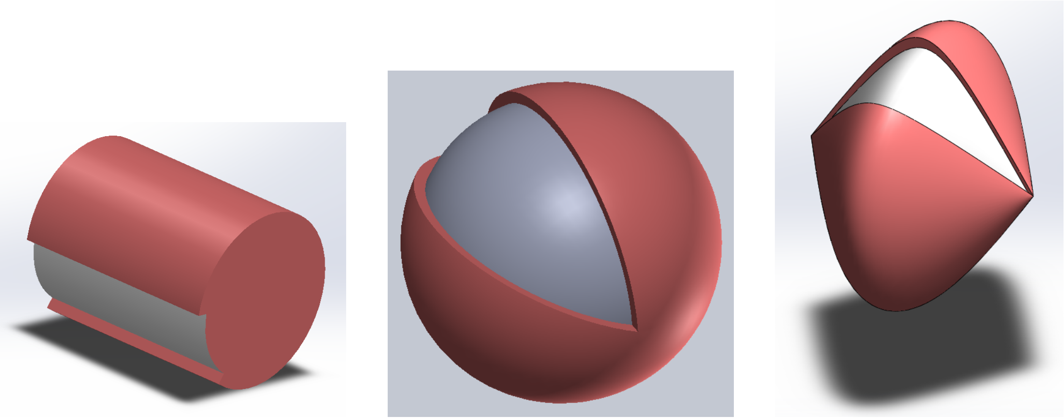

(a) Cylindrical shell. (b) Spherical shell. (c) Oblate shell.

Figure 2.22: Examples of other geometry which can be used to design meta-atoms.

Other geometry can also be analyzed similarly by using spherical wavefunctions in terms of spherical Bessel functions $z_n(kr)$ and associated Legendre functions $P_n^m(\cos\theta)$, for example for spheres

$$\psi(r) = z_n(kr)P_n^m(\cos\theta)e^{im\phi} \tag{2.87}$$

In the next chapter, we discuss an elegant way to investigate the propagation of fields using Green's functions and electromagnetic potential through an object of arbitrary geometry as shown in figure 2.22.

CHAPTER 3: PROPAGATION OF POTENTIALS

In chapter 2, we saw that the well known formulation for interaction of electromagnetic waves with shells is incomplete. Experimental and theoretical analysis of cylindrical shells illustrates the importance of geometry in the formalism of scattering. The exact study of propagation of fields through a structures of various geometries is arduous and changes for every case based on geometry. Hence, it seems imperative to develop a formalism capable of describing a large number of geometries which can be helpful in analyzing metamaterials. The process of designing metamaterials focuses on achieving certain responses to the incident waves from structures fabricated from a variety of materials. In the design process the spatial (or temporal) transfer function is tailored to meet demands of a specific application. The design process can also be performed in the spatial domain using Green's functions of individual and collections of meso-structures or nano-structures. In recent years, Green's functions have been used to design metamaterials to perform mathematical operations [55], and hyperbolic metamaterials for quantum nanophotonics [56].

The geometries of individual unit cells are becoming increasingly complicated with advancements in metamaterials which requires a rigorous technique capable of handling these exotic geometries. Fabrication of metamaterials also pose an issue of characterization of properties of the manufactured structures or materials. This creates a need to extend inverse methods to determine the properties such as local and global variation of permittivity, and permeability. In the inverse problem, the properties are determined from the measured intensity which leads to problems related to sampling, and convergence of solution [57]. Strong scattering and penetration of incident field inside the scattering object leads to violation of many approximations

[58]. More recent literature [45] suggests use of cepstral filtering to improve inverse methods to determine the spatial distribution of permittivtiy, and permeability which requires working in the Fourier domain. Exotic properties of meta-atoms and metamaterials are often achieved by driving them at frequencies very close to the resonance frequencies of the structures. Solutions of inverse problems becomes arduous because various linear approximations such as the first Born approximation break down. This means resorting to non linear algorithms for numerical calculations which are computationally expensive. Hence, it would be desirable to develop rapid methods to solve the inverse problems in resonance regions, such as Herglotz wavefunctions [59]. The Green's functions methods can be used to solve the inverse problems in real space and use of same the formulation for design and characterization of metamaterials can help identity errors in fabrication.

Direct and inverse problems become very difficult when the size of the structures becomes comparable to the wavelength because common electromagnetic scattering approximations break down [60] which makes it imperative to build a framework from first principles without any hidden approximations. Usually, numerical methods in electric and magnetic vector $\mathbf{E}(\mathbf{r}, t)$ - $\mathbf{H}(\mathbf{r}, t)$ formulations are used in metamaterial design and characterization. These methods suffer from breakdown at low-frequencies [61] or when the dimensions of structures become much smaller than the wavelength. Similar problems might occur when structures have highly subwavelength coatings which also leads to high computing costs in field formulations. These issues can be resolved by using scalar $\Phi(\mathbf{r}, t)$ and vector $\mathbf{A}(\mathbf{r}, t)$ electromagnetic potentials [62, 63, 64].

Traditionally, electromagnetic potentials are used to reduce the mathematical complexity of the problem and used to be widely believed that potentials have no physical meaning. But the Aharanov-Bohm effect [65] demonstrates that vector potentials carry physical meaning at quantum levels. Subsequent research has shown its equvalence in water waves [66], and its usefulness in graphene [67] and photonics [68]. This raises an interesting question: can electromagnetic potentials be used to render new properties to metamaterials? In order to explore the usage of potentials in metamaterial design and characterization, they have to be established on the same footing as fields. Hence, there is a need to understand the properties of potentials in an inhomogeneous medium and across boundaries. In this chapter, a method for propagation of potentials of across a boundary of arbitrary geometry using Green's function including boundary conditions are presented.

3.1 Gauge Transformations

The variation or propagation of electromagnetic fields in space and time is governed by Maxwell's equations and the behavior of materials characterized by permittivity $\overleftrightarrow{\epsilon}$ and permeability $\overleftrightarrow{\mu}$ under the influence of fields is dictated by constitutive relations. These characteristic parameters can take tensor form for complex materials but in this chapter we are considering material with spatially varying scalar permittivity $\epsilon(\mathbf{r})$ and permeability $\mu(\mathbf{r})$. Magnetic induction $\mathbf{B}(\mathbf{r},t)$ is always solenoidal, hence it can be expressed in terms of vector potential as

$$\mathbf{B}(\mathbf{r},t) = \nabla \times \mathbf{A}(\mathbf{r},t) \tag{3.1}$$

As a consequence of the Maxwell-Faraday equation, the displacement vector can be expressed as

$$\mathbf{D}(\mathbf{r},t) = -\frac{1}{\epsilon(\mathbf{r})}[\nabla\Phi(\mathbf{r},t) + \frac{\partial}{\partial t}\mathbf{A}(\mathbf{r},t)] \tag{3.2}$$

Using these definitions in Maxwell's equations, coupled equations for electromagnetic potentials generated by electric current density $\mathbf{j}(\mathbf{r},t)$, and localized charge density $\rho(\mathbf{r},t)$ in a inhomogeneous medium can be expressed as

$$\nabla \cdot \epsilon(\mathbf{r})\nabla\Phi(\mathbf{r},t) - \frac{\partial}{\partial t}[\nabla \cdot \epsilon(\mathbf{r})\mathbf{A}(\mathbf{r},t)] = -\rho(\mathbf{r},t) \tag{3.3}$$

$$\nabla \times \frac{1}{\mu(\mathbf{r})}\nabla \times \mathbf{A}(\mathbf{r},t) + \epsilon(\mathbf{r})\frac{\partial^2}{\partial t^2}\mathbf{A}(\mathbf{r},t) + \frac{\partial}{\partial t}[\epsilon(\mathbf{r})\nabla\Phi(\mathbf{r},t)] = -\mathbf{j}(\mathbf{r},t) \tag{3.4}$$

The use of potentials introduces an inherent non-uniqueness giving rise to freedom of gauge for the scalar and vector potential

$$\phi'(\mathbf{r},t) = \phi(\mathbf{r},t) - \frac{\partial}{\partial t}\chi(\mathbf{r},t) \tag{3.5}$$

$$\mathbf{A}'(\mathbf{r},t) = \mathbf{A}(\mathbf{r},t) + \nabla\chi(\mathbf{r},t) \tag{3.6}$$

where, the gauge function $\chi(\mathbf{r},t)$ can assume various functional forms. In classical electromagnetics, it is widely believed that gauge transformations are mathematical constructs and have no physical meaning, and are used to simplify the problem. A comprehensive review [69] of gauge invariance highlights the ambiguity in usage of gauges going back to the Lorenz gauge. Subsequent papers [70, 71] show that choice of a certain gauge imposes certain physical restrictions on the solution for potentials. From equations 3.3 and 3.4, it is clear that electromagnetic potentials originating from a source should propagate under the rules of causality, and relativity, satisfying appropriate boundary conditions for discontinuity in $\epsilon(\mathbf{r})$ and $\mu(\mathbf{r})$.

The propagation speed of scalar potentials has been an interesting topic of research and plays an important role in velocity gauges, where the speed can be chosen to propagate at any speed relative to speed of light (c). The issue of causality of a scalar potential was resolved by decomposing the current density into transverse and longitudinal parts [72] which is a consequence of a subsidiary condition imposed on the potentials. The vector potential can also be decomposed in longitudinal and transverse components, and the longitudinal component travels at 'c' and transverse component can propagate at arbitrary speed. The velocity gauge (see equation 3.7) uses a parameter 'v' to manipulate the propagation speed of potentials. Under the velocity gauge, 'v' parameter controls the propagation speed of potentials which can provide an opportunity to manipulate the response of materials in a novel way. Violation of gauge invariance can be linked to violation of causality, and relativity. Despite the arbitrary speed of scalar potentials in the velocity gauge, it still has a physical meaning [73] as $\mathbf{E}(\mathbf{r}, t)$ still follows the laws of relativity.

$$\frac{1}{\epsilon(\mathbf{r})}\nabla \cdot \epsilon(\mathbf{r})\mathbf{A}^{(v)}(\mathbf{r}, t) + \mu(\mathbf{r})\epsilon(\mathbf{r})\frac{c^2}{v^2}\frac{\partial}{\partial t}\Phi^{(v)}(\mathbf{r}, t) = 0 \tag{3.7}$$

The underpinning concept of metamaterial design is to have controlled spatial variation of $\epsilon(\mathbf{r})$ and $\mu(\mathbf{r})$, which perhaps can be manipulated with electromagnetic potentials and gauge transformations, providing a new avenue to metamaterial design by using photonic Aharanov-Bohm effect [74, 75, 76]. The Aharanov-Bohm effect can also be observed in plasmons leading to oscillations in plasmons' frequencies [77], and wavefront disloctions in scattering of surface plsmons from topological defect [78]. Traditionally potentials have been used to calculate fields due to a source in an infinite homogeneous medium but here propagation of potentials across a boundary is discussed.

Coulomb and Lorenz gauges are two most commonly used gauges in electromagnetic theory. The Coulomb gauge can be derived from velocity gauge if $v \rightarrow \infty$,

$$\frac{1}{\epsilon(\mathbf{r})}\nabla \cdot \epsilon(\mathbf{r})\mathbf{A}^{(C)}(\mathbf{r}, t) = 0 \tag{3.8}$$

The issue of causality of scalar potentials under the Coulomb gauge becomes apparent when it is used in equation 3.3. But the subsidiary condition $\nabla \cdot \mathbf{A}_{\perp}(\mathbf{r}, t) = 0$

[72] corrects the causality of retarded potentials. Upon decomposing vector potentials in gradient and curl components using Helmholtz theorem (see Appendix C), it can be shown that a gradient component can be altered during gauge transformations [71] and does not generate a magnetic field hence should not appear when potentials cross a boundary. These complications in the nature of propagation potentials under Coulomb gauge makes the use of Lorenz gauge logical.

The Lorenz gauge can be obtained from the velocity gauge when $v = c$ and it treats potentials as waves, originating from a source subject to causality and relativity conditions.

$$\frac{1}{\epsilon(\mathbf{r})}\nabla \cdot \epsilon(\mathbf{r})\mathbf{A}^{(L)}(\mathbf{r}, t) + \mu(\mathbf{r})\epsilon(\mathbf{r})\frac{\partial}{\partial t}\Phi^{(L)}(\mathbf{r}, t) = 0 \tag{3.9}$$

Applying the Lorenz gauge conditions in equations 3.3 and 3.4, we get two decoupled equations for potentials in an inhomogeneous medium

$$\nabla \cdot \epsilon(\mathbf{r})\nabla\Phi(\mathbf{r}, t) - \mu(\mathbf{r})\epsilon(\mathbf{r})\frac{\partial^2}{\partial t^2}\Phi(\mathbf{r}, t) = -\rho(\mathbf{r}, t) \tag{3.10}$$

$$\nabla \times \frac{1}{\mu(\mathbf{r})}\nabla \times \mathbf{A}(\mathbf{r}, t) - \epsilon(\mathbf{r})\frac{\partial^2}{\partial t^2}\mathbf{A}(\mathbf{r}, t) + \nabla[\frac{1}{\mu(\mathbf{r})\epsilon(\mathbf{r})}\nabla \cdot \epsilon(\mathbf{r})\mathbf{A}(\mathbf{r}, t)] = -\mathbf{j}(\mathbf{r}, t) \tag{3.11}$$

3.2 Boundary Conditions

An inhomogeneous medium can be treated as a piece-wise homogeneous medium where potentials in various homogeneous regions can be stitched together using boundary conditions. In general, boundary conditions are derived using integration over infinitesimal surface or volume elements using Gauss', and Stokes' theorem. It is important to note that boundary conditions for perfect conductors ($\sigma \to \infty$) and imperfect or real conductor (σ is finite) are different. In this chapter, the primary concern is to deal with real materials, implying finite conductivity hence over a infinitesimal region current and charge densities drop to zero. All information about the behavior at an interface is encapsulated in the equations above and can be solved by various numerical methods including finite element methods.

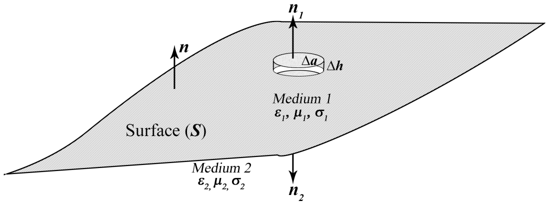

Figure 3.1: Infinitesimal contour for surface integration.

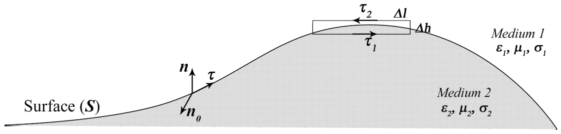

Figure 3.2: Infinitesimal volume for volume integration.

In order to have physical significance, the effects of electromagnetic potentials should be unaffected under gauge transformations, including the boundary conditions. Hence, the boundary conditions are derived from the uncoupled equations to ensure independence from gauge transformations. Using divergence theorem in 3.12 and methods expounded in many textbooks over an infinitesimal volume shown in figure 3.1

$$\oint_V [\nabla \cdot \epsilon(\mathbf{r}) \nabla \Phi(\mathbf{r}, t)] dV - \frac{\partial}{\partial t} \oint_V [\nabla \cdot \epsilon(\mathbf{r}) \mathbf{A}(\mathbf{r}, t)] dV = - \oint_V [\rho(\mathbf{r}, t)] dV \tag{3.12}$$

From equation 3.12, at the boundary with finite conductivity, condition for scalar potential at the boundary

$$\hat{\mathbf{n}} \cdot [\epsilon_2(\mathbf{r}) \nabla \Phi_2(\mathbf{r}, t) - \epsilon_1(\mathbf{r}) \nabla \Phi_1(\mathbf{r}, t)] = 0 \tag{3.13}$$

Due to the finitness of $\nabla \cdot \epsilon(\mathbf{r})\mathbf{A}(\mathbf{r},t)$ at the boundary we obtain a necessary condition,

$$\hat{\mathbf{n}} \cdot [\epsilon_2(\mathbf{r})\mathbf{A}_2(\mathbf{r},t) - \epsilon_1(\mathbf{r})\mathbf{A}_1(\mathbf{r},t)] = 0 \tag{3.14}$$

The integration in equation 3.15 is over an infinitesimal surface, with rectangular path $\mathbf{C_0}$ shown in figure 3.2 in limit $\Delta h \to 0$ and tangent vector $\hat{\tau} = \hat{\mathbf{n}}_0 \times \hat{\mathbf{n}}$

$$\begin{gathered}\int_{\mathbf{C_0}} [\nabla \times \frac{1}{\mu(\mathbf{r})} \nabla \times \mathbf{A}(\mathbf{r},t)] \cdot d\mathbf{S} + \frac{\partial^2}{\partial t^2} \int_{\mathbf{C_0}} [\epsilon(\mathbf{r})\mathbf{A}(\mathbf{r},t)] \cdot d\mathbf{S} \\ + \frac{\partial}{\partial t} \int_{\mathbf{C_0}} [\epsilon(\mathbf{r})\nabla\Phi(\mathbf{r},t)] \cdot d\mathbf{S} = -\int_{\mathbf{C_0}} [\mathbf{j}(\mathbf{r},t)] \cdot d\mathbf{S}\end{gathered} \tag{3.15}$$

From equation 3.15, it is clear that $\nabla \cdot \epsilon(\mathbf{r})\mathbf{A}(\mathbf{r},t)$ and $\nabla \times \mathbf{A}(\mathbf{r},t)$ have to be finite at the surface. Considering, $\epsilon(\mathbf{r})\frac{\partial^2}{\partial t^2}\mathbf{A}(\mathbf{r},t)$ on a infinitesimal surface area at the interface leads to the first boundary condition, where $\hat{\mathbf{n}}$ is a unit vector normal to the surface.

$$\hat{\mathbf{n}} \times [\mathbf{A}_2(\mathbf{r},t) - \mathbf{A}_1(\mathbf{r},t)] = 0 \tag{3.16}$$

A surface with finite conductivity leads to finite $\mathbf{j}(\mathbf{r},t)$ combined with $\nabla[\times \frac{1}{\mu(\mathbf{r})} \nabla \times \mathbf{A}(\mathbf{r},t)]$ leads to

$$\hat{\mathbf{n}} \times [\frac{1}{\mu_2(\mathbf{r})} \nabla \times \mathbf{A}_2(\mathbf{r},t) - \frac{1}{\mu_1(\mathbf{r})} \nabla \times \mathbf{A}_1(\mathbf{r},t)] = 0 \tag{3.17}$$

Observing $\frac{\partial^2}{\partial t^2}\Phi(\mathbf{r},t)$, we get another boundary condition,

$$\Phi_2(\mathbf{r},t) = \Phi_1(\mathbf{r},t) \Rightarrow \hat{\mathbf{n}} \times [\nabla\Phi_2(\mathbf{r},t) - \nabla\Phi_1(\mathbf{r},t)] = 0 \tag{3.18}$$

The same boundary conditions can be obtained using the differentiation method outlined in refernce [79]. It is notable that the boundary conditions for vector potentials are dependent only on the curl component and not on the gradient component which can be affected by gauge transformations. These conditions can very easily be translated to boundary conditions for fields [38].

The next step is to build a framework that embodies all the physical restrictions imposed on the electromagnetic potential waves during propagation once it is generated by the source. An elegant way to express the propagation of vector fields generated by a source located at $\mathbf{r}'$ is the dyadic Green's function $\overleftrightarrow{\mathbb{G}}(\mathbf{r}, \mathbf{r}'|t, t')$. There are no assumptions made during the solution, hence it does not break down when dimensions of the scattering object become comparable to the wavelength.

3.3 Dyadic Green's Functions for Electromagnetic Potentials

In general, Green's function is a kernel in an integral which transforms the boundary conditions and/or the source density into the solution. When the solution is supposed to be a scalar then the kernel could be a scalr but when the source function and the boundary conditions are vectors then the kernels has to be a vector operator or dyadic. Using the concept of eigenfunctions and Green's functions it can be argued that boundary conditions can be expressed as a vector in abstract vector space and Green's function transforms the boundary values into values of the solution. The dyadic Green's function $\overleftrightarrow{\mathbb{G}}(\mathbf{r}, \mathbf{r}'|t, t')$ must satisfy the following properties, reciprocity relations, generate solutions from boundary conditions and source functions and the resulting solutions must have discontinuities just outside the boundaries which has been illustrated by scalar example.

$$\nabla^2\overleftrightarrow{\mathbb{G}}(\mathbf{r}, \mathbf{r}'|t, t') + k^2\overleftrightarrow{\mathbb{G}}(\mathbf{r}, \mathbf{r}'|t, t') = -\overleftrightarrow{\mathbb{I}}(\mathbf{r}, \mathbf{r}'|t, t') \tag{3.19}$$

In an inhomogeneous medium, we consider a medium containing the source total field of incident and scattered fields, and the transmitted field in a non-source region. In general scattering problems the superposition principle is used to satisfy the required boundary and radiation conditions for incident and scattered fields [80]. The method of scattering superposition is also valid for Green's functions [81] as it has to satisfy the same homogeneous or inhomogeneous Helmholtz equations, boundary and radiation conditions. The method of scattering superposition which is valid for any geometry can understood by simple 1D case for scalar Green's function. Scalar Green's function $g(x|x')$ for one dimension with source at x' can be written as sum of free space $g_0(x|x')$ and scattered Green's functions of the form Fe^{ikx}. Assuming that the field goes to zero at $x = 0$ and satisfies Neumann boundary conditions, it can be easily shown the that total Green's function becomes the sum of free space and scattered functions.

$$g(x|x') = \begin{cases} \frac{i}{2k}[e^{ik(x-x')} + e^{ik(x+x')}], & x \geq x' \\ \frac{i}{2k}[e^{-ik(x-x')} + e^{ik(x+x')}], & x' \geq x \geq 0 \end{cases} \tag{3.20}$$

After establishing the method of scattering superposition, a method applicable to a scattering object of arbitrary geometry employing an eigenfunction expansion of a dyadic Green's function using Hansen vector wavefunctions [82] is developed. Key components of this formulation are a scalar generating function $\psi_{pqs}(\mathbf{r})$ which should satisfy the homogeneous Helmholtz equation with eigenvalues (k_{pqs}) in a coordinate system determined by the geometry of the scattering object, and a constant piloting vector $\hat{\mathbf{a}}$. Vector wave-functions are classified as Cartesian vector wave-function if the piloting vector can be $\hat{\mathbf{x}}$, $\hat{\mathbf{y}}$, and $\hat{\mathbf{z}}$ and a spherical vector wave-function if the piloting vector is radial vector $\hat{\mathbf{r}}$. Three vector functions required for the decomposition of dyadic Green's function can be represented using an vector operator $\tilde{\mathbf{T}}$ and is obtained from the scalar generating function.

$$\mathbf{L}_{pqs}(\mathbf{r}) = \nabla\psi_{pqs}(\mathbf{r}) = \tilde{\mathbf{T}}_L\psi_{pqs}(\mathbf{r}) \tag{3.21}$$

$$\mathbf{M}_{pqs}(\mathbf{r}) = \nabla \times \hat{\mathbf{a}}\psi_{pqs}(\mathbf{r}) = \tilde{\mathbf{T}}_M\psi_{pqs}(\mathbf{r}) \tag{3.22}$$

$$\mathbf{N}_{pqs}(\mathbf{r}) = \frac{1}{k_{pqs}} \nabla \times \mathbf{M}_{pqs}(\mathbf{r}) = \tilde{\mathbf{T}}_N \psi_{pqs}(\mathbf{r}) \tag{3.23}$$

Immediately some properties of the eigenfunctions can be inferred, $\mathbf{L}_{pqs}(\mathbf{r})$, $\mathbf{M}_{pqs}(\mathbf{r})$, and $\mathbf{N}_{pqs}(\mathbf{r})$ are not colinear and

$$\nabla \cdot \mathbf{M}_{pqs}(\mathbf{r}) = \nabla \cdot \mathbf{N}_{pqs}(\mathbf{r}) = 0 \tag{3.24}$$

Using vector identities it can be shown that all three eigenfunctions satisfy the same Helmholtz equation as $\psi_{pqs}(\mathbf{r})$, and $\mathbf{L}_{pqs}(\mathbf{r})$ has an infinitely degenerate eigenvalue of zero.

$$[\nabla^2 + k_{pqs}^2] \begin{bmatrix} \psi_{pqs}(\mathbf{r}) \\ \mathbf{L}_{pqs}(\mathbf{r}) \\ \mathbf{M}_{pqs}(\mathbf{r}) \\ \mathbf{N}_{pqs}(\mathbf{r}) \end{bmatrix} = 0 \tag{3.25}$$

These eigenfunctions have to be supplied with proper normalization factors which depend on the geometry of the scattering object, because the eigenfunction expansion of every vector field has to be supported by a completeness condition [83]. Normalization factors for each eigenfunction can be written as

$$\langle \mathbf{L}_{pqs}(\mathbf{r}); \mathbf{L}^*_{pqs}(\mathbf{r}) \rangle = \Lambda^L_{pqs} \tag{3.26}$$

$$\langle \mathbf{M}_{pqs}(\mathbf{r}); \mathbf{M}^*_{pqs}(\mathbf{r}) \rangle = \Lambda^M_{pqs} \tag{3.27}$$

$$\langle \mathbf{N}_{pqs}(\mathbf{r}); \mathbf{N}^*_{pqs}(\mathbf{r}) \rangle = \Lambda^N_{pqs} \tag{3.28}$$

The completeness condition for eigenfunction expansion is

$$\bar{\mathbf{I}}\delta(\mathbf{r}-\mathbf{r}') = \sum[\frac{\mathbf{L}_{pqs}(\mathbf{r})\mathbf{L}^*_{pqs}(\mathbf{r}')}{\Lambda^L_{pqs}} + \frac{\mathbf{M}_{pqs}(\mathbf{r})\mathbf{M}^*_{pqs}(\mathbf{r}')}{\Lambda^M_{pqs}} + \frac{\mathbf{N}_{pqs}(\mathbf{r})\mathbf{N}^*_{pqs}(\mathbf{r}')}{\Lambda^N_{pqs}}] \tag{3.29}$$

The expansion of a dyadic Green's function can be very easily used to decompose it into longitudinal terms containing $\mathbf{L}_{pqs}(\mathbf{r})$ and transverse with terms of $\mathbf{M}_{pqs}(\mathbf{r})$ and $\mathbf{N}_{pqs}(\mathbf{r})$. This mathematical framework for propagation of electromagnetic potentials can be understood with the help of an example.

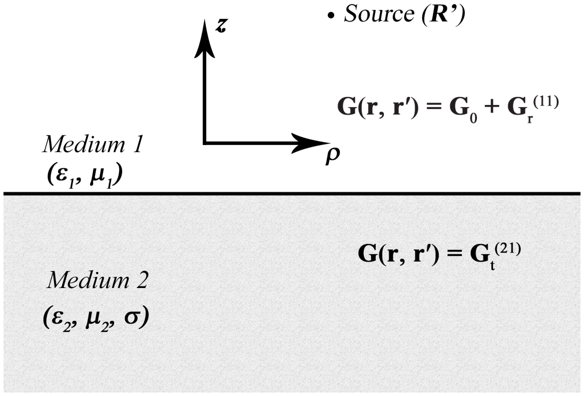

Figure 3.3: Illustration of two semi-finite half spaces with source present in medium 1.

Consider two semi infinite half spaces (see fig. 3.3) where medium 1 is characterized by (ϵ_1, μ_1) and medium 2 by $(\epsilon_2, \mu_2, \sigma)$. A time harmonic point source $(e^{-i\omega t})$ of frequency ω is present at $\mathbf{R}'$ in medium 1 emitting a three dimensional field. The 2D geometry of the problem requires a Fourier transform in $\hat{\mathbf{y}}$ which is used to represent the 3D incident field from a point source in the same geometry as the boundary [84], which makes the use cylindrical generating function (equation 3.30) logical. The Ohm-Rayleigh method [85] will be used to decompose the dyadic Green's function using anterior and posterior vector coefficients to satisfy the radiation and boundary conditions.

$$\psi_{pqs}(\mathbf{r}) = J_p(s\rho)e^{ip\phi}e^{-iqz} \tag{3.30}$$

where, $J_p(s\rho)$ is a Bessel function, radial spectral variable ($s \in (0, \infty)$), longitudinal spectral variable ($q \in (-\infty, \infty)$), integral azimuthal spectral variable ($p \in (-\infty, \infty)$), hence the eigenvalues $k^2_{pqs} = q^2 + s^2$. Using the scalar function, normalization factors can be calculated, where $\delta_{pp'}$ is the Kronecker delta function. In order to calculate the normalization constants let's expand the vector wavefunctions in terms of individual functions.

$$\mathbf{L}_{pqs}(\rho, \phi, z) = [J'_p(s\rho)\hat{\boldsymbol{\rho}} + \frac{ip}{\rho} J_p(s\rho)\hat{\boldsymbol{\phi}} - iqJ_p(s\rho)\hat{\mathbf{z}}]e^{ip\phi}e^{-iqz} \tag{3.31}$$

$$\mathbf{M}_{pqs}(\rho, \phi, z) = [\frac{ip}{\rho} J_p(s\rho)\hat{\boldsymbol{\rho}} - iqJ'_p(s\rho)\hat{\boldsymbol{\phi}}]e^{ip\phi}e^{-iqz} \tag{3.32}$$

$$\mathbf{N}_{pqs}(\rho, \phi, z) = \frac{1}{k_{pqs}}[-iqsJ'_p(s\rho)\hat{\boldsymbol{\rho}} + \frac{pq}{\rho} J_p(s\rho)\hat{\boldsymbol{\phi}} + s^2 J_p(s\rho)\hat{\boldsymbol{z}}]e^{ip\phi}e^{-iqz} \tag{3.33}$$

Now using the definition of normalization constant and properties of Bessel's functions, we can show that

$$`\Lambda^L_{pqs} = 4\pi^2 \frac{s^2 + q^2}{s} \delta(s - s')\delta(q - q')\delta_{pp'} \tag{3.34}$$

$$`\Lambda^M_{pqs} = `\Lambda^N_{pqs} = 4\pi^2 s\delta(s - s')\delta(q - q')\delta_{pp'} \tag{3.35}$$

Its is important to realize that the vector wavefunctions are orthogonal to each other and using Ohm-Rayleigh method, posterior coefficients we can write

$$\overleftrightarrow{\mathbb{I}}(\mathbf{r} - \mathbf{r}') = \int_0^\infty ds \int_\infty^\infty dq \sum_{p=-\infty}^{\infty} [\mathbf{L}_{pqs}(\mathbf{r})\mathbf{A} + \mathbf{M}_{pqs}(\mathbf{r})\mathbf{B} + \mathbf{N}_{pqs}(\mathbf{r})\mathbf{C}] \tag{3.36}$$

Taking a dot product of the equation with $\mathbf{L}^*_{p'q's'}(\mathbf{r})$ and integrating over the entire volume, and normalization factors, and repeating the steps for $\mathbf{M}^*_{p'q's'}(\mathbf{r})$ and $\mathbf{N}^*_{p'q's'}(\mathbf{r})$, we get

$$\mathbf{A} = \frac{s}{4\pi^2(s^2+q^2)}\mathbf{L}_{-p-qs}(\mathbf{r}') \tag{3.37}$$

$$\mathbf{B} = \frac{s}{4\pi^2}\mathbf{M}_{-p-qs}(\mathbf{r}') \tag{3.38}$$

$$\mathbf{C} = \frac{s}{4\pi^2}\mathbf{N}_{-p-qs}(\mathbf{r}') \tag{3.39}$$

Hence, the unit Dyadic in this geometry is

$$\begin{aligned}\overleftrightarrow{\mathbb{I}}(\mathbf{r}-\mathbf{r}') = \int_0^\infty ds \int_{-\infty}^\infty dq \sum_{p\to-\infty}^{\infty} [\frac{s\mathbf{L}_{pqs}(\mathbf{r})\mathbf{L}_{-p-qs}(\mathbf{r}')}{4\pi^2(s^2+q^2)} + \\ \frac{\mathbf{M}_{pqs}(\mathbf{r})\mathbf{M}_{-p-qs}(\mathbf{r}')}{4\pi^2 s} + \frac{\mathbf{N}_{pqs}(\mathbf{r})\mathbf{N}_{-p-qs}(\mathbf{r}')}{4\pi^2 s}]\end{aligned} \tag{3.40}$$

The Green's function in a piece-wise continuous medium and should satisfy the same equation as vector potentials, using vector identities equation 3.11 can be rewritten in space-frequency domain where, $k_i^2 = \omega^2\epsilon_i\mu_i$

$$\nabla^2\overleftrightarrow{\mathbb{G}}(\mathbf{r},\mathbf{r}') - \nabla\nabla\cdot\overleftrightarrow{\mathbb{G}}(\mathbf{r},\mathbf{r}') - k_i^2\overleftrightarrow{\mathbb{G}}(\mathbf{r},\mathbf{r}') = \overleftrightarrow{\mathbb{I}}\delta(\mathbf{r}-\mathbf{r}') \tag{3.41}$$

Using anterior vector coefficients for vector eigenfunctions to satisfy the radiation and boundary conditions, then Green's functions can be written as,

$$\overleftrightarrow{\mathbb{G}}(\mathbf{r}-\mathbf{r}') = \int_0^\infty ds \int_\infty^\infty dq \sum_{p=-\infty}^{\infty} [\mathbf{a}_{pqs}\mathbf{L}_{pqs}(\mathbf{r}) + \mathbf{b}_{pqs}\mathbf{M}_{pqs}(\mathbf{r}) + \mathbf{c}_{pqs}\mathbf{N}_{pqs}(\mathbf{r})] \tag{3.42}$$

Using the expression for the unit dyadic and the properties of the vector wavefunctions

$$\nabla \times \mathbf{L}_{pqs}(\mathbf{r}) = 0 \qquad \nabla \cdot \mathbf{L}_{pqs}(\mathbf{r}) = \nabla^2 \psi_{pqs}(\mathbf{r}) = -k_{pqs}^2 \psi_{pqs}(\mathbf{r}) \tag{3.43}$$

$$\nabla \times \nabla \times \mathbf{N}_{pqs}(\mathbf{r}) = k_{pqs}^2 \mathbf{N}_{pqs}(\mathbf{r}) \tag{3.44}$$

Substituting 3.42 in the equation 3.41, the dyadic Green's function can be expressed as

$$\begin{aligned} \overset{\leftrightarrow}{\mathbb{G}}(\mathbf{r},\mathbf{r}') = -\frac{1}{4\pi^2}\int_0^\infty ds \int_{-\infty}^\infty dq \sum_{p\to-\infty}^{\infty} [\frac{s\mathbf{L}_{pqs}(\mathbf{r})\mathbf{L}_{-p-qs}(\mathbf{r}')}{k_{pqs}^2(k^2-k_{pqs}^2)} \\ +\frac{\mathbf{M}_{pqs}(\mathbf{r})\mathbf{M}_{-p-qs}(\mathbf{r}')}{s(k^2-k_{pqs}^2)} + \frac{\mathbf{N}_{pqs}(\mathbf{r})\mathbf{N}_{-p-qs}(\mathbf{r}')}{s(k^2-k_{pqs}^2)}] \end{aligned} \tag{3.45}$$

The integration over wavenumbers depends on the orientation of the interface and boundary which separates the media. In this case it is along $\hat{\mathbf{z}}$, thus integration over the spectral variable q has to be carried out using contour integration and Jordan's lemma. Thus, the dyadic Green's function for semi-infinite half space, where posterior functions are used to satisfy radiation condition and anterior functions for boundary conditions.

$$\begin{aligned} \overset{\leftrightarrow}{\mathbb{G}}(\mathbf{r},\mathbf{r}') = \int_0^\infty ds \sum_{p\to-\infty}^{\infty} [\frac{-\mathbf{L}_{p(is)s}(\mathbf{r})\mathbf{L}_{-p(-is)s}(\mathbf{r}')}{4\pi k^2} - \\ \frac{s\mathbf{L}_{pvs}(\mathbf{r})\mathbf{L}_{-p-vs}(\mathbf{r}')}{4\pi v k^2} + \frac{i\mathbf{M}_{pts}(\mathbf{r})\mathbf{M}_{-p-ts}(\mathbf{r}')}{4\pi st} + \frac{i\mathbf{N}_{pts}(\mathbf{r})\mathbf{N}_{-p-ts}(\mathbf{r}')}{4\pi st}] \end{aligned} \tag{3.46}$$

where, $i = \sqrt{-1}$, $k^2 + s^2 = -v^2$ and $k^2 - s^2 = t^2$. It is apparent that there exists an extra term in the solution of the Green's function for potentials than for fields [86] and

$\mathbf{L}_{pqs}(\mathbf{r})$ cannot be ignored corroborating [82]. Total dyadic Green's functions using scattering superposition method with free space $\overline{\mathbf{G}}_0(\mathbf{r},\mathbf{r}')$ and scattering $\overline{\mathbf{G}}_s^{(i1)}(\mathbf{r},\mathbf{r}')$ dyadic Green's function is expressed as

$$\overset{\leftrightarrow}{\mathbb{G}}(\mathbf{r},\mathbf{r}') = \begin{cases} \overset{\leftrightarrow}{\mathbb{G}}_0(\mathbf{r},\mathbf{r}') + \overset{\leftrightarrow}{\mathbb{G}}_r^{(11)}(\mathbf{r},\mathbf{r}'), & z \geq 0 \\ \overset{\leftrightarrow}{\mathbb{G}}_t^{(21)}(\mathbf{r},\mathbf{r}'), & z \leq 0 \end{cases} \tag{3.47}$$

Applying the boundary conditions derived earlier with some algebraic manipulation the coefficients of reflection and transmission can be derived where $\mu_2 = \mu_1 = \mu_0$, a_r^L and a_t^L can be arbitrary and set to zero for this geometry.

$$a_r^M = \frac{t_1 - t_2}{t_1 + t_2} \qquad a_t^M = \frac{2t_1}{t_1 + t_2} \tag{3.48}$$

$$a_r^N = \frac{k_2^2 t_1 - k_1^2 t_2}{k_2^2 t_1 + k_1^2 t_2} \qquad a_t^N = \frac{2k_1 k_2 t_1}{k_2^2 t_1 + k_1^2 t_2} \tag{3.49}$$

Hence, the total Green's function for propagation across a boundary separating two semi-infinite half spaces

$$\begin{aligned} \overset{\leftrightarrow}{\mathbb{G}}^{(11)}(\mathbf{r},\mathbf{r}') = \int_0^\infty ds \sum_{p\to-\infty}^{\infty} [&\frac{i\mathbf{M}_{p-t_1s}(\mathbf{r})[\mathbf{M}_{pt_1s}(\mathbf{r}') + a_r^M \mathbf{M}_{p-t_1s}(\mathbf{r}')]}{4\pi s t_1} \\ &+ \frac{i\mathbf{N}_{p-t_1s}(\mathbf{r})[\mathbf{N}_{pt_1s}(\mathbf{r}') + a_r^N \mathbf{N}_{p-t_1s}(\mathbf{r}')]}{4\pi s t_1}] \qquad z \geq z' \\ = \int_0^\infty ds \sum_{p\to-\infty}^{\infty} [&\frac{i[\mathbf{M}_{pt_1s}(\mathbf{r}) + a_r^M \mathbf{M}_{p-t_1s}(\mathbf{r})]\mathbf{M}_{p-t_1s}(\mathbf{r}')}{4\pi s t_1} \\ + &\frac{i[\mathbf{N}_{pt_1s}(\mathbf{r}) + a_r^N \mathbf{N}_{p-t_1s}(\mathbf{r})]\mathbf{N}_{p-t_1s}(\mathbf{r}')}{4\pi s t_1}] \qquad z' \geq z \geq 0 \end{aligned} \tag{3.50}$$

$$\overset{\leftrightarrow}{\mathbb{G}}^{(21)}(\mathbf{r},\mathbf{r}') = \int_0^\infty ds \sum_{p\to-\infty}^{\infty} [a_t^M \frac{i\mathbf{M}_{pt_2s}(\mathbf{r})\mathbf{M}_{p-t_1s}(\mathbf{r}')}{4\pi st_2} + a_t^N \frac{i\mathbf{N}_{pt_2s}(\mathbf{r})\mathbf{N}_{p-t_1s}(\mathbf{r}')}{4\pi st_2}] \qquad z \leq 0 \tag{3.51}$$

This is an illustration of the framework for propagation of electromagnetic potentials presented in this paper. It can be very easily adapted to any geometry by using the boundary conditions derived in section 3 and appropriate scalar generating function. An important point is that the scalar variable will become discrete if the space is finite. The integration over spectral variables in the Green's function (equation 3.45) for an infinite medium will be summations for a finite medium, such as cylinders. This method can also be translated to a spherical scattering objects by changing the Bessel function to spherical Bessel function in generating function and radial piloting vector.

3.4 Conclusions

```
Mathematical Framework 2: Green's function method.
Input: Choose generating function $\psi_{pqs}(r)$ based on geometry.
for Vector wavefunctions do
    $\mathbf{L}_{pqs}(\mathbf{r}) = \nabla\psi_{pqs}(\mathbf{r})$    (3.52)
    $\mathbf{M}_{pqs}(\mathbf{r}) = \nabla \times \hat{\mathbf{a}}\psi_{pqs}(\mathbf{r})$    (3.53)
    $\mathbf{N}_{pqs}(\mathbf{r}) = \frac{1}{k_{pqs}}\nabla \times \mathbf{M}_{pqs}(\mathbf{r})$    (3.54)
Calculate the normalization constants, $\Lambda^L_{pqs}$, $\Lambda^M_{pqs}$ and $\Lambda^N_{pqs}$ Using the definition of $\overleftrightarrow{\mathbb{I}}$ and the equation below to calculate the general form of Green's functions
$\nabla^2\overleftrightarrow{\mathbb{G}}(\mathbf{r},\mathbf{r}') - \nabla\nabla\cdot\overleftrightarrow{\mathbb{G}}(\mathbf{r},\mathbf{r}') - k_i^2\overleftrightarrow{\mathbb{G}}(\mathbf{r},\mathbf{r}') = \overleftrightarrow{\mathbb{I}}\delta(\mathbf{r}-\mathbf{r}')$    (3.55)
General Green's functions,
$\overleftrightarrow{\mathbb{G}}(\mathbf{r},\mathbf{r}') = -\frac{1}{4\pi^2}\int_0^\infty ds\int_{-\infty}^{\infty} dq \sum_{p\to-\infty}^{\infty}[\frac{s\mathbf{L}_{pqs}(\mathbf{r})\mathbf{L}_{-p-qs}(\mathbf{r}')}{k_{pqs}^2(k^2-k_{pqs}^2)} + \frac{\mathbf{M}_{pqs}(\mathbf{r})\mathbf{M}_{-p-qs}(\mathbf{r}')}{s(k^2-k_{pqs}^2)} + \frac{\mathbf{N}_{pqs}(\mathbf{r})\mathbf{N}_{-p-qs}(\mathbf{r}')}{s(k^2-k_{pqs}^2)}]$    (3.56)
Integrate for the spectral variable which defines the direction of interface
for Planar interface do
    Using boundary conditions, we get coefficients
    $a_r^M = \frac{t_1-t_2}{t_1+t_2} \quad a_t^M = \frac{2t_1}{t_1+t_2} \quad a_r^N = \frac{k_2^2t_1-k_1^2t_2}{k_2^2t_1+k_1^2t_2} \quad a_t^N = \frac{2k_1k_2t_1}{k_2^2t_1+k_1^2t_2}$    (3.57)
Result: Exact geometrical dependence comes from $i=\sqrt{-1}$, $k^2+s^2=-v^2$ and $k^2-s^2=t^2$. The spectral variables depend on the dimensions of the scattering object and the coefficients depend on the product of wavenumuber and dimensions as shown in chapter 2.
```

In mathematical framework 2,we have summarized the method for the propagation of electromagnetic potentials across a boundary of arbitrary geometry is presented, establishing the propagation of potentials on the same footing as fields across boundary. No approximations were made regarding the size of scattering object and wavelength, making it applicable to any electromagnetic problem. Using potentials helps alleviate the problem of low frequency breakdown making it applicable to any scale, and for any materials. With the knowledge of sources and point of observation, potentials can be calculated as,

$$\mathbf{A}(\mathbf{r}) = \int \overset{\leftrightarrow}{\mathbb{G}}(\mathbf{r}, \mathbf{r}')\mathbf{j}(\mathbf{r}')d\mathbf{r}' \tag{3.58}$$

The vector potential can be be written as a linear combination of the vector eigenfunction

$$\mathbf{A}(\mathbf{r}) = \frac{1}{i\omega}\sum_{n=0}^{\infty}[a_n^L\mathbf{L}_{pqs}(\mathbf{r}) + a_n^M\mathbf{M}_{pqs}(\mathbf{r}) + a_n^N\mathbf{N}_{pqs}(\mathbf{r})] \tag{3.59}$$

and consequent electric and magnetic field vectors are given by

$$\mathbf{E}(\mathbf{r}) = \sum_{n=0}^{\infty}[a_n^M\mathbf{M}_{pqs}(\mathbf{r}) + a_n^N\mathbf{N}_{pqs}(\mathbf{r})] \tag{3.60}$$

$$\mathbf{H}(\mathbf{r}) = \frac{k}{i\omega\mu}\sum_{n=0}^{\infty}[a_n^M\mathbf{N}_{pqs}(\mathbf{r}) + a_n^N\mathbf{M}_{pqs}(\mathbf{r})] \tag{3.61}$$

This formulation can be used for any geometry, by replacing the scalar generating function based on geometry and coefficients 'a_n^i' serving as reflection and transmission coefficients. The complex integration over spectral variables have to be carried out to capture near field effects. For far zone fields, asymptotic expressions for Bessel functions can be used to simplify the problem.

For rectangular geometry, the generating function is combination of sines and cosines and can be expressed as

$$\psi_{pqs}(r) = \sin(\frac{p\pi x}{a})\sin(\frac{s\pi x}{b})e^{iqz} \tag{3.62}$$

For cylindrical geometry,

$$\psi_{pqs}(r) = J_p(s\rho)e^{ip\phi}e^{-iqz} \tag{3.63}$$

For spherical geometry,

$$\psi_{pqs}(r) = z_n(s\rho)P_p^q(\cos\theta)e^{iq\phi} \tag{3.64}$$

The framework also provides an opportunity to study the effects of change in position of the source on the measured scattered field. This method also decreases the computation time as the dyadic Green's function is composed of well defined Bessel functions and their derivatives. Design and characterization of meta-surfaces is also refined by the use of this method. Since any surface when fabricated is not truly two dimensional then the simulations should also be carried out with the added condition where one dimension is considerably smaller than other two dimensions. It can also be modified to be used for chiral and bianisotropic media by changing the scalar spatially varying permittivity and permeability to its tensor spatially varying form in equation 3.41. The details of applications of this method to various geometry, design and characterization of metamaterial properties will be covered in subsequent chapters.

CHAPTER 4: META ELECTRODYNAMICS

So far, we have investigated the influence of geometry and surrounding medium on propagation of electromagnetic waves through core-shell geometry where the fields are related to each other using boundary conditions. The electromagnetic fields or potentials inside the shells are usually neither studied in detail nor to my knowledge any attempt has been made to engineer the distribution in the volume of the shell. In this chapter, we have built a framework to study the following

- **Distribution**: Characterize and design the distribution of electromagnetic fields and potentials inside the volume of dielectric and conducting shell or solid structures.
- **Dynamics**: Interaction of localized current densities with incident electromagnetic fields and perturbation due to presence of adjacent densities.

Since the geometry of a single meta-atom governs the detailed boundary conditions, the analysis becomes extremely complex for the wide spectrum of shapes utilized to construct meta-structures. This raises the question of how do geometrical parameters such as curvature and thickness affect the distribution of current on the surface and in the volume of the meta-atoms or eigen-modes? Here, we use differential geometry to directly incorporate geometrical parameters into the existing formalism of electromagnetic interactions. This will provide a way to map structure to observed function and to ensure that the method being developed can be generalized. Experimental and theoretical results have demonstrated the importance of geometry in the study of scattering and the three key components of such interactions are the wavelength of the incident radiation, the geometry of structures and the material or constitutive parameters, all of has been embedded in the method. In this chapter, the theoretical framework will be developed from first principles as most approximations are invalid when structure sizes become comparable to wavelength. The basic understanding will help develop physical intuition regarding the impact of loss mechanisms, scattering from resonant and non-resonant meta-atoms, and also from 2D and 3D arrangements of such structures. The incident field induces a current density in the meta-atoms and thus the scattered field generated can be linked to the induced multipole moments providing a method to connect observed global effects to local interactions.

The dynamics of interaction of localized current densities in a unit structure with incident electromagnetic fields can be studied using semi-classical interaction Lagrangian and Hamiltonian. The effect of coupling between adjacent structures can be understood by the perturbation in the dynamics accounted by damping parameters and their effects on the observed far field. We have demonstrated the concept of coupling parameters that can relate the local multiple scattering between meta-atoms and their inter-element coupling effects to observable quantities but the rigorous mathematics is yet to be developed.

The major impact of this method is development of a bottom-up theoretical framework for analysis of interaction of light with meta-structures, which would be a major step away from the existing mesh-based computational and small-field perturbative models. This new characterization method relates the dynamics of current densities in meta-structures to the scattered field using multipole analysis of geometry based current distribution. The effects of change in geometry of structures on the induced current densities can be studied using differential geometry and group theory approaches. These methods inherently exploit the symmetry and lack thereof to predict the properties of structures and to classify them based on their response to the incident field. Development of this framework improves the understanding of interaction of various modes to achieve strong non-linearities for harmonic generation and can provide a basis for mathematical development of metamaterial-based lasers. These tools for detailed understanding and numerical verification of meta-structures will help to establish fundamental limits for scattering and losses, and will allow identification of optimal structures having maximum response to incident radiation.

The study of non-linear phenomenon is dominated by perturbative models, inherently restricting the magnitude of second- or higher-order effects. Interactions of various multipole modes can be studied in order to enhance the second- and higher-order effects along with the influence of epsilon-near-zero materials. One of the main goals of this proposal is to establish the mathematical framework for analyzing strong non-linear interactions using the multipole moments which can be manipulated by the induced current densities. The analysis of single meta-atoms as entities possessing various modes of radiation allows them to be treated as atoms which can be used to develop sources of laser radiation. Experimental verification of limits of losses from well-known structures has not been discussed in this dissertation but computational studies of bianisotropic structures for second-harmonic generation can be done using the method developed. Using the adaptable framework developed we can develop a table of meta-structures according to their properties and meta-surfaces for maximum response to radiation and hopefully can achieve the most ambitious goal of experimental demonstration of metamaterial lasers.

4.1 Distribution

In order to develop a complete understanding of light-structure interactions both the geometry of the scattering object and the nature of excitation have to be considered, especially when the structure size is comparable to wavelength of incident radiation [49]. In this section, we build a rigorous theoretical framework for analyzing the responses of a structured material by characterizing the interaction of electromagnetic waves with meta-atoms in terms of induced current densities and relating the eigen-modes of current distribution to the scattered field through its multipole moments. The effects of interactions between several adjacent meta-atoms in different arrangements on the current dynamics can be studied using principles of quantum electrodynamics and can be associated to observable far-field effects. In order to ensure generalizability of the method we can decompose the induced current densities into temporal and spatial components which be dependent on the geometry of the meta-atoms through differential geometry, hence mapping structure to function of scattered fields. The aforementioned steps combined with specific functional forms of material parameters will be used to determine the overall effective material parameters of each meta-structure and their changes due to the interactions with adjacent structures.

The distribution of current induced in metallic meta-structures depends on the skin depth and geometry of the structure which plays a crucial role in accurate determination of scattered field. The traditional theory of skin depth may not be sufficient to explain the interaction when the size of meta-atoms becomes comparable to the operating wavelength and the thickness of the structures becomes deeply sub-wavelength. The experiments conducted ([87], and chapter 2) have led to unexpected results in the scattered field from cylindrical shells when the interior contents are altered. These observations imply that the skin depth can be varied by engineering the surface geometry. If we are able to excite Fabry-Perot type resonances then the transmission can be increased as evident in Fabry-Perot cavities. This provides a new avenue for exploiting the effect of geometry in the distribution of current in conductors with finite conductivity. For ease of calculation, metals are typically assumed to have infinite conductivity but as we know from calculation of transmission in cavities a slight deviation from 100% reflectivity leads to a potentially large transmission. Hence, similar resonant effects can lead to modification of the skin depth in finite conductivity calculations allowing skin-depth engineering. Skin depth can also be modified in the dielectric structure [88] by designing structures using layers of different materials.

In this section, we will discuss the decomposition of current densities into multipole moments and accurate calculation of current distribution in three dimensional structures.

4.1.1 Multipolar Analysis

The diversity of meta-atom geometries and the spectrum of frequencies spanned by metamaterial applications makes the development of single analytical framework to characterize the interactions very difficult. However, this complex task can be simplified by dividing it into smaller problems. The analysis of a single meta-atom can be done using multipole theory which expresses observable quantities in terms origin dependent such electric and magnetic polarizabilities or multipole moments. Multipole expansions in electrostatics, magnetostatics and electrodynamics provide a useful and powerful method for characterizing charge and current densities, and the generated electromagnetic fields and potentials. Since, the multipole moments are generated by the induced current distributions in the individual meta-atoms this method provides an opportunity to engineer the current distribution in these structures. There have been efforts using multipole theory as way to characterize light-matter interactions but the current is usually considered to exist in a spherical volume which generates the multipole moments [89, 90]. There is a dearth of literature where the microstructure of the materials is analyzed precisely without any simplifying approximations. In order to study the accurate analysis of current distributions in metallic and dielectric structure we to understand how current distribution is related to multipole moments.

First, we will be look at the traditional multipole expansions presented in standard textbooks [38, 91] for electromagnetic potentials. In the case of a finite, continuous charge distribution with density ρ and the origin within the distribution (see figure 4.1a), the charge density infinitesimal volume dv at $\mathbf{r}'$ is ρdv. The electromagnetic potential at point P located at $\mathbf{r}$ is

$$\Phi(\mathbf{r}) = \frac{1}{4\pi\epsilon_0}\int_V \frac{\rho(\mathbf{r})dv}{|\mathbf{r}-\mathbf{r}'|} \tag{4.1}$$

If we assume that the zero of the potential is at zero then for a point $\mathbf{r} >> \mathbf{r}'$, we can expand the denominator

$$\begin{aligned}
|\mathbf{r}-\mathbf{r}'|^{-1} =&(r^2 - 2\mathbf{r}\cdot\mathbf{r}' + r'^2)^{-\frac{1}{2}}\\
=&\frac{1}{r}(1+\frac{1}{r^2}[r^2 - 2\mathbf{r}\cdot\mathbf{r}'])^{-\frac{1}{2}}\\
=&\frac{1}{r} + \frac{\mathbf{r}\cdot\mathbf{r}'}{r^3} + \frac{3(\mathbf{r}\cdot\mathbf{r}')^2 - r^2r'^2}{2r^5} + \frac{5(\mathbf{r}\cdot\mathbf{r}')^3 - 3r^2(\mathbf{r}\cdot\mathbf{r}')r'^2}{2r^7} + \cdots
\end{aligned} \tag{4.2}$$

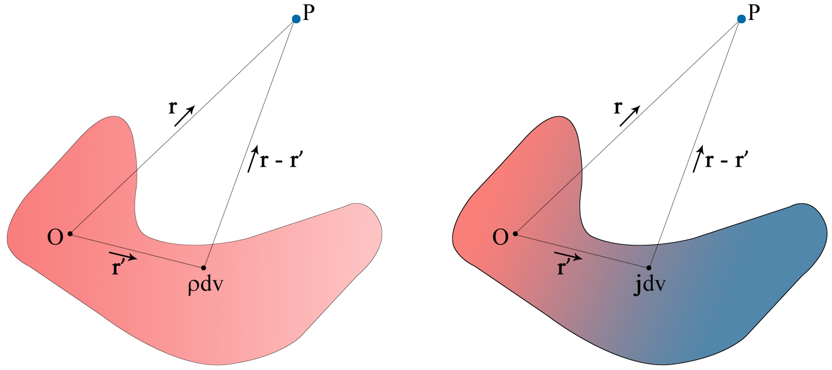

(a) Discrete charge distribution. (b) Current distribution.

Figure 4.1: Coordinates for finite and continuous charge and current distributions.

Hence, using equation 4.1 and 4.2, the multipole expansion of electrostatic potential is given by

$$\begin{aligned}
\Phi(\mathbf{r}) =&\frac{1}{4\pi\epsilon_0}[\frac{q}{r} + \frac{r_i}{r^3}p_i + \frac{3r_ir_j - r^2\delta_{ij}}{2r^5}q_{ij} +\\
&\frac{5r_ir_jr_k - r^2(r_i\delta_{jk} + r_j\delta_{ki} + r_k\delta_{ij})}{2r^7}q_{ijk} + \cdots]
\end{aligned} \tag{4.3}$$

Similar expression can be derived for discrete charge distribution with N charges q^i $(i = 1, 2, \cdots, N)$ each located at position $\mathbf{r}^i$

$$\Phi(\mathbf{r}) = \frac{1}{4\pi\epsilon_0}\sum_{i=1}^{N}\frac{q^i(\mathbf{r})dv}{|\mathbf{r}-\mathbf{r}^i|} \tag{4.4}$$

In the case of finite current distribution as shown in figure 4.1b, the vector potential at point P is given by

$$\mathbf{A}(\mathbf{r}) = \frac{\mu_0}{4\pi}\int_V \frac{\mathbf{j}(\mathbf{r})dv}{|\mathbf{r}-\mathbf{r}'|} \tag{4.5}$$

Thus, multipole expansion for magnetostatic $(\nabla\cdot\mathbf{j}(r)) = 0$ vector potential is given by,

$$\mathbf{A}(\mathbf{r}) = \frac{\mu_0}{4\pi}[\frac{1}{r}\int_V j_i dv + \frac{r_i}{r^3}\int_V j_i r_j dv + \frac{3r_i r_j - r^2\delta_{ij}}{2r^5}\int_V j_i r_j r_k dv + \cdots] \tag{4.6}$$

We are interested in the interaction of light interactions which is a dynamic system, hence we have to look a the multipole expansion of electromagnetic potentials. In Lorenz gauge, potentials are given by

$$\Phi(\mathbf{r}) = \frac{1}{4\pi\epsilon_0}\int_V \frac{\rho(\mathbf{r}, t - \frac{|\mathbf{r}-\mathbf{r}'|}{c})dv}{|\mathbf{r}-\mathbf{r}'|} \tag{4.7}$$

$$\mathbf{A}(\mathbf{r}) = \frac{\mu_0}{4\pi}\int_V \frac{\mathbf{j}(\mathbf{r}, t - \frac{|\mathbf{r}-\mathbf{r}'|}{c})dv}{|\mathbf{r}-\mathbf{r}'|} \tag{4.8}$$

Here, c is the speed of light in vacuum, V is volume of current and charge densities at retarded time $\mathbf{r}, t - \frac{|\mathbf{r}-\mathbf{r}'|}{c}$. For a field in the far field $(R >> r)$, retarded time can be written in terms of retarded time at the origin t',

$$t - \frac{|\mathbf{r}-\mathbf{r}'|}{c} = t - \frac{r}{c} + \Delta t = t' + \Delta t \tag{4.9}$$

where,

$$\Delta t = \frac{1}{c}[\frac{r_i}{r}r_i + \frac{r_ir_j - r^2\delta_{ij}}{r^3}r_ir_j + \frac{3r_ir_jr_k - r^2(r_i\delta_{jk} + r_j\delta_{ki} + r_k\delta_{ij})}{6r^5}r_ir_jr_k + \cdots] \tag{4.10}$$

Making a Taylor series expansion of $\rho(\mathbf{r}, t' + \Delta t)$ about t',

$$\rho(\mathbf{r}, t' + \Delta t) = \rho(\mathbf{r}, t') + \frac{\partial\rho(\mathbf{r}, t')}{\partial t'}\Delta t + \frac{1}{2!}\frac{\partial^2\rho(\mathbf{r}, t')}{\partial t'}^2\Delta t^2 + \frac{1}{3!}\frac{\partial^3\rho(\mathbf{r}, t')}{\partial t'}^3\Delta t^3 \cdots \tag{4.11}$$

Using equation 4.10, $\rho = \rho(\mathbf{r}, t')$ and $\dot{\rho} = \frac{\partial\rho(\mathbf{r},t')}{\partial t}$, we get

$$\begin{aligned}&\rho(\mathbf{r}, t' + \Delta t) = \rho + \dot{\rho}\frac{1}{c}\frac{r_i}{r}r_i + [\dot{\rho}\frac{r_ir_j - r^2\delta_{ij}}{2cr^3} + \ddot{\rho}\frac{r_ir_j}{2c^2r^2}]r_ir_j + \\ &[\frac{1}{6cr^5}(\dot{\rho} + \frac{R}{c}\ddot{\rho})[3r_ir_jr_k - r^2(r_i\delta_{jk} + r_j\delta_{ki} + r_k\delta_{ij})] + \dddot{\rho}\frac{r_ir_jr_k}{6c^3r^3}]r_ir_jr_k + \cdots\end{aligned} \tag{4.12}$$

The scalar potential in terms of electrical multipole moments is given by,

$$\begin{aligned}\Phi(\mathbf{r}, t) =& \frac{1}{4\pi\epsilon_0}[\frac{q}{r} + \frac{r_i}{r^3}(p_i + \frac{R}{c}\dot{p_i}) + \frac{3r_ir_j - r^2\delta_{ij}}{2r^5}(q_{ij} + \frac{R}{c}\dot{q_{ij}}) + \frac{r_ir_j}{2c^2r^3}\ddot{q_{ij}} \\ &+ \frac{5r_ir_jr_k - r^2(r_i\delta_{jk} + r_j\delta_{ki} + r_k\delta_{ij})}{2r^7}(q_{ijk} + \frac{R}{c}\dot{q_{ijk}}) \\ &+ \frac{6r_ir_jr_k - r^2(r_i\delta_{jk} + r_j\delta_{ki} + r_k\delta_{ij})}{6c^2r^5}\dddot{q_{ijk}} + \frac{r_ir_jr_k}{6c^3r^4}\dddot{q_{ijk}} + \cdots]\end{aligned} \tag{4.13}$$

Similarly, for electromagnetic vector potential can be written in terms of electric and magnetic multipole moments,

$$\begin{aligned}\mathbf{A}_i(\mathbf{r}, t) =& \frac{1}{4\pi\epsilon_0}[\frac{\dot{p_i}}{r} + \frac{r_i}{r^3}[(\frac{1}{2}\ddot{q_{ij}} - \epsilon_{ijk}m_k) + \frac{r}{c}(\frac{1}{2}\ddot{q_{ij}} - \epsilon_{ijk}\dot{m_k})] \\ &+ \frac{3r_ir_j - r^2\delta_{ij}}{2r^5}[\frac{\dot{p_i}}{r} + \frac{r_i}{r^3}[(\frac{1}{2}\ddot{q_{ij}} - \epsilon_{ijl}m_{lk}) + \frac{r}{c}(\frac{1}{3}\ddot{q_{ijk}} - \epsilon_{ijl}\dot{m}_{lk})] \\ &+ \frac{r_jr_k}{2c^2r^3}(\frac{1}{3}\dddot{q_{ijk}} - \epsilon_{ijl}\dot{m}_{lk}) + \cdots]\end{aligned} \tag{4.14}$$

The multipole moments are located at an arbitrary origin in the current distribution and the retarded time is at the origin. The main reason to reproduce standard results is to illustrate the presence of individual electric and magnetic moments in the expansions for scalar and vector potentials. It should also be noted that the vector potential contains both electric and magnetic moments and in order to retain the magnetic quadrupole it is required to retain electric octopole.

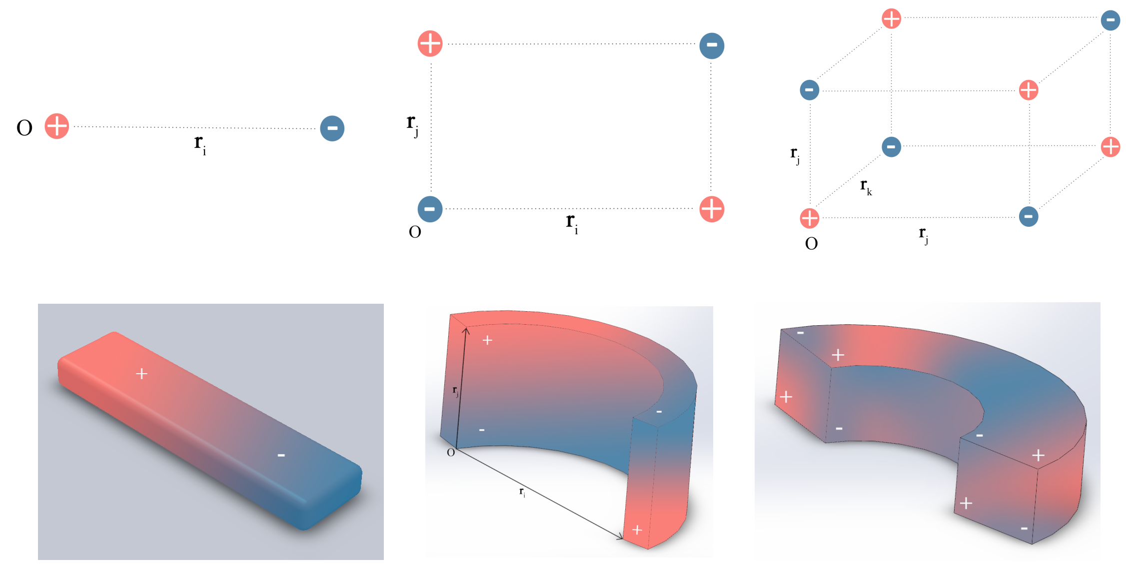

Figure 4.2: Top: Distribution of discrete charge particles leading to dipole, quadrupole, octupole moments. Bottom: Illustration of modes of current distributions or eigen-modes in meta-atoms for multipole moments.

Current and charge distribution in the volume of object is very important as it can be seen from the table below.

Table 4.1: Charge and current dependence of multipole Moments.

Moments	Electric	Magnetic
Monopole	$q = \int_V \rho(\mathbf{r})dv$	Does not exist
Dipole	$p_i = \int_V r_i \rho(\mathbf{r})dv$	$\dot{p_i} = \int_V \mathbf{j}(\mathbf{r})dv$
Quadrupole	$q_{ij} = \int_V r_i r_j \rho(\mathbf{r})dv$	$\frac{1}{2}\dot{q_{ij}}(t) - \epsilon_{ijk}m_k(t) = \int_V \mathbf{j}_i(\mathbf{r},t)r_j dv$
Octopole	$q_{ijk} = \int_V r_i r_j r_k \rho(\mathbf{r})dv$	$\frac{1}{3}\dot{q_{ijk}}(t) - \frac{1}{2}\epsilon_{ijl}m_{lk}(t) - \frac{1}{2}\epsilon_{ikl}m_{lj}(t) = \int_V \mathbf{j}_i(\mathbf{r},t)r_j r_k dv$

where, $\epsilon_{ijl}\epsilon_{klm} = \delta_{il}\delta_{jm} - \delta_{im}\delta_{jl}$. The exact calculation for higher order multipoles have been calculated rigorosly in Ref. [92] and can be adapted for calculation of multipoles of meta-atoms. It is also imperative to realize that multipole method is also valid for macroscopic medium. Since, Maxwells' equations are valid over any geometrical scale, then for microscopic equations where electric ($\mathbf{E}^m(\mathbf{r},t)$) and magnetic ($\mathbf{H}^m(\mathbf{r},t)$) vector fields generated by microscopic charge ($\rho^m(\mathbf{r},t)$) and current ($j^m(\mathbf{r},t)$) densities is given by,

$$\nabla \cdot \mathbf{E}^m(\mathbf{r},t) = \frac{1}{\epsilon_0}\rho^m(\mathbf{r},t) \tag{4.15}$$

$$\nabla \cdot \mathbf{H}^m(\mathbf{r},t) = 0 \tag{4.16}$$

$$\nabla \times \mathbf{E}^m(\mathbf{r},t) = -\mu_0 \frac{\partial}{\partial t}\mathbf{H}^m(\mathbf{r},t) \tag{4.17}$$

$$\nabla \times \mathbf{H}^m(\mathbf{r},t) = \mathbf{j}^m(\mathbf{r},t) + \epsilon_0 \frac{\partial}{\partial t}\mathbf{E}^m(\mathbf{r},t) \tag{4.18}$$

Averaging the microscopic fields and source densities using methods outlined in

[38, 93, 94] the bound charge and current densities become evident

$$\nabla \cdot \mathbf{E}(\mathbf{r}, t) = \frac{1}{\epsilon_0}(\rho_f(\mathbf{r}, t) + \rho_b(\mathbf{r}, t)) \tag{4.19}$$

$$\nabla \cdot \mathbf{H}(\mathbf{r}, t) = 0 \tag{4.20}$$

$$\nabla \times \mathbf{E}(\mathbf{r}, t) = -\mu_0 \frac{\partial}{\partial t}\mathbf{H}(\mathbf{r}, t) \tag{4.21}$$

$$\nabla \times \mathbf{H}(\mathbf{r}, t) = \mathbf{j}_f(\mathbf{r}, t) + \mathbf{j}_b(\mathbf{r}, t) + \epsilon_0 \frac{\partial}{\partial t}\mathbf{E}(\mathbf{r}, t) \tag{4.22}$$

The bound charge and current densities can expanded in macroscopic multipole moments from equations 4.7 and 4.8

$$\rho_b(\mathbf{r}, t) = -\nabla_i P_i + \frac{1}{2}\nabla_i \nabla_j Q_{ij} - \frac{1}{6}\nabla_k \nabla_j \nabla_i Q_{ijk} + \cdots \tag{4.23}$$

$$\mathbf{j}_{bi}(\mathbf{r}, t) = \dot{P}_i - \nabla_j(\frac{1}{2}\dot{Q}_{ij} - \epsilon_{ijk}M_k) + \nabla_j(\frac{1}{6}\dot{Q}_{ijk} - \frac{1}{2}\epsilon_{ijk}M_{lj}) + \cdots \tag{4.24}$$

Thus, macroscopic fields for each component in electric octopole -magnetic quadrupole becomes

$$D_i(\mathbf{r}, t) = \epsilon_0 E_i + P_i - \frac{1}{2}\nabla_j Q_{ij} + \frac{1}{6}\nabla_k \nabla_j Q_{ijk} + \cdots \tag{4.25}$$

$$B_i(\mathbf{r}, t) = \mu_0 H_i - \mu_0 M_i + \mu_0 \frac{1}{2}\nabla_j M_{ij} + \cdots \tag{4.26}$$

Multipole moments have been used to analyze interaction of light with structures in large variety of scenarios from study of molecules in chemistry [95], astrophysics [96] and widely in metamaterials [97, 98, 99, 100]. The multipole approach helps create a relationship between observed macroscopic response to microscopic interactions within meta-atoms. It helps relate the magnetization induced in meta-atoms to magnetic multipole moments and deduce the physical implications of the magnetic interactions on the overall response. This method can be used to derived the geometrical dependence of polarization and magnetization densities as shown later in the chapter and hence geometrical dependence of constitutive parameters. This allows design of meta-atoms from very basic principles and which can be extended to a wide variety of meta-atoms such as, plasmonic, active, passive and quantum metamaterials.

The multipole method can be adapted for analysis of meta-structures, where each meta-atom can be approximated as point current distribution and using multipole expansions for spherical geometry [38]. In general, the total field generated by total current distributions can be represented by superposition of point current densities. It has already been shown that superposition of dipole and torodial moments to generate non radiating anapole moment [35].

$$\begin{aligned}\mathbf{E}_s(r,\theta,\phi) = E_0\sum_{l=1}^{\infty}\sum_{m=-l}^{l} i^l[\pi(2l+1)]^{\frac{1}{2}}[\frac{1}{k}a_E(l,m)\nabla\times(h_l^{(1)}(kr)\mathbf{X}_{lm}(\theta,\phi))\\ +a_M(l,m)h_l^{(1)}(kr)\mathbf{X}_{lm}(\theta,\phi))]\end{aligned} \tag{4.27}$$

$$\begin{aligned}\mathbf{H}_s(r,\theta,\phi) = \frac{E_0}{\eta}\sum_{l=1}^{\infty}\sum_{m=-l}^{l} i^{l-1}[\pi(2l+1)]^{\frac{1}{2}}[\frac{1}{k}a_M(l,m)\nabla\times(h_l^{(1)}(kr)\mathbf{X}_{lm}(\theta,\phi))\\ +a_E(l,m)h_l^{(1)}(kr)\mathbf{X}_{lm}(\theta,\phi))]\end{aligned} \tag{4.28}$$

where, η is the impedance, $h_l^{(1)}(x)$ is the spherical Hankel function of the first kind and $\mathbf{X}_{lm}(x)$ is the normalized vector spherical harmonics. The wavenumber k is calculated for the surrounding medium which has the impedance η. As shown in

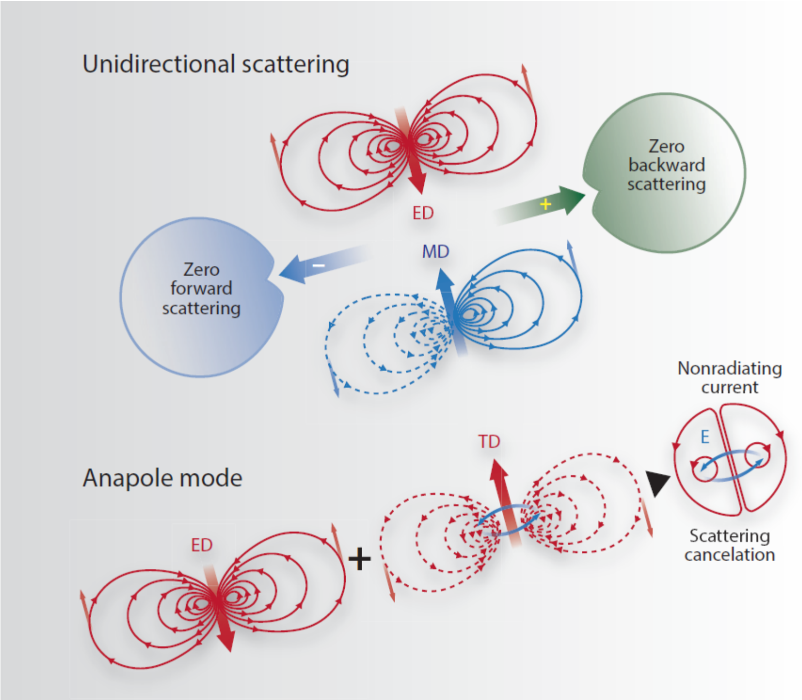

Figure 4.3: Ref. [90]: Constructive interference electric and magnetic dipole lead to zero back-scattering and destructive interference leads to zero forward scattering. Later cancellation of radiation pattern leads to a non radiative anapoles.

chapter 3, the vector wavefunctions form a complete basis to describe a scattering problem. They also help describe the scattering and extinction cross sections in a compact form. The scattering cross-section (σ_s) describes the amount of power scattered by the scattering object with respect to power per unit are carried by the incident wave. The extinction cross section (σ_e) describes the amount of overall power extracted by the scattering object with respect to power per unit area carried by the incident waves. The absorption cross-section (σ_a) describes the power absorbed by the scattering object with respect to power per unit area carried by the incident waves. The expression of the cross-sections is given by [101, 32],

$$\sigma_s = \frac{\pi}{k^2} \sum_{l=1}^{\infty} \sum_{m=-l}^{l} (2l+1)[|a_E(l,m)|^2 + |a_M(l,m)|^2] \tag{4.29}$$

The extinction cross section depends on the choice of polarization and propagation direction of the incident field, for a x-polarized wave traveling z extinction cross-section is given by

$$\sigma_{e,x} = -\frac{\pi}{k^2}\sum_{l=1}^{\infty}\sum_{m=-l,+1}(2l+1)\Re[ma_E(l,m)+a_M(l,m)] \tag{4.30}$$

For y-polarized wave

$$\sigma_{e,x} = -\frac{\pi}{k^2}\sum_{l=1}^{\infty}\sum_{m=-l,+1}(2l+1)\Im[a_E(l,m)+ma_M(l,m)] \tag{4.31}$$

where, $\Re(\cdot)$ and $\Im(\cdot)$ represent the real and imaginary parts. It should be noted that the summation for m is carried over just two values. The absorption coefficient is given by

$$\sigma_e = \sigma_a - \sigma_s \tag{4.32}$$

The calculation of the coefficients for scattered field over any spherical volume in terms of scalar spherical harmonics ($Y_{lm}(\theta,\phi)$) is given by

$$a_E(l,m) = \frac{(-i)^{l+1}kr}{h_l^{(1)}(kr)E_0[\pi(2l+1)l(l+1)]^{\frac{1}{2}}}\int_0^{2\pi}\int_0^{\pi}Y_{lm}^*(\theta,\phi)\hat{\mathbf{r}}\cdot\mathbf{E}_s(\mathbf{r})\sin\theta d\theta d\phi \tag{4.33}$$

$$a_M(l,m) = \frac{(-i)^{l+1}\eta kr}{h_l^{(1)}(kr)E_0[\pi(2l+1)l(l+1)]^{\frac{1}{2}}}\int_0^{2\pi}\int_0^{\pi}Y_{lm}^*(\theta,\phi)\hat{\mathbf{r}}\cdot\mathbf{H}_s(\mathbf{r})\sin\theta d\theta d\phi \tag{4.34}$$

Using the Maxwell's equations and multipole representation of charge and current densities (equations 4.23 & 4.24) provides a way to control the exact scattering from meta-structures. The main question is that can the current density be manipulated using geometry and what is the exact distribution of current inside the volume. In the next section, we will derive the geometrical dependence of current distribution.

4.1.2 Skin Depth Engineering

As we saw earlier that the analysis of electromagnetic waves inside a conducting volume is missing the component geometrical parameters. These formalism work well in large cases but there may situations where these calculations may breaks down or in the case of meta-structure design it may be desired to engineer the current distribution. The accurate calculation of current distribution in a volume element requires the exact representation of the surface. It is apparent that the calculation becomes increasingly complex even for relatively simple geometries such as a ring. In order to develop a closed-form solution for a more complex geometry we have use the generalized coordinate system from differential geometry and develop a formalism for electromagnetism in curved spaces fulfilling the need for a mathematical framework for calculation of current distributions and scattered fields in meta-atoms of arbitrary geometry. In this section we will follow the notations of Ref. [102] for differential geometry properties which describes any geometric configuration (curves, surfaces and volumes) using differential and integral calculus.

4.1.3 Theory of Curves

In order to develop the mathematical framework in generalized coordinates we introduce a set of local coordinates at the surface S. One of the key aspects of generalized coordinate system is the parameterization of space.

- Three dimensional *position vector* $\mathbf{x}$, where x_1, x_2, x_3 are coordinates.

$$\mathbf{x} = (x_1, x_2, x_3) \tag{4.35}$$

- The *parametric representation* of the position vector is given as

$$\mathbf{x} = (x_1(s), x_2(s), x_3(s)) \tag{4.36}$$

where, t is real variable defined in the interval $I : a \leq t \leq b$. This means that for every value of t there is a point in three dimensional space that has position vector $\mathbf{x}(t)$.

An arbitrary three dimensional curve C can be parameterized using the arc length s as the parameter $\mathbf{x}(s)$. Two points on the curve separated by h determine a chord between s and $s + h$ with direction of the tangent vector $\mathbf{x}(s + h) - \mathbf{x}(s)$, thus the unit tangent vector at point $\mathbf{x}(s)$,

$$\mathbf{t}(s) = \lim_{h \to 0} \frac{\mathbf{x}(s + h) - \mathbf{x}(s)}{h} = \frac{d\mathbf{x}}{ds} \tag{4.37}$$

- A straight line passing through a point P in the direction of the unit tangent vector (see figure 4.4a) through a point on curve is called a *tangent*.
- The totality of all vectors bound at a point of the curve which are normal to unit tangent vector is called *normal plane*.

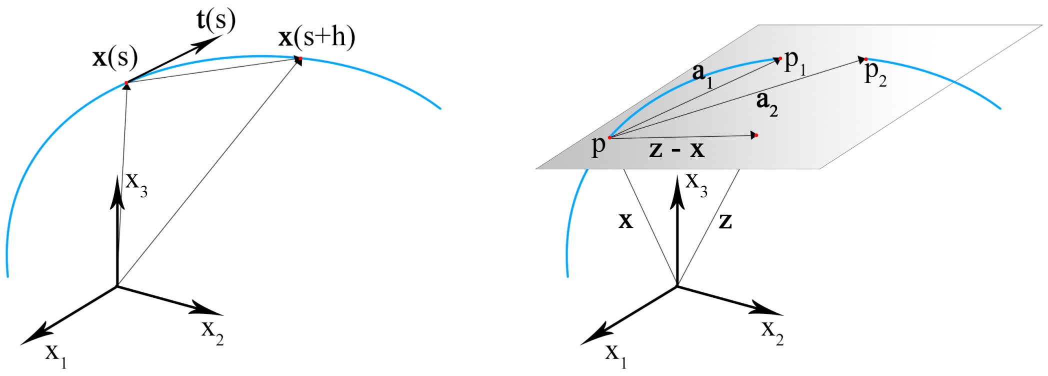

(a) Tangent vector and Normal plane (b) Osculating plane.

Figure 4.4: Parameterization of a curve.

In figure 4.4b, we have two points p and p_1 on the curve C joined by a straight line. If the point p_1 tends towards p, then in the limiting case line joining them becomes a tangent. Hence, we want to determine the limiting position of plane through the points p, p_1 and p_2 as both points tend towards p. The parametric values of points s, $s+h_1$, $s+h_2$, respectively gives a chord vectors pp_1 and pp_2 which span the entire plane in the event of linearly independent.

$$\mathbf{a}_i = \mathbf{x}(s+h_i) - \mathbf{x}(t) \tag{4.38}$$

The plane is also spanned by

$$\mathbf{v}^1 = \frac{\mathbf{a}_1}{h_1} \quad \& \quad \mathbf{w} = \frac{2(\mathbf{v}^2 - \mathbf{v}^1)}{h_2 - h_1} \tag{4.39}$$

Using Taylor formula

$$\mathbf{x}(s+h_i) = \mathbf{x}(s) + h_i\mathbf{x}'(s) + \frac{h_i}{2!}\mathbf{x}''(s) + \mathbf{o}(h_i^2) \tag{4.40}$$

If $f(z)$ and $g(z)$ are non zero functions the interval with $z = 0$ such that quotient $g(z)/f(z)$ tends to zero as z tends to zero then $g(z)$ is said to be $\mathbf{o}(f(z))$. Hence if $\mathbf{o}(h_1) + \mathbf{o}(h_2) = \mathbf{o}(h_2 - h_1)$, we get

$$\mathbf{v}^1 = \mathbf{x}'(s) + \frac{h_1}{2!}\mathbf{x}''(s) + \mathbf{o}(h_1) \tag{4.41}$$

$$\mathbf{w} = \mathbf{x}''(s) + \mathbf{o}(1) \tag{4.42}$$

- If $h_i \to 0$, then $\mathbf{v}^1 \to \mathbf{x}'(s)$ and $\mathbf{w} \to \mathbf{x}'',(s)$. And if $\mathbf{x}'(s)$ and $\mathbf{x}''(s)$ are linearly independent then they span the plane namely, *osculating plane*. Thus, osculating plane at point P on curve C with $\mathbf{z}$ is the position vector of a point on it is given by

$$|(\mathbf{z} - \mathbf{x})\mathbf{x}'\mathbf{x}''| = 0 \tag{4.43}$$

- When the osculating plane passes through the tangent, the intersection of osculating and normal plane is called *principle normal.*

Parameterization of surfaces require calculation of some basic tensor quantities. For a curve on surface $S : \mathbf{x}(u^1, u^2)$ can be represented by a parameteric representation

$$u^1 = u^1(t) \qquad u^2 = u^2(t) \tag{4.44}$$

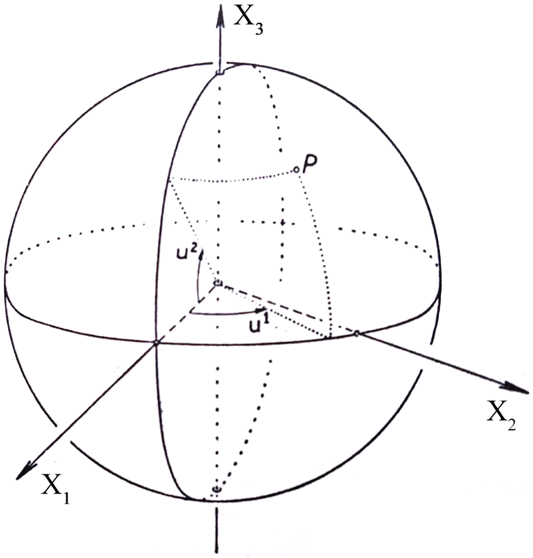

Figure 4.5: Point P in three dimensional space.

In order to determine the element of arc (or linear element) of the curve which leads to first fundamental form.

$$ds^2 = \sum_{i=1}^{3} dx_i^2 = d\mathbf{x} \cdot d\mathbf{x} = (\mathbf{x}_1 du^1 + \mathbf{x}_2 du^2) \cdot (\mathbf{x}_1 du^1 + \mathbf{x}_2 du^2) \tag{4.45}$$

$$ds^2 = \mathbf{x}_1 \cdot \mathbf{x}_1 (du^1)^2 + 2\mathbf{x}_1 \cdot \mathbf{x}_2 du^1 du^2 + \mathbf{x}_2 \cdot \mathbf{x}_2 (du^2)^2 \tag{4.46}$$

- Using the $\mathbf{x}_\alpha \cdot \mathbf{x}_\beta = g_{\alpha\beta}$ are components of metric tensor tensor or fundamental tensor.

- Note superscript represents contravariant behavior and subscript represents covariant tensor.

$$ds^2 = \sum_{\alpha=1}^{2} \sum_{\beta=1}^{2} g_{\alpha\beta} du^\alpha du^\beta \tag{4.47}$$

- Without any detailed calculations, the second fundamental form is defined as

$$b_{\alpha\beta} = \mathbf{x}_{\alpha\beta} \cdot \mathbf{n} \qquad \mathbf{x}_{\alpha\beta} = \frac{\partial^2 \mathbf{x}}{\partial u^\alpha \partial u^\beta} \tag{4.48}$$

The second fundamental form is invariant with respect to any allowable coordinate transformation which preserves the sense of the normal **n** evident by

$$b_{\alpha\beta} du^\alpha du^\beta = -d\mathbf{x} \cdot d\mathbf{n} \tag{4.49}$$

In order to parameterize the arbitrary and normal sections of a surface, we need to introduce normal curvature

$$\kappa_n = \frac{b_{\alpha\beta} du^\alpha du^\beta}{g_{\alpha\beta} du^\alpha du^\beta} \tag{4.50}$$

Thus, using the principal curvatures are the curves intersection of principal planes with the surface which gives two main curvatures for the analysis of surfaces.

- Gaussian curvature of the surface at the point of curvature

$$K = \kappa_1 \kappa_2 = \frac{b}{g} \tag{4.51}$$

- For a sphere of radius r has Gaussian curvature $\frac{1}{r^2}$ everywhere, and a flat plane and a cylinder have Gaussian curvature is zero.
- The arithmetic mean of the principle curvature is called mean curvature

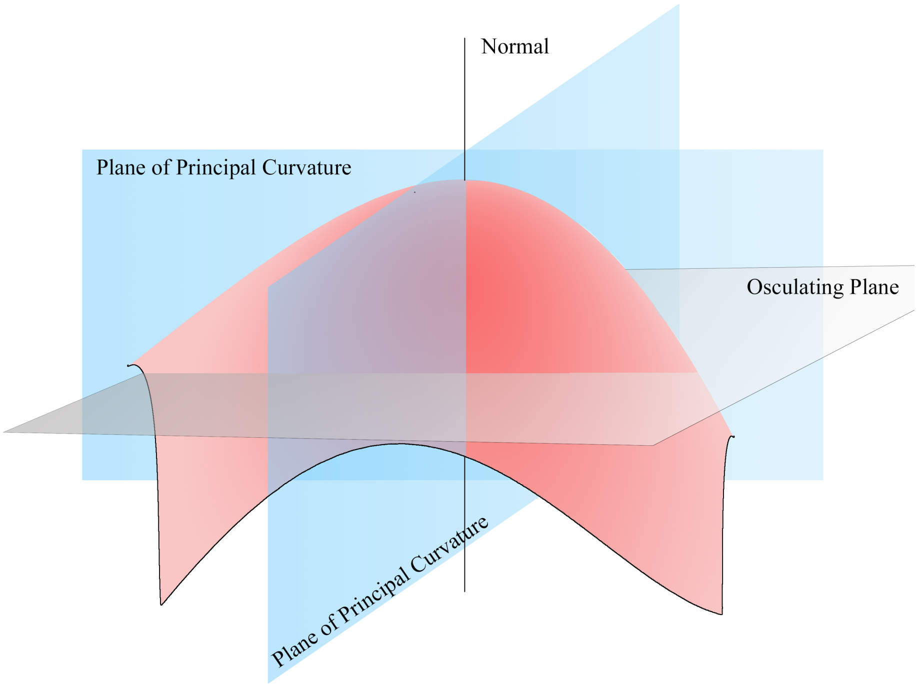

Figure 4.6: Principal plane and principal curvatures.

$$H = \frac{1}{2}(\kappa_1 + \kappa_2) = \frac{1}{2} b_{\alpha\beta} g^{\alpha\beta} = \frac{1}{2} b^{\alpha}_{\alpha} \tag{4.52}$$

- It is related to the normal vector by

$$H = -\frac{1}{2} \nabla \cdot \mathbf{n} \tag{4.53}$$

4.1.4 Asymptotic Skin Depth Formulation

In order to explain the method used in this section to derive geometrical dependence of skin depth, first we illustrate the use of asymptotic methods to derive common geometrical optics formulations, such as Fermat's principle and intensity law using the formulation used in Ref. [51].

In figure 4.7a a plane wave traveling positive z - direction shown which can be written as

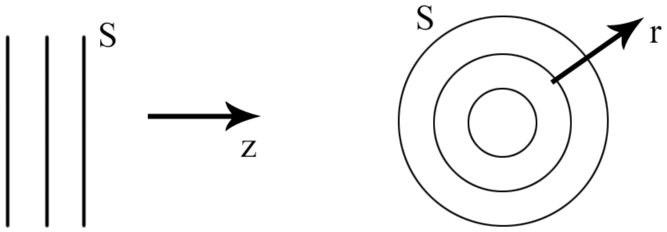

(a) A plane wave. (b) A spherical wave.

Figure 4.7: Illustration of wavefronts and ray directions.

$$U(\mathbf{r}) = U_0 e^{ikz} \tag{4.54}$$

where, U_0 is the amplitude of the incident field and the geometric waves are straight lines propagating in z - direction and wavefronts can be written as $z = constant$. A spherical wave generated by a point source at origin is illustrated in figure 4.7b which can be written as,

$$U(\mathbf{r}) = U_0 \frac{e^{ikr}}{kr} \tag{4.55}$$

where, the optical path is simply a straight line originating from the origin. A more general field can be written in the form which is not valid in every case but can be used to define a ray with well defined direction at any given point.

$$U(\mathbf{r}) = a(\mathbf{r}) e^{ikS(\mathbf{r})} \tag{4.56}$$

Substituting this trail solution in Helmholtz equation, we have

$$\nabla \cdot \nabla [a(\mathbf{r}) e^{ikS(\mathbf{r})}] + k^2 n^2(\mathbf{r}) a(\mathbf{r}) e^{ikS(\mathbf{r})} = 0 \tag{4.57}$$

Using chain rule the differential equation can be expanded as and dividing the common exponential term,

$$\nabla^2 a + 2ik\nabla a \cdot \nabla S - k^2 a(\nabla S)^2 + ika\nabla^2 S + k^2 n^2 a = 0 \tag{4.58}$$

As both a and S are both real valued functions, the real part of the equation becomes

$$\nabla^2 a - k^2 a(\nabla S)^2 + k^2 n^2 a = 0 \tag{4.59}$$

After dividing by $k^2 a$ and take the geometrical optics limit of $\lambda \to 0$ and $k \to \infty$, we get

$$(\nabla S)^2 = n^2 \tag{4.60}$$

This is the Eikonal equation of geometrical optics which is the differential form of Fermat's principle. The expression 4.56 is the simplest form but a more sophisticated model for geometric wave can be written as

$$U(\mathbf{r}) = \sum_{n=0}^{\infty} \frac{a_n(\mathbf{r})}{(ik)^n} e^{ikS(\mathbf{r})} \tag{4.61}$$

Substituting in Helmholtz equation

$$[\nabla^2 + k^2 n^2(\mathbf{r})] \sum_{n=0}^{\infty} \frac{a_n(\mathbf{r})}{(ik)^n} e^{ikS(\mathbf{r})} = 0 \tag{4.62}$$

Using chain rule we can write

$$\sum_{n=0}^{\infty} \frac{1}{(ik)^n} [\nabla^2 a_n + 2ik\nabla a_n \cdot \nabla S - k^2 a_n(\nabla S)^2 + ika_n\nabla^2 S + k^2 n^2 a_n] = 0 \tag{4.63}$$

The lowest order term $n = 0$,

$$-k_0^a(\nabla S)^2 + k^2 n^2 a_0 = 0 \tag{4.64}$$

which is the Eikonal equation. The next order term $n = 1$ gives,

$$2ik\nabla a_0 \cdot \nabla S + ika_0 \nabla^2 S - a_1(\nabla S)^2 + n^2 a_1 = 0 \tag{4.65}$$

The last two terms vanish because of Eikonal equation and the rest gives the intensity law of geometrical optics [51]. The case discussed here is for a scalar but similar expression can be derived for electric and magnetic field vectors in Ref. [48], which is given as

$$\mathbf{E}_0 = \sum_{n\geq 0} \frac{\mathbf{e}_n(\mathbf{r})}{(ik_0)^n} e^{ikS(\mathbf{r})} \qquad \mathbf{H}_0 = \sum_{n\geq 0} \frac{\mathbf{h}_n(\mathbf{r})}{(ik_0)^n} e^{ikS(\mathbf{r})} \tag{4.66}$$

Separating the spatial parts of the field vector in terms of a small parameters provide an elegant way to obtain an asymptotic expression of light-meta structure interactions. Now, we use these concepts to study conducting structure of arbitrary geometry and surrounded by dielectric material interacting with an electromagnetic wave with harmonic time dependence with angular frequency, ω.

- Dielectric region: $\epsilon = \epsilon_0$, $\sigma = 0$ and $\mu = \mu_0$
- Conducting region: $\epsilon = \epsilon_r\epsilon_0$, $\epsilon_r = (1 + \frac{i\sigma(\omega)}{\epsilon_0\omega}) = (1 + \frac{i}{\Delta^2})$, $\sigma(\omega) = \sigma$ and $\mu = \mu_0$

Hence, Maxwell's equations in space-frequency domain in both regions

For Dielectric,

$$\begin{aligned} \nabla \times \nabla \times \mathbf{E} - \omega^2\epsilon_0\mu_0\mathbf{E} &= i\omega\mu_0\mathbf{j} \\ \nabla \times \nabla \times \mathbf{H} - \omega^2\epsilon_0\mu_0\mathbf{H} &= \nabla \times \mathbf{j} \end{aligned} \tag{4.67}$$

For Conducting region

$$\begin{aligned} \nabla \times \nabla \times \mathbf{E} - (1 + \frac{i}{\Delta^2})\omega^2 \epsilon_0 \mu_0 \mathbf{E} = 0 \\ \nabla \times \nabla \times \mathbf{H} - (1 + \frac{i}{\Delta^2})\omega^2 \epsilon_0 \mu_0 \mathbf{H} = 0 \end{aligned} \tag{4.68}$$

Now, with all the basic quantities defined we can start analyzing the geometric dependence of skin effect. We first split the parameterization of position vector using the formalism developed in quantum mechanics of constrained particles [103] using the unit normal **n** as shown in figure 4.8. The local coordinate system can be decomposed in normal and tangential components as

$$\mathbf{x}(x_1, x_2, x_3) = \mathbf{o}(x_1, x_2) + \delta x_3 \mathbf{n}(x_1, x_2) \tag{4.69}$$

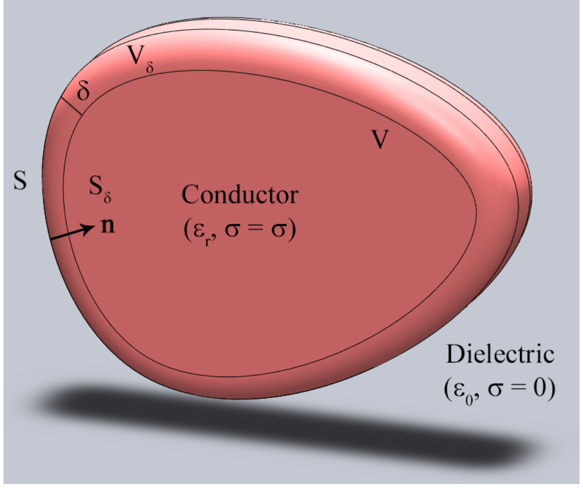

Figure 4.8: Illustration of arbitrary geometry of a conducting volume V represented by red. Surrounding dielectric with $\sigma = 0$, represented by gray. The black lines represents volume V_δ of current inside the conductor with thickness δ. Surface of the conductor S is the interface between conductor and dielectric and S_δ is the surface of the penetrated fields.

We want to develop a metric tensor that can split any vector field **F** into normal F_n and tangential F_T components which is a vector field $\mathbf{F}^\alpha$, where $\alpha = 1, 2$ on the surface S_δ inside the conducting object at a distance δ for the interface. The metric tensor

$$\begin{gathered} g_{\alpha\beta}(x^3) = f_{\alpha\beta} - 2b_{\alpha\beta}x^3 + b^{\eta}_{\alpha}b_{\eta\beta}(x^3)^2 \\ g_{33} = 1, \qquad g_{3\alpha} = 0 \end{gathered} \tag{4.70}$$

$$g_{\alpha\beta}(x^3) = \begin{bmatrix} g_{\alpha\beta}(x^3) & 0 \\ 0 & 1 \end{bmatrix} \tag{4.71}$$

In order to calculate the operators for Maxwell's equations we need the determinant of the metric tensor which is given by in terms of Jacobian expressed as a function of Gaussian and mean curvature (H and K)

$$\sqrt{g} = \sqrt{f}(1 - 2Hx^3 + K(x^3)^2) \tag{4.72}$$

The calculation of exact solution for the decaying fields is still difficult to find, hence using the formalism developed for study of scattering and general boundary conditions [104] we want to calculate the series for skin depth. Henceforth, we will be using the position vectors in local coordinate system, $\mathbf{x} = (x_T, x_n) = (x_\alpha, x_3)$. Using the series expansion of fields using the proof provided in section 4 of Ref. [104], for dielectric region

$$\begin{aligned} \mathbf{E}^d_\Delta(\mathbf{x}) &= \sum_{j\geq 0} \Delta^j E^d_j(\mathbf{x}) = E^d_0(\mathbf{x}) + \Delta E^d_1(\mathbf{x}) + \Delta^2 E^d_2(\mathbf{x}) + \cdots \\ \mathbf{H}^d_\Delta(\mathbf{x}) &= \sum_{j\geq 0} \Delta^j H^d_j(\mathbf{x}) = H^d_0(\mathbf{x}) + \Delta H^d_1(\mathbf{x}) + \Delta^2 H^d_2(\mathbf{x}) + \cdots \end{aligned} \tag{4.73}$$

In conductor region,

$$\begin{aligned}\mathbf{E}^c_\Delta(\mathbf{x},\Delta) &= \sum_{j\geq 0}\Delta^j E^c_j(\mathbf{x},\Delta) = E^c_0(\mathbf{x},\Delta) + \Delta E^c_1(\mathbf{x},\Delta) + \Delta^2 E^c_2(\mathbf{x},\Delta) + \cdots \\ \mathbf{H}^c_\Delta(\mathbf{x},\Delta) &= \sum_{j\geq 0}\Delta^j H^c_j(\mathbf{x},\Delta) = H^c_0(\mathbf{x},\Delta) + \Delta H^c_1(\mathbf{x},\Delta) + \Delta^2 H^c_2(\mathbf{x},\Delta) + \cdots\end{aligned} \tag{4.74}$$

where, the functions in the conductor is calculated at Δ from the surface in the normal direction and $\Xi(x_3)$ is a smooth function on the surface and equal to 1 outside the conductor region. *Physically*, it means that the field at a scaled distance inside the conductor can be separated into tangential and decaying normal component.

$$\begin{aligned}E^c_j(\mathbf{x},\Delta) &= \Xi(x_3)\mathbf{e}(x_a,\frac{x_3}{\Delta}) \\ H^c_j(\mathbf{x},\Delta) &= \Xi(x_3)\mathbf{h}(x_a,\frac{x_3}{\Delta})\end{aligned} \tag{4.75}$$

In the case of very high conductivity the field penetration will be very small, hence we need to add the condition $\mathbf{e}(x_a,x_3) \rightarrow 0$ and $\mathbf{h}(x_a,x_3) \rightarrow 0$ when $\frac{x_3}{\Delta} \rightarrow 0$. Now using the wave equation for magnetic field with source located in dielectric region.

Thus, to be precise the expression should be

$$\begin{aligned}E^c_j(\mathbf{x},\Delta) &= \Xi(x_3)\mathbf{e}(x_a,\frac{x_3}{\Delta}) + O(\Delta\rightarrow\infty) \\ H^c_j(\mathbf{x},\Delta) &= \Xi(x_3)\mathbf{h}(x_a,\frac{x_3}{\Delta}) + O(\Delta\rightarrow\infty)\end{aligned} \tag{4.76}$$

but the term $O(\Delta\rightarrow\infty)$ is understood and not explicitly written in the calculations. The convergence of series has also been proved in [104] along with error analysis, hence it has not been reproduced here.

Substituting the asymptotic representation in equations 4.67 and 4.68, we get

$$[\nabla \times \nabla \times \cdot - \omega^2\epsilon_0\mu_0] \sum_{j\geq 0} \Delta^j E_j^d(\mathbf{x}, \Delta) = i\omega\mu_0\mathbf{j} \tag{4.77}$$

$$[\nabla \times \nabla \times \cdot - (1 + \frac{i}{\Delta^2})\omega^2\epsilon_0\mu_0] \sum_{j\geq 0} \Delta^j E_j^d(\mathbf{x}, \Delta) = 0 \tag{4.78}$$

which can also be written as operator form

$$\mathbb{L} \sum_{j\geq 0} \Delta^j E_j^c(\mathbf{x}, \Delta) = 0 \qquad \mathbb{L} = [\nabla \times \nabla \times \cdot - (1 + \frac{i}{\Delta^2})\omega^2\epsilon_0\mu_0\mathbb{I}] \tag{4.79}$$

The operators can also be expanded in power series using in terms of parameter Δ, which has been proved in detail in Ref. [105, 106].

$$\mathbb{L}[\Delta] = \frac{1}{\Delta^2} \sum_{n=0}^{\infty} \Delta^n \mathbb{L}^n \tag{4.80}$$

where individual terms of the series are

$$\mathbb{L}_\alpha^0(\mathbf{e}) = -\partial_3^2 e_\alpha - i\omega\epsilon_0\mu_0 e_\alpha \tag{4.81}$$

where, ∂_3 is the partial derivative with respect to $X_3 = \frac{\delta}{\Delta}$ and the vector field can be split in tangential and normal components $\mathbf{e} = (e_\alpha, e_N)$

$$\mathbb{L}_\alpha^1(\mathbf{e}) = -2b_\alpha^\beta \partial_3 e_\beta + \partial_3 D_\alpha e_N - i b_\beta^\beta \partial_3 e_\alpha \tag{4.82}$$

Thus, transverse components of $\mathbb{L}$ is $\mathbb{L}_3^n$

$$\mathbb{L}_3^0(\mathbf{e}) = -i\omega\epsilon_0\mu_0 e_N \tag{4.83}$$

With the change of metric tensor

$$a_{\alpha\beta}(\mathbf{e}) = \frac{1}{2}(D_\alpha e_\beta + D_\beta e_\alpha) - b_{\alpha\beta} e_N \tag{4.84}$$

$$\mathbb{L}_3^1(\mathbf{e}) = a_\alpha^\alpha(\partial\mathbf{e}) + b_\beta^\beta \partial_3 e_N \tag{4.85}$$

In order to calculate the relationship between the fields in dielectric and conductor region we have to use boundary conditions for the coefficients on surface S. The boundary conditions can be derived using the same method as equation 3.11 on equations 4.68 and 4.67.

$$\nabla \times \mathbf{E}_\Delta^c \times \mathbf{n} = \nabla \times \mathbf{E}_\Delta^d \times \mathbf{n} \tag{4.86}$$

$$\mathbf{E}_\Delta^c \times \mathbf{n} = \mathbf{E}_\Delta^d \times \mathbf{n} \tag{4.87}$$

The operator $\mathbb{T} = \nabla \times \cdot \times \mathbf{n}$ is in the local normal coordinate system and for $\mathbf{e} = (e_\alpha, e_N)$

$$(\mathbb{T}\mathbf{e})_\alpha = \partial_3^\Delta e_\alpha - D_\alpha e_N \tag{4.88}$$

After scaling the operator to $X_3 = \frac{\delta}{\Delta}$, we can expand it in the power of Δ

$$\mathbb{T}[\Delta] = \frac{\mathbb{T}^0}{\Delta} + \mathbb{T}^1 \tag{4.89}$$

where, the surface component terms can be derived using 4.88 and the scaling factor

$$\mathbb{T}_\alpha^0(\mathbf{e}) = \partial_3 e_\alpha \qquad \mathbb{T}_\alpha^1(\mathbf{e}) = -D_\alpha e_N \tag{4.90}$$

Thus, the boundary condition on surface S becomes,

$$\mathbb{T}[\Delta] \sum_{n\geq 0} \Delta^n \mathbf{e}(x_\alpha, 0) = \sum_{n\geq 0} \Delta^n \nabla \times \mathbf{E}_n^d \times \mathbf{n} \tag{4.91}$$

From definition of operator $\mathbb{T}$, we get

$$\mathbb{T}_\alpha^0(\mathbf{e}_0) = 0 \tag{4.92}$$

and

$$\mathbb{T}_\alpha^0(\mathbf{e}_0) + \mathbb{T}_\alpha^0(\mathbf{e}_0) = (\nabla \times \mathbf{E}_n^d \times \mathbf{n})_\alpha \tag{4.93}$$

Thus for first asymptotic $n = 0$, $\mathbf{e}_0$ wave equation and boundary condition become

$$\partial_3^2 \mathbf{e}_0(x_\alpha, X_3) - i\omega^2 \epsilon_0 \mu_0 \mathbf{e}_0(x_\alpha, X_3) = 0 \tag{4.94}$$

$$\partial_3 \mathbf{e}_0(x_\alpha, 0) = 0 \tag{4.95}$$

Thus for a unique solution for e_0 such that $\mathbf{e}_0 \to 0$ when $X_3 \to \infty$, we get $\mathbf{e}_\alpha(x_\alpha, X_3) = 0$. Recalling $\mathbb{L}_3^0 = -i\omega^2 \epsilon_0 \mu_0 e_N$, the zeroth order field inside the conductor is zero.

$$\mathbf{e}(x_\alpha, X_3) = 0 \tag{4.96}$$

Thus, for the dielectric region

$$\begin{aligned} [\nabla \times \nabla \times \cdot - \omega^2 \epsilon_0 \mu_0] \Delta^j E_0^d(\mathbf{x}) &= 0 \\ E_0^d(\mathbf{x}) \times \mathbf{n} &= 0 \end{aligned} \tag{4.97}$$

The next term $n = 1$,

Observing that the series has common terms for order of Δ, we get

$$\mathbb{L}^0(\mathbf{e}_0) = 0 \qquad \mathbb{L}^0(\mathbf{e}_1) + \mathbb{L}^1(\mathbf{e}_0) = 0 \qquad \sum_{m=0}^{n} \mathbb{L}^{n-m}(\mathbf{e}_m) = 0 \tag{4.98}$$

$$\partial_3^2 \mathbf{e}_1(x_\alpha, X_3) - i\omega^2 \epsilon_0 \mu_0 \mathbf{e}_1(x_\alpha, X_3) = 0 \tag{4.99}$$

$$\partial_3 \mathbf{e}_1(x_\alpha, 0) = E_0^d(\mathbf{x}) \times \mathbf{n}(x_\alpha, 0) \tag{4.100}$$

In order to solve the partial differential equations, we use a common trick

$$E_0^d(\mathbf{x}) \times \mathbf{n}(x_\alpha, 0) = \kappa \mathbf{R}_\alpha(x_\alpha) \tag{4.101}$$

where $\kappa = e^{-i\frac{\pi}{4}}\omega\sqrt{\epsilon_0\mu_0}$

$$\mathbf{e}_1(x_\alpha, X_3) = -\mathbf{R}(y_\alpha)e^{-\kappa\frac{\delta}{\Delta}} = -(E_0^d(\mathbf{x}) \times \mathbf{n}(x_\alpha, 0))e^{-\kappa\frac{\delta}{\Delta}} \tag{4.102}$$

For the dielectric part

$$\begin{aligned} [\nabla \times \nabla \times \cdot - \omega^2\epsilon_0\mu_0]\Delta^j E_1^d(\mathbf{x}) &= 0 \\ E_1^d(\mathbf{x}) \times \mathbf{n} &= -E_0^d(\mathbf{x}) \times \mathbf{n} \times \mathbf{n} \end{aligned} \tag{4.103}$$

For the next term $n = 2$, surface component becomes

$$\partial_3^2 \mathbf{e}_{2,\alpha}(x_\alpha, X_3) - i\omega^2\epsilon_0\mu_0 \mathbf{e}_{2,\alpha}(x_\alpha, X_3) = -2b_\alpha^\eta \partial_3 \mathbf{e}_{1,\eta}(x_\alpha, X_3) + b_\beta^\eta \partial_3 \mathbf{e}_{1,\alpha}(x_\alpha, X_3) \tag{4.104}$$

$$\partial_3 \mathbf{e}_{2,\alpha}(x_\alpha, 0) = (E_1^d(\mathbf{x}) \times \mathbf{n})_\alpha(x_\alpha, 0) \tag{4.105}$$

Thus,

$$\mathbf{e}_{2,\alpha}(x_\alpha, X_3) = [-\mathbf{R}_{1,\alpha} + (\frac{1}{\kappa} + X_3)(b^\eta_\alpha \mathbf{R}_{0,\eta} - H\mathbf{R}_{0,\alpha})](x_\beta)e^{-\kappa\frac{\delta}{\Delta}} \quad (4.106)$$

where,

$$E^d_1(\mathbf{x}) \times \mathbf{n}(x_\alpha, 0) = \kappa \mathbf{R}_{0,\alpha}(x_\alpha) \quad (4.107)$$

and the normal component

$$\mathbf{e}_2(x_\alpha, X_3) = -\frac{1}{\kappa} D_\alpha \mathbf{R}_{0,\alpha}(x_\beta) x_\beta e^{-\kappa\frac{\delta}{\Delta}} \quad (4.108)$$

In order to calculate the magnetic field in the conductor region we can use Faraday's law in generalized coordinates using Levi-Civeta matrix (ϵ^{ijk}),

$$(\nabla \times \mathbf{e})^\alpha = \epsilon^{3\beta\alpha}(\partial^\delta_3 \mathbf{e}_\beta - \partial_\beta \mathbf{e}) \quad (4.109)$$

$$(\nabla \times \mathbf{e})^3 = \epsilon^{3\beta\alpha} D^\delta_\alpha \mathbf{e}_\beta \quad (4.110)$$

The contravariant components (ϵ^{ijk}) depend depend on normal coordinate δ

$$(\epsilon^{ijk}) = (deto_{\alpha\beta}(\delta))^{-\frac{1}{2}} \epsilon_0(i, j, k) \quad (4.111)$$

which implies

$$(\epsilon^{ijk}) = o^{-\frac{1}{2}}(1 + 2H\delta + O(\delta^2))\epsilon_0(i, j, k) \quad (4.112)$$

4.1.5 Physical Interpretation

In the simplest interpretation of the results are

- $n = 0$ Perfect conductor condition as there is no penetration

- $n = 1$ Real conductor condition
- $n = 2$ Conductor with curvature condition

The results obtained in the equations 4.102 & 4.104 show that the fields inside the conducting volume is function of geometry.

$$\mathbf{E}_{conductor} = \mathbf{E}(H, b^{\alpha}_{\eta}) \tag{4.113}$$

We can explore ways the use of geometry to tailor losses in meta-structures by representing them as accurate current distribution and polarizations in order to understand the dynamics necessary to achieve magnetic dipole flipping. The total induced current can be decomposed in electric and magnetic current densities.

$$\mathbf{j}(\mathbf{r}) = \mathbf{j}_p(\mathbf{r}) + \mathbf{j}_m(\mathbf{r}) \qquad \mathbf{j}_p(\mathbf{r}) = \frac{\partial \mathbf{P}(H, K, t)}{\partial t} \qquad \mathbf{j}_m(\mathbf{r}) = \nabla \times \mathbf{M}(H, K, t) \tag{4.114}$$

The geometrical dependence of charge and current densities lead to *geometric dependence of material response* as shown by

$$\mathbf{D}(\mathbf{r}, t) = \epsilon_0 \mathbf{E}(\mathbf{r}, t) + \mathbf{P}(H, K, t) \tag{4.115}$$

$$\mathbf{B}(\mathbf{r}, t) = \mu_0 \mathbf{H}(\mathbf{r}, t) + \mathbf{M}(H, K, t) \tag{4.116}$$

4.2 Dynamics

In this section, we will describe the dynamics of the interaction of localized modes of current distribution with the incident electromagnetic fields. The dynamics of these modes decay due to radiation and ohmin losses and gets perturbed by the presence of other structure. This method is different from the traditional quantum electrodynamics method because the modes localized is quantized making it semi-classical. However, this method can also be used for quantum metamaterials by replacing the finite current distribution by quantized distribution.

We can tie together various applications of structured materials in one method using concepts of quantum electrodynamics for the dynamics of interaction, and differential geometry to incorporate the geometry of structures in the framework of meta-electrodynamics. Stated simply, in this method meta-atoms are represented as multipoles generated by induced current distributions which interact with each other and with the substrate to produce observable far-field effects. The problem statement can be generalized with the help of mathematical techniques which exploit the presence or lack symmetry of individual structure and ensembles of them. The coupling between various structures provides a method to control the decay rates and local current distributions enabling tailoring of radiation patterns in individual structures.

We propose to develop a new method to develop a precise understanding of the structure and dynamics of meta-structures providing better control of internal and external degree of freedoms for realization of many applications. This provides an elegant way to develop modes of the field distribution in ensembles of meta-atoms incorporating effects of shape of meta-surfaces on the observed fields. It allows one to span the range of metamaterials being operated at radio-frequencies to quantum metamaterials in a single formulation. Hence, Green's functions combined with effect of coupling should provide a good platform to understand metamaterials from physical point of view. Now, let us look at the important components required to understand the dynamics of such interactions.

4.2.1 Dynamical Variables

From Maxwell's equations, we can see that the rate of change of electric and magnetic fields with respect to time depends on their spatial derivatives in the neighborhood of point $\mathbf{r}$. In the reciprocal space, fields can be derived from spatial Fourier transform

$$\mathfrak{E}(\mathbf{k},t)=\frac{1}{(2\pi)^{\frac{3}{2}}}\int d^3r\mathbf{E}(\mathbf{r},t)e^{-i\mathbf{k}\cdot\mathbf{r}} \tag{4.117}$$

$$\mathbf{E}(\mathbf{r},t)=\frac{1}{(2\pi)^{\frac{3}{2}}}\int d^3k\mathfrak{E}(\mathbf{r},t)e^{-i\mathbf{k}\cdot\mathbf{r}} \tag{4.118}$$

Table 4.2: Real and reciprocal representation of electromagnetic quantities.

Physical quantity	Space-time	Reciprocal-time
Electric Field	$\mathbf{E}(\mathbf{r},t)$	$\mathfrak{E}(\mathbf{k},t)$
Magnetic Field	$\mathbf{H}(\mathbf{r},t)$	$\mathfrak{H}(\mathbf{k},t)$
Electric Displacement	$\mathbf{D}(\mathbf{r},t)$	$\mathfrak{D}(\mathbf{k},t)$
Magnetic Induction	$\mathbf{B}(\mathbf{r},t)$	$\mathfrak{B}(\mathbf{k},t)$
Vector Potential	$\mathbf{A}(\mathbf{r},t)$	$\mathfrak{A}(\mathbf{k},t)$
Scalar Potential	$\mathbf{\Phi}(\mathbf{r},t)$	$\mathfrak{P}(\mathbf{k},t)$
Charge Density	$\rho(\mathbf{r},t)$	$\mathfrak{R}(\mathbf{k},t)$
Current Density	$\mathbf{j}(\mathbf{r},t)$	$\mathfrak{I}(\mathbf{k},t)$

We can use the definitions above to derive Maxwell's equations in reciprocal-time domain and using the definitions of longitudinal vector quantities,

$$i\mathbf{k}\times\mathfrak{V}_{\parallel}(\mathbf{k})=0 \tag{4.119}$$

Transverse vector quantities

$$i\mathbf{k}\cdot\mathfrak{V}_{\perp}(\mathbf{k})=0 \tag{4.120}$$

we can get longitudinal and transverse components of electromagnetic quantities. From Maxwell's equations it becomes evident that magnetic field is purely transverse

$$i\mathbf{k}\cdot\mathfrak{B}(\mathbf{k},t)=0 \tag{4.121}$$

and decomposing a vector into its longitudinal and transverse components

$$\begin{aligned}\mathfrak{V}_{\parallel}(\mathbf{k})&=\hat{\mathbf{k}}[\hat{\mathbf{k}}\cdot\mathfrak{V}(\mathbf{k})]\\ \mathfrak{V}_{\perp}(\mathbf{k})&=\mathfrak{V}(\mathbf{k})-\mathfrak{V}_{\parallel}(\mathbf{k})\end{aligned} \tag{4.122}$$

we find that the longitudinal electric field is not dynamic in nature

$$\mathfrak{E}(\mathbf{k},t)=-\frac{i}{\epsilon_0}\frac{\mathbf{k}}{k^2}\mathfrak{P}(\mathbf{k}) \tag{4.123}$$

Thus, the dynamics is contained in the transverse components of the electromagnetic quantities. From Maxwell's equations, we can derive the dynamic equations

$$\begin{aligned}\frac{\partial}{\partial t}\mathfrak{B}&=-i\mathbf{k}\times\mathfrak{E}_{\perp}\\ \frac{\partial}{\partial t}\mathfrak{E}_{\perp}&=-\frac{i}{\epsilon_0\mu_0}\mathbf{k}\times\mathfrak{B}-\frac{1}{\epsilon_0}\mathfrak{J}_{\perp}\end{aligned} \tag{4.124}$$

Note,

- The source term is $\mathfrak{J}_{\perp}$ and not $\mathfrak{J}$ but in real the relationship between $\mathbf{j}_{\perp}$ and $\mathbf{j}$ is non-local hence the dynamics at any time t is affected by current at every point. This comes very subtle aeguments of delta function. (see page 14 Ref. [39]).

Equation 4.124 can be used to derive a set of normal variables with normalization constant $\Lambda(k)$

$$\mathbf{a}(\mathbf{k},t)=-\frac{i}{2\Lambda(k)}[\mathfrak{E}_{\perp}(\mathbf{k},t)-\frac{1}{\sqrt{\epsilon_0\mu_0}}\hat{\mathbf{k}}\times\mathfrak{B}_{\perp}(\mathbf{k},t)] \tag{4.125}$$

$$\mathbf{b}(\mathbf{k},t) = -\frac{i}{2\Lambda(k)}[\mathfrak{E}_{\perp}(\mathbf{k},t) + \frac{1}{\sqrt{\epsilon_0\mu_0}}\hat{\mathbf{k}} \times \mathfrak{B}_{\perp}(\mathbf{k},t)] \tag{4.126}$$

Using the complex conjugate properties of the reciprocal fields

$$\mathbf{b}(\mathbf{k},t) = -\mathbf{a}^{*}(-\mathbf{k},t) \tag{4.127}$$

Thus, we get the dynamic nature of the fields can be encapsulated in one term $\mathbf{a}(\mathbf{k},t)$

$$\mathfrak{E}_{\perp}(\mathbf{k},t) = i\Lambda(k)[\mathbf{a}(\mathbf{k},t) - \mathbf{a}^{*}(-\mathbf{k},t)] \tag{4.128}$$

$$\mathfrak{B}(\mathbf{k},t) = \frac{i\Lambda(k)}{\sqrt{\epsilon_0\mu_0}}[\hat{\mathbf{k}} \times \mathbf{a}(\mathbf{k},t) + \hat{\mathbf{k}} \times \mathbf{a}^{*}(-\mathbf{k},t)] \tag{4.129}$$

Thus, similar expression can be derived for vector potentials using

$$\mathbf{E}_{\perp}(\mathbf{r},t) = -\frac{\partial}{\partial t}\mathbf{A}_{\perp}(\mathbf{r},t) \tag{4.130}$$

$$\mathbf{B}(\mathbf{r},t) = \nabla \times \mathbf{A}_{\perp}(\mathbf{r},t) \tag{4.131}$$

Now, let us look at a method using which Lagrangian and Hamiltonian of the interactions.

4.2.2 Lagrangian and Hamiltonian Formulations

The Lagrangian for the system made up of particles interacting with the electromagnetic field is derived as a function of dynamic variable of each particle. In standard formalism, the position vector and it's time derivative serves as the dynamical variable and electromagnetic potentials for the incident fields because the equations of motion are second order. The dynamics of the system of particles + electromagnetic field can be derived from standard Lagrangian

$$L = \sum_i \frac{1}{2} m_i \dot{\mathbf{r}}_i^2 + \frac{\epsilon_0}{2} \int d^3r [\mathbf{E}^2(\mathbf{r}) - c^2 \mathbf{B}^2(\mathbf{r})] + \sum_i [q_i \dot{\mathbf{r}}_i \cdot \mathbf{A}(\mathbf{r}_i) - q_i \Phi(\mathbf{r}_i)] \qquad (4.132)$$

The Lagrangian has three terms

For particles

$$L_p = \sum_i \frac{1}{2} m_i \dot{\mathbf{r}}_i^2 \qquad (4.133)$$

For the electromagnetic fields

$$L_{EM} = \frac{\epsilon_0}{2} \int d^3r [\mathbf{E}^2(\mathbf{r}) - c^2 \mathbf{B}^2(\mathbf{r})] \qquad (4.134)$$

For interaction

$$L_I = \sum_i [q_i \dot{\mathbf{r}}_i \cdot \mathbf{A}(\mathbf{r}_i) - q_i \Phi(\mathbf{r}_i)] = \int d^3r [\mathbf{j}(\mathbf{r}) \cdot \mathbf{A}(\mathbf{r}) - \rho(\mathbf{r}) \Phi(\mathbf{r})] \qquad (4.135)$$

Without going in rigorous detail, using the method developed in Ref. [39], the conjugate momentum can be written as

$$\Pi(\mathbf{r}) = \frac{\partial L}{\partial \dot{\mathbf{A}}(\mathbf{r})} = \epsilon_0 \dot{\mathbf{A}}(\mathbf{r}) = \mathbf{D}_\perp(\mathbf{r}) \qquad (4.136)$$

The Hamiltonian is given by

$$H = \int d^3r \Pi(\mathbf{r}) \dot{\mathbf{A}}(\mathbf{r}) - L \qquad (4.137)$$

Thus, Hamiltonian as a function of fields in real space

$$H = \sum_i \frac{1}{2m_i}[\mathbf{p}_i - q_i\mathbf{A}(\mathbf{r}_i)]^2 + V_{Coul} + \frac{\epsilon_0}{2}\int d^3r[(\frac{\Pi}{\epsilon_0})^2 + c^2(\nabla \times \mathbf{A})^2] \qquad (4.138)$$

where, $\mathbf{p}_i = m\dot{\mathbf{r}}_i + q_i A_i(\mathbf{r})$ is the momentum associated with the discrete variable

4.2.3 Charge Coupled with External Fields

In order to understand the transformation required to understand the interaction of current distribution with incident field we will see an example of localized charge around the origin interacting with external electromagnetic field described by potentials $A_e(\mathbf{r}, t)$ and $\Phi_e(\mathbf{r}, t)$. The Lagrangian and Hamiltonian which are functions of dynamical variable of particles only,

$$L = \sum_i \frac{1}{2}m_i\dot{\mathbf{r}}_i^2 - V_{Coul} + \sum_i [q_i\dot{\mathbf{r}}_i \cdot A_e(\mathbf{r}, t) - q_i\Phi_e(\mathbf{r}, t)] \qquad (4.139)$$

$$H = \sum_i \frac{1}{2m_i}[\mathbf{p}_i - q_i\mathbf{A}(\mathbf{r}_i)]^2 + V_{Coul} + \sum_i q_i\Phi_e(\mathbf{r}, t) \qquad (4.140)$$

Under the long wavelength where the localized charges form a globally neutral system

$$\sum_i q_i = 0 \qquad (4.141)$$

where, the spatial extent a_s is small with respect to the length of variation of $A_e(\mathbf{r}, t)$ and $\Phi_e(\mathbf{r}, t)$ which is the wavelength of incident field. Upon expanding the potentials into multipole moments and for the lowest order term, the dipole approximation

$$\mathbf{d} = \sum_i q_i\mathbf{r}_i \qquad (4.142)$$

Under this approximation, the Lagrangian becomes

$$L = \sum_i \frac{1}{2} m_i \dot{\mathbf{r}}_i^2 - V_{Coul} + \dot{\mathbf{d}} \cdot A_e(\mathbf{0}, t) - \mathbf{d} \cdot \nabla \Phi_e(\mathbf{0}, t)] \tag{4.143}$$

The momentum conjugate with $\mathbf{r}_i$

$$\mathbf{p}_i = m\dot{\mathbf{r}}_i + q_i A_e(\mathbf{0}, t) \tag{4.144}$$

The Hamiltonian becomes

$$H = \sum_i \frac{1}{2m_i} [\mathbf{p}_i - q_i \mathbf{A}(\mathbf{0}, t)]^2 + V_{Coul} + \mathbf{d} \cdot \nabla \Phi_e(\mathbf{0}, t) \tag{4.145}$$

4.2.4 Power-Zienau-Woolley Transformation

The Lagrangian can be derived by using the Power-Zienau-Woolley Transformation [39] where the incident field is considered as a dynamical system interacting with distribution of charge and current density. The advantages of using this approach are that the coupling between fields and current is expressed as function of electric and magnetic field and no longer has to be a function of vector potential. The system of charges and current densities can be described by polarization and magnetization densities which are functions of macroscopic variables, geometry and incident-radiation time dependence. This provides a rigorous basis to develop the electrodynamics of structured material where the displacement vector **D** is introduced naturally as momenta-conjugate with vector potential. Thus, by using the multipole moments of charge and current distributions we can get multipole expansion of interaction of light with structured materials. This also delineates the magnitude of the multipole moments and coupling Hamiltonian when the system is extended. This generalization makes the method valid for single meta-atom or an ensemble.

As shown in section 4.1.2 the current densities can be engineered using geometry of structures. The polarization and magnetization densities characterize the behavior of materials under the influence of incident fields and are zero outside the structure.

$$\mathbf{D}(\mathbf{r}) = \epsilon_0 \mathbf{E}(\mathbf{r}) + \mathbf{P}(\mathbf{r}) \tag{4.146}$$

Considering, it's divergence

$$\nabla \cdot \mathbf{D}(\mathbf{r}) = \epsilon_0 \nabla \cdot \mathbf{E}(\mathbf{r}) + \nabla \cdot \mathbf{P}(\mathbf{r}) \tag{4.147}$$

The electric displacement can be separated into parallel and perpendicular components and for a electrically neutral system $\rho(\mathbf{r}) = 0$,

$$\begin{gathered} \mathbf{D}_{\parallel} = \mathbf{0} \\ \mathbf{D} = \mathbf{D}_{\perp} \end{gathered} \tag{4.148}$$

which implies,

$$\mathbf{P}_{\parallel}(\mathbf{r}) = \epsilon_0 \mathbf{E}_{\parallel}(\mathbf{r}) \tag{4.149}$$

Thus, Coulomb energy which is the energy of longitudinal fields becomes

$$V_{Coul} = \frac{1}{2\epsilon_0} \int d^3 r \mathbf{P}_{\parallel}^2(\mathbf{r}) \tag{4.150}$$

The variation of current produces a change in polarization density along with continuity equation, we get the polarization current density.

$$\dot{\rho} + \nabla \cdot \dot{\mathbf{P}} = 0 \tag{4.151}$$

And the total current can be written as sum of polarization and magnetization current densities, $\mathbf{j}(\mathbf{r}) = \mathbf{j}_P(\mathbf{r}) + \mathbf{j}_M(\mathbf{r})$, where

$$\begin{aligned} \mathbf{j}_P(\mathbf{r}) &= \frac{\partial \mathbf{P}(\mathbf{r})}{\partial t} \\ \mathbf{j}_M(\mathbf{r}) &= \nabla \times \mathbf{M}(\mathbf{r}) \end{aligned} \tag{4.152}$$

In order to include the accurate current distributions Power, Zienau and Woolley introduced

$$F = -\int d^3r \mathbf{P}(\mathbf{r}) \cdot \mathbf{A}(\mathbf{r}) \tag{4.153}$$

which changes the interaction Lagrangian

$$L_I' = L_I + \frac{\partial F}{\partial t} = \int d^3r \mathbf{j} \cdot \mathbf{A} - \int d^3r [\dot{\mathbf{P}} \cdot \mathbf{A} + \mathbf{P} \cdot \dot{\mathbf{A}}] \tag{4.154}$$

substituting the relationships of current densities

$$L_I' = \int d^3r (\nabla \times \mathbf{M}) \cdot \mathbf{A} - \int d^3r \mathbf{P} \cdot \dot{\mathbf{A}} \tag{4.155}$$

Using integration by parts and definition of vector potentials, we get

$$L_I' = \int d^3r \mathbf{M} \cdot \mathbf{B} + \int d^3r \mathbf{P} \cdot \mathbf{E}_\perp \tag{4.156}$$

Thus, the interaction can be expressed as localized polarization density with electric field and magnetization density with magnetic field.

Similarly, the term for single particle containing the inertia,

$$L = \sum_i \frac{1}{2} m_i \dot{\mathbf{r}}_i^2 \tag{4.157}$$

can be modified using the dynamic distribution of charge ($\mathbf{I}$) which would lead to kinetic inductance (l_k) energy

$$L_{Kinetic} = \sum_i \frac{1}{2} l_k \dot{\mathbf{I}}^2 \tag{4.158}$$

4.3 Characterization of Interactions

The research for interaction of light with structured materials is heavily dependent on the computation and thus lacks inherent physical intuition. Currently, the most popular technique for analysis of such structures is finite-element analysis using commercial software. These programs are heavily mesh-dependent and are programmed to provide quick solutions using equations which may not be valid at the mesoscale. Recent papers [31] have discussed the factors that were missed using such programs, especially in non-linear applications. There have been studies where finite-element methods break down for deeply subwavelength structures [61]. But this issue can be resolved by using electromagnetic potentials instead of fields Various homogenization methods are used to average the effects of ensemble of meta-atoms over the volume of unit cells. These homogenization methods fail to capture the multiple-scattering effects that may lead to localization of fields within a system. In general, it is assumed that each meta-atom is only excited by the incident waves but the spacing between adjacent meta-atoms is subwavelength, which leads to strongly scattered fields acting as input fields for other meta-atoms. Accurate analyses of strong interactions between a metamaterial's unit cells often requires simplifying assumptions, such as the elements being arranged in an infinite lattice. But the discrete nature of metamaterials becomes apparent when the infinite lattice symmetry is broken [107, 108] and effects of local fields become more important. The strong interaction between these structures renders them very sensitive to finite size effects and to disorder in the lattice [109]. Strong interactions between resonators can find important applications in metamaterial systems, providing precise control and manipulation of EM fields on a subwavelength scale e.g., by localizing sub-diffraction-field hot spots, similar to

Anderson localization of electrons. Different methods are chosen depending on the application and the geometry of the meta-atom, which hinders development of an overall classification of these structures.

The major change in formulation can be observed when we transition from bulk bianisotropic media to bianisotropic meta-atoms. In the dipole approximation, the moments generated by the incident field are described as

$$\mathbf{p} = \overset{\leftrightarrow}{\alpha}_{ee} \cdot \mathbf{E}_{loc} + \overset{\leftrightarrow}{\alpha}_{em} \cdot \mathbf{H}_{loc} \tag{4.159}$$

$$\mathbf{m} = \overset{\leftrightarrow}{\alpha}_{me} \cdot \mathbf{E}_{loc} + \overset{\leftrightarrow}{\alpha}_{mm} \cdot \mathbf{H}_{loc} \tag{4.160}$$

It also important to realize that one meta-atom can support various modes of oscillation and hence during the calculation of various eigenmodes is essential. The study of interaction between various eigenmodes is also valuable as under certain circumstances unexpected results can be observed. Modal analysis of light interaction with cylinders have shown the existence of resonances at certain frequencies which may affect the scattering properties [19]. However, the analysis becomes increasingly cumbersome when the geometry becomes more complex which makes it imperative to develop a framework that capable of handling complex configurations using differential geometry. Geometric effects may introduce non-linearity which can be studied using the multipole method described earlier. There have been papers showing that negative index can be achieved away from resonances by exploiting chirality [29] and bianisotropy. This can pave the path for low-loss metamaterials for applications in time reversal.

The polarizability coefficients are geometry dependent and in case of spheres they can be derived using the Mie coefficients. Under the dipole approximation, interactions between various modes of combination of sphere such as dimer and trimer [110] can create a perfect bianisotropic meta-atom. There have been efforts to develop multipole nonlinearity of metamaterials using a hydrodynamic model where the modes are generated by localized charge densities located at certain positions. However, a complete dynamic description would require calculation of current distributions not making prior assumptions as to the location of charge densities.

4.4 Conclusions

The ecosystem of metamaterials consists of a wide variety of resonator geometries, hence analyzing them using one framework is a complex task. Meta-atoms can be composed of metallic structures supporting plasmonic oscillations, allowing internal current flows. The dielectric meta-atoms have a system of surface current that are induced based on the geometry. As we saw in previous section, the multipole moments are dependent on the accurate determination of current distribution. Currently, there are no rigorous methods available to map structure to function and computations are mostly dominated by mesh-dependent methods. We extend the method developed to describe light interaction with the general bianisotropic structures. Identification of the spatial profiles or eigenmodes of the structure with one formalism is complex because the coordinate system is dependent on the geometry of interfaces and associated boundary conditions. Use of differential geometry simplifies the identification process of the eigenmode bases which can be supported by the structure at certain incident wavelengths. Structures are capable of supporting multiple modes, hence can produce a combined effects due to mode interference. The geometrical information about the structure can be expressed in the metric tensor. The first and second fundamental forms are derived by a parametrization of the structure. This is extremely important for analyzing 2.5D structures, where the local analysis can be done in three dimensions and third dimension can be set to zero capturing the 3D interaction effects. This gives an extra degree of freedom by assigning multiple modes of current oscillation to each meta-atom, each with its own dynamic variable and mode function to describe the corresponding polarization and magnetization densities. For simplification of the problem, each meta-atom can be assumed to possess only a single mode of current oscillation. This is analogous to approximating an atom interacting with the EM field as a two-level atom.

Mapping an observed function to structure as an inverse problem often leads to non-unique solutions. Various numerical methods have been discussed in the literature [45] but they are computationally very expensive. The classification of structures is also a complex task due to the wide variety of geometries employed. Hence, classifying structures based on the presence or lack of geometry seems to be an excellent starting point. Using the methodology used in chemistry to classify molecules based on group theory we can start to put together a table of structure based on symmetry [111]. Stereo-metamaterials [112] is a novel class of metamaterials where meta-molecules are classified by techniques that are inspired by chemistry. It demonstrates the effect of change in dynamics of current densities and observed properties based on relative angle between two split-ring resonators. There have been other efforts to classify 3D meta-molecules using group theory, augmenting the inverse methods [40]. We will develop a group-theory-based technique combined with the interacting multipole method for analyzing 3D meta-molecules (oligomers). For example, molecules in chemistry can be identified as IR- or Raman-active by just their symmetry group without any actual modal solution governing the equation of motions of the particles [113]. Comparing the molecules in chemistry to meta-atoms, the vibrational modes can be equivalent to the fundamental modes of the meta-structure and hence principles of point group and symmetry can be exploited to obtain structure from function and classify meta-structures. The method discussed above is appropriate for classification based on electromagnetic response as identification of modes of structures and effects on dynamics of current densities on constitutive relations are essential.

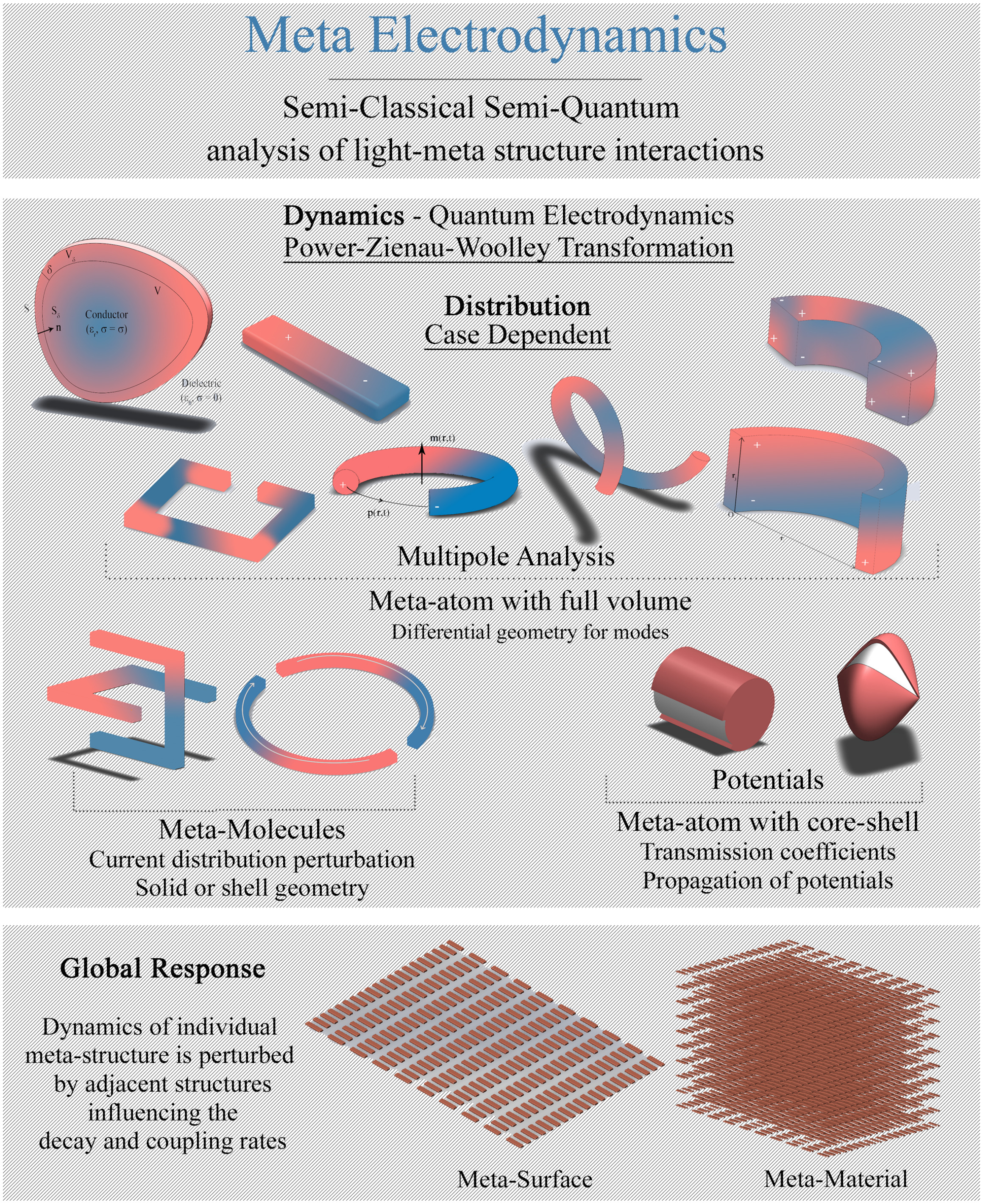

Figure 4.9: Pictorial summary of Meta-Electrodynamics.

CHAPTER 5: TIME REVERSAL USING META-MOLECULES

In chapters 2 and 3, we have studied the propagation of electromagnetic waves through structures and obtained geometry based reflection and transmission coefficients. In chapter 4, we have studied behavior of fields inside the volume of the geometry by determining the distribution of current densities based on geometry. The induced current density can be decomposed into multipole moments and their interactions can be used to engineer large number of interactions. Multipole analysis provides understanding of minutiae details of interactions of meta-atoms in various metamaterials for linear and non-linear applications such as second harmonic generations [114]. Another building block of metamaterials are meta-molecules which provides a method to tailor individual multipole moment of the unit structure. In this chapter, we will present a method to analyze a meta-molecule which can be used for time reversal of signals.

The issue of time reversal has been addressed for acoustic [115, 116] and electromagnetic [117] waves. In a non dissipative medium, for every wave produced by a source there exists a time reversed wave that retraces the path exactly and converges to the source location. In the basic experiment, the forward propagating wave is captured over a sufficiently long time window and the recorded signal is phase conjugated before being propagating back in the same medium. Consider, a incident scalar wave propagating in positive z direction,

$$E_1(\mathbf{r}) = \Re[\psi(\mathbf{r})e^{-i(kz-\omega t)}] \tag{5.1}$$

when it is substituted in the scalar wave equation we have,

$$\nabla^2\psi - 2ik\frac{\partial\psi}{\partial z} + [\omega^2\mu\epsilon(\mathbf{r}) - k^2]\psi = 0 \tag{5.2}$$

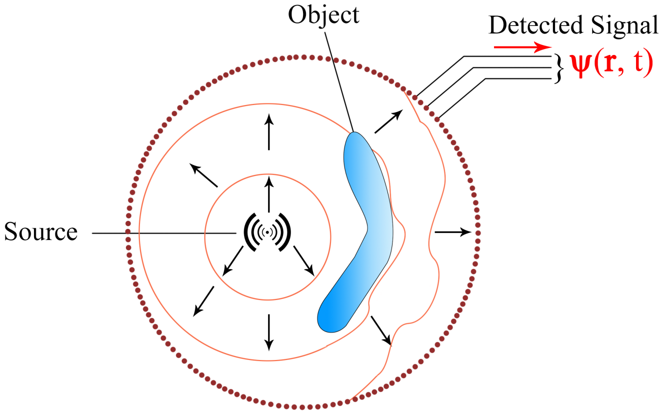

Figure 5.1: Detection of scattered field.

The complex conjugate of the wave equation,

$$\nabla^2\psi^* + 2ik\frac{\partial\psi^*}{\partial z} + [\omega^2\mu\epsilon(\mathbf{r}) - k^2]\psi^* = 0 \tag{5.3}$$

can be interpreted as describing the propagation of the wave in the negative z direction, which is opposite to $E_1(\mathbf{r})$ and having an amplitude complex conjugated at each point.

$$E_2(\mathbf{r}) = \Re[\psi^*(\mathbf{r})e^{i(\omega t+kz)}] \tag{5.4}$$

This one-to-one correspondence is the reason for reversing the distortions occurred during propagation effects by propagating the conjugated wave backward in the

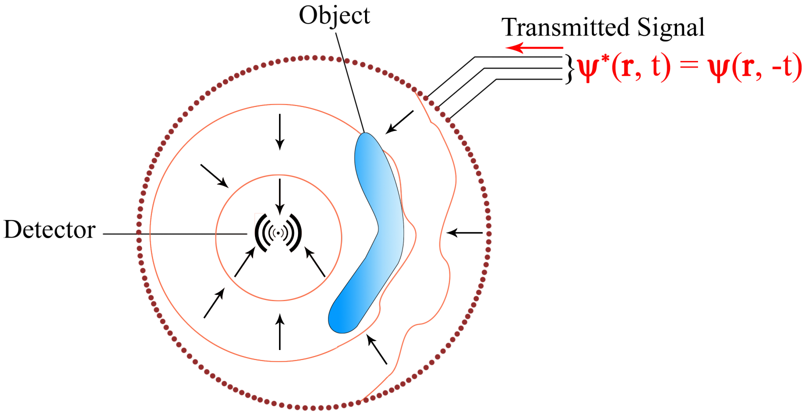

Figure 5.2: Propagation of phase conjugated waves in reverse direction.

medium which is equivalent to time reversal for unity gain [118].

Time reversal symmetry holds in a strongly heterogeneous medium which contains multiple scattering events of the incident waves. In order to have a complete understanding of how distortions can be corrected through phase conjugation, understanding the role of evanescent waves is very important and this has been studied by Nieto-Vesperinas and Wolf [119]. However, under phase conjugation the homogeneous and evanescent part of the waves behave differently. Depending on the space in which the waves propagate the phase conjugation of waves follow different rules. If the waves propagate in same half space then the evanescent waves are the complex conjugate of each other whereas homogeneous wave are the complex conjugate of the reflected waves. If the waves propagate in complimentary half space then the homogeneous waves are the complex conjugate of each other whereas evanescent wave are the complex conjugate of reflected waves. Hence, for any wave containing both homogeneous and evanescent components together, phase conjugation is not equivalent to time reversal in the presence of losses. Thus, for time reversal with subwavelength resolution it is not enough to have conjugate media but two metasurfaces should be complimentary to each other.

The time-reversal in presence of losses becomes complicated as time reversed version of a passive lossy scattering event is an event active one. Phase conjugation can be equivalent to time reversal in presence of evanescent waves only if gain is equal to loss [118]. Time reversal experiments in presence of losses are difficult but non-perturbative computational methods provide a solution to the problem. But inverse methods have non-unique solutions and suffer from issues of convergence, hence the reconstructions are not accurate and suffer from issues of noise.

Evanescent waves play an important role as they carry subwavelength information and decay exponentially before reaching the detector thereby limiting the reconstruction to the diffraction limit. It has been shown at microwave frequencies [120] that using a multiple scattering medium in the near field and back propagating the conjugated wave, two sources separated by subwavelength distances can be resolved. Time reversal with low losses reverses the multiple scattering and converts propagating waves back into correctly located evanescent waves thereby providing high resolution isolation. Exploiting multiple scattering in a positive and a complimentary negative index material can provide a way for analog coding and decoding of signal with high spatial resolution. This may be the first attempt to specifically design a time reversal metamaterial for analog coding and decoding exploiting densely packed scatterers (or sources). Subwavelength focusing using time-reversal can be used for various applications in telecommunications and RF broadcasting where it can increase the rate of data sent by increasing the number of antennas.

In our theoretical model, time reversal is used to image two sources placed at subwavelength separation. We do not have a phase conjugated wave being propagated backwards instead we are trying to code by scattering an image with subwavelength features. Traditionally, imaging strongly scattering objects requires a nonlinear inverse scattering algorithm capable of recovering images of subwavelength features but they are computationally expensive and suffer from issues of non-uniqueness and convergence. Fully reciprocal and complimentary materials that effect time reversal will inform us about reciprocal meta-structures and their ability to recover subwavelength scale features in a target by encoding near field with the help of a strong scatterer. Achieving negative refractive index in metamaterial requires using the structures at or near resonance frequencies, leading to very high losses. Exploiting shapes associated with low loss, such as, bianisotropic structures give us an opportunity to design local meta-atom and avoid exploiting resonant phenomenon which would keep losses low. This will allow antennas operating at different frequency ranges to be placed closely together without interference. It will also allow far field superresolved imaging to be achieved and should be scalable to higher frequencies.

5.1 Time Reversal and Reciprocity

The metasurfaces described in the setup are composed of electrically small resonators or meta-atoms. The size of the meta atoms dictate the type of multipole response and to avoid any non-linear effects, the size of the meta-atoms are restricted to have dipolar response. In this section, we discuss the effect of time reversal on these dipole moments. Under time reversal, the magnetic moments reverse their directions, while the electric moments remain unchanged as illustrated by figure 5.3. Hence, in a magnetoelectric model with parallel electric and magnetic dipole moments, then become antiparallel during time reversal. The form invariance of Maxwell's equations under time reversal ($\mathcal{T}$) gives

$$\begin{aligned}\mathcal{T}\mathbf{E}(t) &= \mathbf{E}(-t)\\ \mathcal{T}\mathbf{D}(t) &= \mathbf{D}(-t)\\ \mathcal{T}\mathbf{H}(t) &= -\mathbf{H}(-t)\\ \mathcal{T}\mathbf{B}(t) &= -\mathbf{B}(-t)\end{aligned} \tag{5.5}$$

For time harmonic fields, the complex vectors under time reversal can be written as complex conjugate

$$\begin{aligned}\mathcal{T}\mathbf{E} &= \mathbf{E}^*\\ \mathcal{T}\mathbf{D} &= \mathbf{D}^*\\ \mathcal{T}\mathbf{H} &= -\mathbf{H}^*\\ \mathcal{T}\mathbf{B} &= -\mathbf{B}^*\end{aligned} \tag{5.6}$$

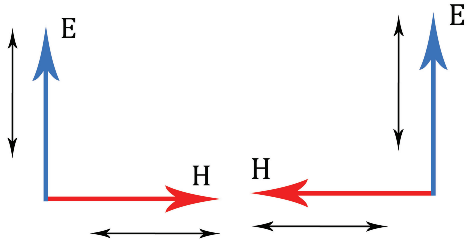

Figure 5.3: Illustration of the change in direction of magnetic dipole moment of meta-atoms under time reversal. The electric moment remains unchanged, hence to create two complimentary resonators or meta-atoms, the dipolar response should follow this scheme.

The two sets of electromagnetic fields for the coding metasurface ($\mathbf{E}_c$, $\mathbf{H}_c$) and the decoding metasurface ($\mathbf{E}_d$, $\mathbf{H}_d$) are generated by the electric and magnetic current densities of the individual meta-atoms. When ϵ and μ are Hermitian, a generalization of the energy flux conservation principle from Maxwell's equations becomes,

$$\nabla \cdot (\mathbf{H}_c^* \times \mathbf{E}_d + \mathbf{H}_d^* \times \mathbf{E}_c) = \mathbf{H}_d \mathbf{m}_c^* + \mathbf{H}_c \mathbf{m}_d^* + \mathbf{E}_d \mathbf{j}_c^* + \mathbf{E}_c \mathbf{j}_d^* \tag{5.7}$$

This indeed can be shown for the condition $\mathbf{m}_c = \mathbf{m}_d$, $\mathbf{j}_c = \mathbf{j}_d$, $\mathbf{E}_c = \mathbf{E}_d$ and $\mathbf{H}_c = \mathbf{H}_d$ and integrating over a closed surface $\delta\Gamma$ enclosing volume Γ gives the Poynting vector

$$\oint_{\delta\Gamma} \mathbf{P} d^2 r = -\frac{1}{2} \int_{\Gamma} Re(\mathbf{E}_c^* \cdot \mathbf{j}_c + \mathbf{H}_c^* \cdot \mathbf{m}_c) d^3 r \tag{5.8}$$

In its simplest form, the reciprocity theorem states that a system is reciprocal if the response of the system is unchanged if source and detector positions are interchanged. The reaction can be written as

$$< S, D >= \int_V \mathbf{J}_s \cdot \mathbf{E}_d dV \tag{5.9}$$

Under reciprocity $< S, D >=< D, S >$ but in order to design a complementary medium for time reversal of waves with evanescent components, the following relation should be satisfied, where $'c'$ stands for complimentary.

$$< S, D >^c =< D, S > \tag{5.10}$$

With the increase in complexity of a bianisotropic response of meta-atoms, the expression for reaction relation (equation 5.9) becomes complicated but can be used to derive essential relationships between constitutive parameters.

5.2 Role of Bianisotropy

It has been argued that a negative index makes a perfect lens [121] thus making it ideal for time reversal with subwavelength resolution. But achieving negative index by driving electric permittivity and magnetic permeability through two separate resonances leads to increased losses, especially at optical wavelengths. It was shown that a single chiral resonance can be utilized to achieve negative refraction for single polarization [122]. Similarly, bianisotropic structures can be used to achieve negative index by avoiding resonances. The response of bulk biansiotropic materials to an incident field is described by

$$\mathbf{D}(\mathbf{r},t) = \overset{\leftrightarrow}{\epsilon} \cdot \mathbf{E}(\mathbf{r},t) + \overset{\leftrightarrow}{\xi} \cdot \mathbf{H}(\mathbf{r},t) \tag{5.11}$$

$$\mathbf{B}(\mathbf{r},t) = \overset{\leftrightarrow}{\zeta} \cdot \mathbf{E}(\mathbf{r},t) + \overset{\leftrightarrow}{\mu} \cdot \mathbf{H}(\mathbf{r},t) \tag{5.12}$$

In a source free region for a non absorbing medium, the time average of the divergence of the Poynting vector vanishes $\langle \nabla \cdot \mathbf{S} \rangle = 0$, yielding a relationship.

$$\mathbf{H} \cdot \mathbf{B}^* - \mathbf{H}^* \cdot \mathbf{B} + \mathbf{E} \cdot \mathbf{D}^* - \mathbf{E}^* \cdot \mathbf{D} = 0 \tag{5.13}$$

In the presence of losses, where the energy is absorbed in the medium, the above relation is not valid and certain restrictions are imposed on the susceptibilty tensors based on Maxwell's equations and constitutive relations. The tensors $\overset{\leftrightarrow}{\epsilon}$ and $\overset{\leftrightarrow}{\mu}$ must be symmetric and non-negative definite. Hence, the tensor elements must satisfy the following conditions alongwith $\xi_{ij} = -\zeta_{ij}$

$$\epsilon_{ii} \geq 0 \qquad \mu_{ii} \geq 0 \qquad i = 1,2,3 \tag{5.14}$$

$$a_{ij}^2 \leq a_{ii}a_{jj} \qquad d_{ij}^2 \leq d_{ii}d_{jj} \qquad i = 1,2,3 \quad i \neq j \tag{5.15}$$

However, metasurfaces are composed of discrete resonators which localize the incident fields to achieve desired permeability and permittivity values. Hence, the description of a bianisotropic meta-atom is described by a different formalism in terms of electric and magnetic dipoles

$$\mathbf{p} = \overset{\leftrightarrow}{\alpha}_{ee} \cdot \mathbf{E}_{loc} + \overset{\leftrightarrow}{\alpha}_{em} \cdot \mathbf{H}_{loc} \tag{5.16}$$

$$\mathbf{m} = \overset{\leftrightarrow}{\alpha}_{me} \cdot \mathbf{E}_{loc} + \overset{\leftrightarrow}{\alpha}_{mm} \cdot \mathbf{H}_{loc} \tag{5.17}$$

Using the above relations we can now find the relation for reciprocal scatterers from the Onsager-Casimir principle [123]

$$\overset{\leftrightarrow}{\alpha}_{ee} = \overset{\leftrightarrow}{\alpha}_{ee}^{\;t} \qquad \overset{\leftrightarrow}{\alpha}_{mm} = \overset{\leftrightarrow}{\alpha}_{mm}^{\;t} \qquad \overset{\leftrightarrow}{\alpha}_{me} = -\overset{\leftrightarrow}{\alpha}_{em}^{\;t} \tag{5.18}$$

For passive meta-atoms, the imaginary part of the six-dyadic formed by four polarizabilities $(\overset{\leftrightarrow}{\alpha} - \overset{\leftrightarrow}{\alpha}^{t})$ is positive definite and scalar parameters satisfy the condition $\Im(\alpha_{he}\alpha_{eh}) < \Im(\alpha_{ee}\alpha_{hh})$. However, passivity does not impose any restriction on the real part of the six-dyadic $\overset{\leftrightarrow}{\alpha}$. In naturally occurring materials, the magnetoelectric coupling effects are negligible as compared to direct polarization effects. However with careful design of meta-atoms we can enhance these coupling effects. It is known that indirect coupling cannot be stronger than direct ones but for polarizabilties, metal spirals near their fundamental resonance for example follow the relation [124]

$$|\alpha_{he}\alpha_{eh}| = |\alpha_{ee}\alpha_{hh}| \tag{5.19}$$

However, for bianisotropic meta-atoms the cross terms cannot be exactly equal to the direct polarizability terms for passive scatterers. These terms for individual meta-atoms are modified due to adjacent meta-atoms. The overall Green's functions of the metasurface derived using the dipolar terms of individual meta-atoms can have fundamental a eigenfrequency different from the fundamental frequency of a single resonator. This is mainly due to multiple scattering events and can be analyzed using a multipole analysis of meta-atoms.

5.3 Time Reversal using Bianisotropic Metastructures

The traditional condition for the time reversal effect resulting from phase conjugation [125] are, finite size lossless scatterers. A phase conjugate mirror should not introduce any loss and gain and the mirror and observation plane should be far enough away to avoid evanescent waves. However, the new concept introduced here requires capturing the evanescent waves through strong multiple scattering and coupling and then propagating to the observation plane. Subwavelength resolution is achieved by placing a metasurface in the near field of the source to encode evanescent waves into propagating waves. After the propagation in free space, these evanescent waves can be decoded by a complementary metasurface in the near field of the detector. The setup imposes the condition that the coder should have refractive index near $+1$ and the decoder to have refractive index close to -1 to create a perfect imaging system. The analysis of the entire system can be done using Green's functions of the coder, free space and the decoder. Since, the surfaces are composed of discrete resonators, the Green's functions have to be derived using a bottom up approach where individual excitation and decay rate are considered along with perturbations introduced by multiple scattering events.

Meta-atoms composed of metals have inherent ohmic loss but dielectrics provide a solution for reducing such losses. In order to design reciprocal meta-atoms the geometry has to be asymmetric. It has been shown that half cut dielectric cylinders can form a reciprocal meta-atom. Multipole analysis can be used to analyze the scattered field from individual meta-atoms. The response can be altered due to strong interaction between the adjacent scatterers. In the simplest form meta-atoms can be approximated by dipoles with tensorial electric, magnetic, and magnetoelectric polarization coefficients. The forward and backward propagation of waves can be shown by using $\pm$ in the notation for extinction cross section, where $I_0 = |\mathbf{E}_{inc}|/2Z_0$ with free space impedance (Z_0)

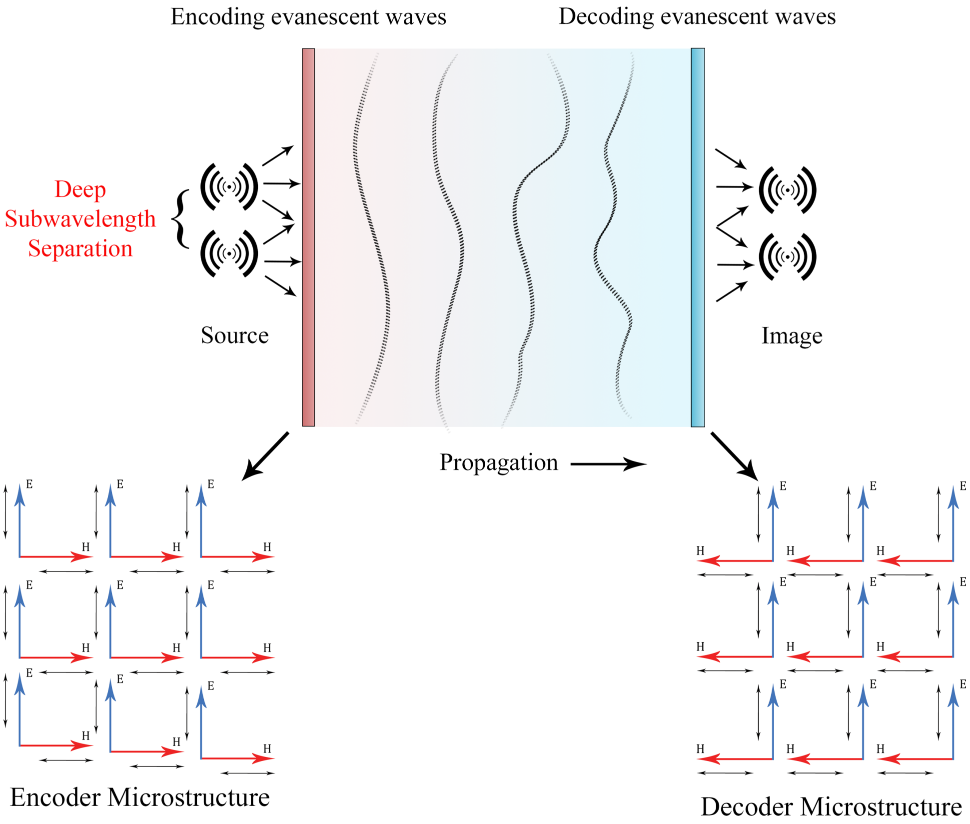

Figure 5.4: Schematic of the entire setup. A metasurface composed of bianisotropic scatterers placed in the near field of sources, the encoder. The field propagates and passes through a complimentary surface present in the near field of detector (the decoder) which reverses the multiple scattering events.

$$C_{ext}^{\pm} = \frac{P_{ext}^{\pm}}{I_0} = -\frac{1}{2I_0} Re \oint_s (\mathbf{E}_{inc} \times \mathbf{H}_{sca}^{\pm *} + \mathbf{E}_{sca}^{\pm} \times \mathbf{H}_{inc}^{*}) \cdot \mathbf{n} ds \tag{5.20}$$

By using the dipole expressions above

$$C_{ext}^{\pm} = kIm(\alpha_{ee} \pm \alpha_{eh} \pm \alpha_{he} + \alpha_{hh}) \tag{5.21}$$

For the scattering cross section

$$C_{sca}^{\pm} = \frac{P_{sca}^{\pm}}{I_0} = -\frac{1}{2I_0} Re \oint_s (\mathbf{E}_{sca} \times \mathbf{H}_{sca}^{\pm *}) \cdot \mathbf{n} ds \tag{5.22}$$

$$C_{sca}^{\pm} = \frac{k^4}{6\pi}(|\alpha_{ee} \pm \alpha_{eh}|^2 + |\alpha_{he} \pm \alpha_{hh}|^2) \tag{5.23}$$

The extinction cross section for a lossless reciprocal meta-atom has to be identical to the scattering cross section, i.e., due to the fact that the absorption cross section should be close to zero $C_{abs} = C_{ext} - C_{sca} = 0$.

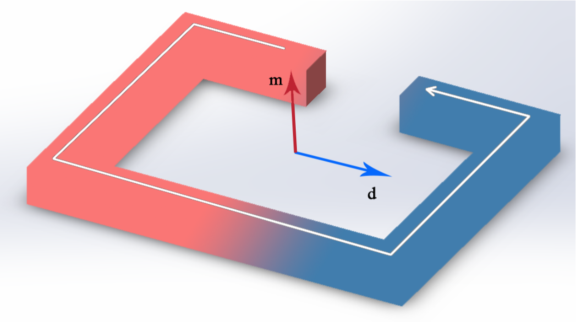

Figure 5.5: Illustration of electric and magnetic dipole moments in meta-atoms. The split resonator posses binanisotripic properties if the thickness of the ring increases.

The strength of cross-coupling terms changes with the geometrical parameters of the meta-atoms which can be optimized for this time reversal application by achieving refractive indices of ±1. The resonant frequency of meta-atoms gets perturbed by adjacent resonators which changes the radiation and decay rates of individual meta-atoms. The overall effect is that the resonant frequency changes from the fundamental frequency of the resonators. Hence, combining all the components of meta-atom design we have created a setup capable of resolving sources separated by subwavelength separation.

5.4 Importance of Asymmetry

The study of dynamics of individual components of meta-molecules composed of asymmetric rings provide a way to design a structure which can reverse the direction of magnetic dipole as required for time reversal applications. The existence of multipoles can be proved by observing the change in scattering cross-sections as function of

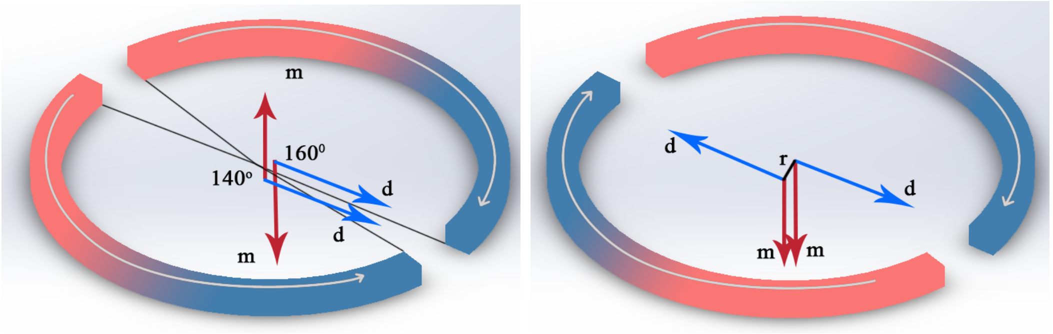

Figure 5.6: Illustration of the setup and geometry of asymmetric meta-molecule with changing mode of current oscillations.

wavelength. The over size of the meta-moelcules relative to the operating wavelength dictates the presence of higher multipole moments. The accurate distribution of current densities in the volume of the rings help tailor ohmic losses using geometry. It has been shown in literature using finite element method that losses change depending on dimensions of the ring with respect to the skin depth [126].

5.5 Conclusions

We have theoretically demonstrated a setup for low loss time reversal using bianisotropic metasurfaces. The evanescent component of the wave carrying subwavelength information couples back and forth into propagating waves due to multiple scattering. Losses are reduced by avoiding resonances and ohmic losses of metallic meta-atoms. We have analyzed the possibility of exploiting various simple shapes and geometrical parameters to reduce losses in meta-atoms. We have developed a bottom-up theoretical framework for wave propagation through bianisotropic metasurfaces. The local meta-atom design is optimized in order to achieve the required refractive index and studying the effects of interaction between adjacent meta-atoms. The local interactions can be encapsulated in the Green's functions of the metasurfaces, which along with free space Green's functions are used to analyze the system. This technique can be used to enhance the bit-rate of signals by increasing the spatial density or packing of antennas.

CHAPTER 6: CONCLUSIONS

In this dissertation, we have presented a rigorous analysis of interaction of electromagnetic waves with meta-structures of various geometries. This research is inspired by an attempt to develop a deep understanding of irregular scattering patterns observed from metallic cylindrical shells. The mathematical framework developed can be generalized for any geometry by choosing a generating function based on the shape of the boundaries. The key parameters common for interaction of electromagnetic waves with structures at meso-scale are the wavelength of the incident wavelength, the constitutive parameters of the material and the geometry of the structure. In general, structures are defined by a single size parameter and the actual shape is ignored. We have showed that the actual shape is important for designing and characterizing these interaction for tailoring the properties of metamaterials through following two main studies

- Propagation of electromagnetic waves through shell structures and implications of the resonant behavior at discrete frequencies.
- Discovered a new family of meta-atoms based on transmission enhancement due to shape resonances rather than plasmon coupling which can be used for linear and non-linear applications.
- Geometry based determination of current distribution inside the volume of the scattering object which can be used to tailor multiople moments of individual structures and associated global properties.
- Using the principles of quantum dynamics, we have developed a method to describe the temporal dynamics of interactions with localized current densities.

In chapter 2, we have presented experimental and theoretical study of scattering of waves from cylindrical shells in detail. Analyzing the data of variation of scattered fields from empty and filled cylindrical shells, we concluded that waves must interact with the contents of the shell through some mechanism. After repeating the experiments with different shells the increase in penetration of fields was attributed to possible Fabry-Perot type resonance on these structures. In order to understand the scattering mathematically, we have obtained the fields in each region by solving wave equations and the solutions in different regions were stitched together by calculating the coefficients of fields from the boundary conditions. Since, there are two boundaries we have four unknown coefficients for each mode of the fields. Hence, we have used Cramer's rule from linear algebra to solve for these coefficients from the system of equations. Plotting the relative field at the center of the shell which can be given by the coefficient of fields inside the shell as a function of frequency we discovered the presence of discrete frequencies at which the penetration increase by two order of magnitudes. The number of such frequencies increases when the dielectric constant of the medium inside the shell increases but is unaffected by the medium outside. The position of the resonance frequencies can be changed by changing the radius of the cylinders, hence combination of cylinders of different radii can be used to operate metamaterials at certain frequencies only.

This discovery has huge implications on design of meta-atoms as it opens the ability to design meta-atoms which are active at certain discrete frequencies and these frequencies are unaffected by the surrounding medium. This establishes these engineered atoms at the same footing as a natural atom as it has similar narrow and discrete response as energy levels calculated from quantum mechanics. The response of the meta-atom can be controlled at a certain frequency by the conductivity and radius of the shell and the linear, nonlinear or active core regions. We can design meta-atoms that can only response to certain frequency and we can deliver electromagnetic energy to the core region by using this phenomenon. We can also design meta-atom which can trap and localize electromagnetic energy if the core material is non-linear and shift the frequency of emitted wave away from the resonant frequency which can be used for heating applications. By carefully designing the geometry we design atoms that are responsive or "on" at certain frequencies and unresponsive or "off" at others. It can be used as a method to detect objects inside shell if we can mathematically relate the scattering pattern to the core material. In the case, where the core region has second order non-linear properties then these structure can also be used as frequency doubling atoms for discrete frequencies. Temporal dynamics can also be added to this analysis which can expand the method to study pulsed electromagnetic waves. The resonance condition shown in chapter 2 is only valid for empty cylindrical shells but similar behavior is expected from other geometries such as spheres, oblate shell if the parameters are kept in perfect harmony. In cylindrical shell the condition for TE and TM waves can be mixed by changing the angle of incidence or tilting the cylinder adding another degree of freedom.

In chapter 3, we have developed a mathematical framework which is capable of describing the propagation of electromagnetic waves through any geometry. The generating function for finite or infinite structures contain spectral variables which relate the incident wavelength to the geometrical parameters such as radius and height. This enables calculation of the field coefficients which shows the existence of resonances as a function of geometrical parameters. The main reason we are interested in propagation to electromagnetic potentials rather than fields or Hertz vectors is exploiting Aharanov-Bohm effect where the observed fields are perturbed by the shielded material without interacting with the fields. Even though it is not proved in this dissertation, using core shell geometries we should be able to design such meta-atoms by engineering the current in shell itself. The Green's function developed contains all the information about the geometry and boundary conditions of the objects, hence we can analyze the effect of structured excitation on interactions with structures.

In chapter 4, we have presented a method to analyze the current distribution within the volume of the structure and studied the dynamics of interactions of the distribution current densities with the incident fields. This leads to determination of material response $\mathbf{D}(\mathbf{r}, t)$ & $\mathbf{B}(\mathbf{r}, t)$ as a function of geometry. In general, the current distribution in a structure is limited by the skin depth but as we saw geometry can lead to enhanced transmission of fields. Hence, we have used differential geometry to introduce curvature of the structures into asymptotically decaying current inside the volume of the structure. The series is expanded in terms of a parameter Δ which is a ratio of conductivity to the permittivty and frequency of incident wave. As it is evident from the derivation the first two terms show the well known expression of skin depth but higher order term depend on the curvature. This provide a way to engineer the current density in the volume of the scattering object and engineer the multipole moments.

The interaction of adjacent meta-atoms are very important to characterize the global parameters of the metasurface or metamaterials. By decomposing the accurate current distribution related to the structure into multipole moments and analyzing the interaction of the incident fields by using principles of quantum electrodynamics, accurate dynamics can studied. The current distributions are affected by neighboring meta-atoms leading to change in decay and coupling rates. This holistic method explains uses classical and quantum electrodynamics methods to engineer the dynamics of interaction of fields with geometry based current distribution, hence is termed meta-electrodynamics.

The simplest case of to study such interactions is meta-molecule which is usually made of two meta-atoms. In chapter 5, we have illustrated an example for the methods where asymmetric meta-molecule can be used to obtain binaisotropic properties. The bianisotropic materials have a unique property where reversing the direction of magnetic dipole moments time reversal of signals can be achieved. We have not been able to show that the existence of negative index from these structure but using collective properties of individual structures we can achieve negative index of the metasurface.

We have extended the knowledge of electromagnetic wave with structure at mesoscale by rigorously introducing geometrical parameters in the electromagnetic formulation along with method inspired by quantum electrodynamics to study dynamics of the interactions. It is a significant leap forward in the design and characterization of metamaterials from common techniques such as differential Maxwell's equation solvers such as finite-difference time-domain simulations, finite-element methods, and Fourier modal methods. The results help fulfill the need to develop a better physical understanding of metamaterials in order for the area of research to mature. With the growing uncertainty about the accuracy of finite element programs, such as COMSOL to capture all physical phenomenon involved in interaction of meta-atoms with the incident field this effort is timely and can be extended to describe a wide variety of interactions and help classify various types of meta-structures as touched upon in the following sections.

6.1 Generalizability

The framework developed considers the functional dependence of permittivity and permeability making it robust and adaptable for metallic or dielectric structures. It has been shown that multipolar analysis can be used to analyze dielectric structures and interference of modes can give rise to bianisotropic properties. Accurate determination of multipole moments for metallic structures requires exact calculation of current distribution, hence dependence of skin depth on geometry. This raises an important question, are the fundamental limits to light-structure interaction dependent only on material properties or can be affected by geometrical parameters? Currently, the limits of extinction by metallic nanoparticles are independent of geometry but it can be observed that there is slight change to response for pinched tetrahedron that ellipsoid [127]. We can use the method developed here to examine the effect of geometry on fundamental limits [128] of light-structure interaction using energy conservation principles. Since the polarization density is related to current distribution in a meta-atom, can it provide a way to design effective susceptibility that could allow us to engineer the limits of interactions? We can also develop fundamental limits on power extraction from incident fields and re-radiation from bi-anisotropic meta-atoms and ensembles. By using energy-conservation principles we can set limits based on geometry of meta-atoms. These limits are essential because even for applications of radiation absorption where fluctuations in Q-factor due to interaction with neighboring structures is undesirable. Using Tretyakov's [129] approach of analyzing bi-anisotropic meta-atoms in terms of electric and magnetic dipole response as the starting point, we can start analyzing limitations of response using multipole response various structures. However, the arduous task of handling such varied geometries can be streamlined by using the formalism developed in chapter 4 and the geometrical parameters inherent in the formalism using differential geometry can be used to determine the geometry-based constitutive parameters.

6.2 Strong Non-Linearity

The results presented here can be used to demonstrate extreme non-linearity for harmonic generations at optical wavelengths. Significant advancements in fabrication techniques has led to widespread study of open nano-size optical resonators (resonant nano-antennas). Metal nano-particles capable of sustaining surface plasmon-polariton modes as well as dielectric meta-atoms with sufficiently high index of refraction to produce significant multipole response are utilized as such resonators. In case of linear and nonlinear scattering at the nanoscale for arbitrary geometries, a multipole decomposition of the scattered electromagnetic fields provides a logical interpretation for the measurable far-field characteristics, such as radiation efficiency and radiation patterns, since they are essentially determined by the interference of the excited multipole modes. Details of these multipoles which are derived from current distribution can be determined by our geometry-based method. Losses are large at optical wavelengths and attempts have been made to set fundamental limits on the responses. But analysis of such structures in the present literature is typically geometry-independent [54] which is incomplete, since the geometry is inherent in the study of structured materials.

It has been suggested that a surface discontinuity can be a source of second-harmonic generation. In multi-frequency electrical systems, nonlinear components and discontinuities in metallic contacts lead to passive intermodulation which creates signals that are harmonics of the incident frequencies [130]. This is undesirable in electric circuits and has to be removed, and there are no rigorous methods available to characterize such interactions. We can study the effects of asymmetry and discontinuities in the surface to design nonlinear properties meta-atoms using passive intermodulation techniques. There has been evidence of harmonic generation by interacting multipoles of two different meta-atoms [89, 131]. When dynamics of current density is considered the non-linear properties arise from the bulk rather than at the surface. Hence, accurate calculation of current distributions is important for engineering non-linear properties. But the theoretical model used for non-linear analysis in literature is perturbative in nature. However, designing combinations of meta-atoms to enhance certain multipolar response can lead to strong nonlinearity. Such interactions are enhanced by epsilon-near-zero (ENZ) materials [42] by concentrating light in small regions and creating high energy densities which can enhance harmonic generation. It has been shown that ENZ materials can be used to achieve large non-linearities at optical wavelengths by using indium-tin-oxide [132]. These materials can be used as a substrate for discontinuous meta-atoms to enhance harmonic generation and experiments have shown the second harmonic can be generated using magnetic dipoles [133]. We can adapt this method to enhance the non-linearity by combining such structures with epsilon-near-zero materials. Experimental studies of multipole interactions of meta-atoms are as yet nonexistent mainly because the appropriate theory is not available. Our multipole-analysis approach can provide a path forward, and an improvement over the present perturbative models. Bi-anisotropic structures can be classified as reciprocal or non-reciprocal depending on the response, which when combined with lateral radiation pattern can be used to design beam blocking surfaces.

6.3 Sources

The method proposed is a completely new way to characterize and tailor the properties of metamaterials where the interaction of incident light and structures expressed by the Lagrangian and Hamiltonian formalism with single dynamic variable with the units of charge. Current distribution in meta-structures of arbitrary geometries represented by multipole moments enabling the multipole expansion of scattered field and providing tools to tailor the collective response. This moves the state-of-the-art forward and away from computational and perturbative models for such interactions. Since the polarization density has a time and space dependent part the modes supported by the structure can directly be determined by eigenmodes corresponding to that geometry. The interaction between various modes can be leveraged to produce novel non-linear effects in materials. Exploiting the presence and lack of symmetry using group theory, inspired by classification molecules in chemistry, provides a way to classify meta-structures and maps observed function to structures. The core-shell geometry can be modified by adding a gain medium in the core which can be driven by a broadband source as the shell will ensure transmission of single frequency. In layman's terms, we should be able to design circuits which can be driven flashlights which high enough intensities.

One such area where the results can be applied is miniaturization of coherent sources which is essential in order to fill the gap between photonics and electronics. Two main problems faced in miniaturization are radiative losses due to the diffraction limit and efficient coupling of light into and out of nano-photonic sources. There has been evidence of nano-laser feasibility where optimizing the resonator geometry and the laser material has led to successful demonstration of miniaturization [134]. Recently, more exotic anapoles have been used to show generation and coupling in nano-sources [135]. The methods used in such cases have been problem-specific and are difficult to generalize. The multipole analysis developed can be generalized to develop the mathematical framework for a meta-laser as an interaction between various modes.

Presently, Maxwell-Bloch models for active nano-plasmonic metamaterials are used to describe coherent non-linear gain-plasmon dynamics [136]. These models combine the Drude-Lorentz model with Bloch model for a four-level gain system for active nano-plasmonic metamaterials. The dipole transitions are coupled to form a four-level system by adding a non-radiating carrier relaxation term. The losses can be compensated by an ultrafast pump-probe setup where both pump and probe have shorter time scales than those for which typical fluctuations become relevant. In the literature double-fishnet structures enclosing the gain material are used for demonstration of the technique. In present models, the polarizability follows a local equation of motion, driven by the incident electric field, where the decay rate determines the linewidth. The pump can be replaced by an electric pulse instead of ultrafast optical pumping for robustness and miniaturization.

Recent papers [137, 138] have shown the importance of geometry in topological insulator laser where the dynamics of lasing modes were studied using Haldane model. Analysis of localized modes due to multiple scattering in the system of rings becomes important as they do not utilize the gain medium optimally. We can to formulate gain equations and a loss analysis for a meta-atom containing a gain medium. As shown in [135] different multipoles can be made to interact to produce non-radiating modes that can be used as the resonant mechanism and presence of such modes in proximity of a gain medium can be used to design a coherent source. Hence, study of effects of dimers and trimers as the unit radiating structures appear to hold promise, with one structure as the gain medium and the other acting as the cavity resonator. This will require cavity quantum electrodynamics to accurately model such an interaction from first principles, without solely relying on numerical methods. In this analysis, the temporal dependence of interaction is very important to characterize the decay rates and linewidth of the coherent radiation produced. Studies of mode competition for such nano-sources are presently non-existent. The first test will be to formulate equations for geometry-dependent multipoles interacting with other meta-atoms to create a four-level lasing systems.

REFERENCES

[1] J. C. Maxwell, *A treatise on electricity and magnetism*, vol. 1. Clarendon press, 1881.

[2] J. A. Kong, "Theorems of bianisotropic media," *Proceedings of the IEEE*, vol. 60, pp. 1036–1046, Sept 1972.

[3] G. Mie, "Beiträge zur optik trüber medien, speziell kolloidaler metallösungen," *Ann. Phys. (Berl.)*, vol. 330, no. 3, pp. 377–445, 1908.

[4] V. G. Veselago, "The electrodynamics of substances with simultaneously negative values of ϵ and μ," *Sov. Phys. Uspekhi*, vol. 10, no. 4, p. 509, 1968.

[5] H. Lamb, "On group-velocity," *Proc. Lond. Math. Soc.*, vol. 2, no. 1, pp. 473–479, 1904.

[6] J. B. Pendry, "Negative refraction makes a perfect lens," *Phys. Rev. Lett.*, vol. 85, no. 18, p. 3966, 2000.

[7] R. A. Shelby, D. R. Smith, and S. Schultz, "Experimental verification of a negative index of refraction," *Science*, vol. 292, no. 5514, pp. 77–79, 2001.

[8] V. M. Shalaev, W. Cai, U. K. Chettiar, H.-K. Yuan, A. K. Sarychev, V. P. Drachev, and A. V. Kildishev, "Negative index of refraction in optical metamaterials," *Opt. Lett.*, vol. 30, no. 24, pp. 3356–3358, 2005.

[9] A. I. Kuznetsov, A. E. Miroshnichenko, Y. H. Fu, J. Zhang, and B. Luk'yanchuk, "Magnetic light," *Sci. Rep.*, vol. 2, p. 492, 2012.

[10] Y. Cui, K. H. Fung, J. Xu, H. Ma, Y. Jin, S. He, and N. X. Fang, "Ultrabroadband light absorption by a sawtooth anisotropic metamaterial slab," *Nano Lett.*, vol. 12, no. 3, pp. 1443–1447, 2012.

[11] C. F. Guo, T. Sun, F. Cao, Q. Liu, and Z. Ren, "Metallic nanostructures for light trapping in energy-harvesting devices," *Light Sci. Appl.*, vol. 3, no. 4, p. e161, 2014.

[12] N. Papasimakis and N. I. Zheludev, "Metamaterial-induced transparency: Sharp fano resonances and slow light," *Opt. Photonics News*, vol. 20, no. 10, pp. 22–27, 2009.

[13] N. Khizhnyak, "Artificial anisotropic dielectrics formed from 2-dimensional lattices of infinite bars and rods," *Sov. Phys. Technical Physics*, vol. 4, no. 5, pp. 539–648, 1959.

[14] D. R. Smith, J. B. Pendry, and M. C. Wiltshire, "Metamaterials and negative refractive index," *Science*, vol. 305, no. 5685, pp. 788–792, 2004.

[15] J. Valentine, S. Zhang, T. Zentgraf, E. Ulin-Avila, D. A. Genov, G. Bartal, and X. Zhang, "Three-dimensional optical metamaterial with a negative refractive index," *Nature*, vol. 455, no. 7211, p. 376, 2008.

[16] W. Cai, U. K. Chettiar, A. V. Kildishev, and V. M. Shalaev, "Optical cloaking with metamaterials," *Nat. Photonics*, vol. 1, no. 4, pp. 224–227, 2007.

[17] E. Plum, X.-X. Liu, V. Fedotov, Y. Chen, D. Tsai, and N. Zheludev, "Metamaterials: optical activity without chirality," *Phys. Rev. Lett.*, vol. 102, no. 11, p. 113902, 2009.

[18] J. Pendry, "A chiral route to negative refraction," *Science*, vol. 306, no. 5700, pp. 1353–1355, 2004.

[19] E. Plum, J. Zhou, J. Dong, V. Fedotov, T. Koschny, C. Soukoulis, and N. Zheludev, "Metamaterial with negative index due to chirality," *Phys. Rev. B*, vol. 79, no. 3, p. 035407, 2009.

[20] J. B. Pendry and D. R. Smith, "Reversing light with negative refraction," *Physics today*, vol. 57, pp. 37–43, 2004.

[21] T. J. Cui, X. Q. Lin, Q. Cheng, H. F. Ma, and X. M. Yang, "Experiments on evanescent-wave amplification and transmission using metamaterial structures," *Phys. Rev. B*, vol. 73, no. 24, p. 245119, 2006.

[22] K. L. Kelly, E. Coronado, L. L. Zhao, and G. C. Schatz, "The optical properties of metal nanoparticles: the influence of size, shape, and dielectric environment," 2003.

[23] V. A. Podolskiy, A. K. Sarychev, E. E. Narimanov, and V. M. Shalaev, "Resonant light interaction with plasmonic nanowire systems," *J. Opt. A: Pure Appl. Opt.*, vol. 7, no. 2, p. S32, 2005.

[24] A. Lagarkov and A. Sarychev, "Electromagnetic properties of composites containing elongated conducting inclusions," *Phys. Rev. B*, vol. 53, no. 10, p. 6318, 1996.

[25] U. Leonhardt, "Optical conformal mapping," *Science*, vol. 312, no. 5781, pp. 1777–1780, 2006.

[26] J. B. Pendry, D. Schurig, and D. R. Smith, "Controlling electromagnetic fields," *Science*, vol. 312, no. 5781, pp. 1780–1782, 2006.

[27] K. S. Yee, J. S. Chen, and A. H. Chang, "Conformal finite-different time-domain (FDTD) with overlapping grids," *IEEE Trans. Antennas Propag.*, vol. 40, no. 9, pp. 1068–1075, 1992.

[28] A. M. Urbas, Z. Jacob, L. Dal Negro, N. Engheta, A. Boardman, P. Egan, A. B. Khanikaev, V. Menon, M. Ferrera, N. Kinsey, *et al.*, "Roadmap on optical metamaterials," *J. Opt.*, vol. 18, no. 9, p. 093005, 2016.

[29] A. Chipouline and F. Küppers, "Analytical qualitative modeling of passive and active metamaterials," *J. Opt. Soc. Am. B*, vol. 34, no. 8, pp. 1597–1623, 2017.

[30] S. Tan and L. Tsang, "Green's functions, including scatterers, for photonic crystals and metamaterials," *J. Opt. Soc. Am. B*, vol. 34, no. 7, pp. 1450–1458, 2017.

[31] K. N. Reddy, P. Y. Chen, A. I. Fernández-Domínguez, and Y. Sivan, "Revisiting the boundary conditions for second-harmonic generation at metal-dielectric interfaces," *J. Opt. Soc. Am. B*, vol. 34, pp. 1824–1832, Sep 2017.

[32] P. Grahn, A. Shevchenko, and M. Kaivola, "Electromagnetic multipole theory for optical nanomaterials," *New J. Phys.*, vol. 14, no. 9, p. 093033, 2012.

[33] T. Niemi, A. O. Karilainen, and S. A. Tretyakov, "Synthesis of polarization transformers," *IEEE Trans. Antennas Propag.*, vol. 61, pp. 3102–3111, June 2013.

[34] X. Chen, B.-I. Wu, J. A. Kong, and T. M. Grzegorczyk, "Retrieval of the effective constitutive parameters of bianisotropic metamaterials," *Phys. Rev. E*, vol. 71, p. 046610, Apr 2005.

[35] A. E. Miroshnichenko, A. B. Evlyukhin, Y. F. Yu, R. M. Bakker, A. Chipouline, A. I. Kuznetsov, B. Luk'yanchuk, B. N. Chichkov, and Y. S. Kivshar, "Nonradiating anapole modes in dielectric nanoparticles," *Nat. Commun.*, vol. 6, p. 8069, 2015.

[36] T. Kaelberer, V. Fedotov, N. Papasimakis, D. Tsai, and N. Zheludev, "Toroidal dipolar response in a metamaterial," *Science*, vol. 330, no. 6010, pp. 1510–1512, 2010.

[37] I. Liberal and N. Engheta, "Near-zero refractive index photonics," *Nat. Photonics*, vol. 11, no. 3, p. 149, 2017.

[38] J. D. Jackson, *Classical electrodynamics.* Wiley Online Library, 1975.

[39] C. Cohen-Tannoudji, J. Dupont-Roc, and G. Grynberg, *Photons and atoms: introduction to quantum electrodynamics.* Wiley Online Library, 1989.

[40] C. M. Reinke, M. Teofilo, M. F. Su, M. B. Sinclair, and I. El-Kady, "Group-theory approach to tailored electromagnetic properties of metamaterials: An inverse-problem solution," *Physical Review E*, vol. 83, no. 6, p. 066603, 2011.

[41] C. Ciracì, E. Poutrina, M. Scalora, and D. R. Smith, "Origin of second-harmonic generation enhancement in optical split-ring resonators," *Phys. Rev. B*, vol. 85, p. 201403, May 2012.

[42] C. Argyropoulos, P.-Y. Chen, G. D'Aguanno, N. Engheta, and A. Alu, "Boosting optical nonlinearities in ε-near-zero plasmonic channels," *Physical Review B*, vol. 85, no. 4, p. 045129, 2012.

[43] A. Yariv, "Phase conjugate optics and real-time holography," *IEEE J. Quantum Electron.*, vol. 14, pp. 650–660, Sep 1978.

[44] M. Noginov, G. Zhu, A. Belgrave, R. Bakker, V. Shalaev, E. Narimanov, S. Stout, E. Herz, T. Suteewong, and U. Wiesner, "Demonstration of a spaser-based nanolaser," *Nature*, vol. 460, no. 7259, p. 1110, 2009.

[45] M. A. Fiddy and R. S. Ritter, *Introduction to imaging from scattered fields.* CRC Press, 2014.

[46] F. Lin and M. A. Fiddy, "Image estimation from scattered field data," *Int. J. Imaging Syst. Technol.*, vol. 2, no. 2, pp. 76–95, 1990.

[47] W. C. Chew, *Waves and fields in inhomogeneous media.* IEEE press, 1995.

[48] M. Born and E. Wolf, *Principles of optics: electromagnetic theory of propagation, interference and diffraction of light.* Elsevier, 2013.

[49] L. Landau, *Electrodynamics of Continuous Media.* Textbook Publishers, 2003.

[50] H. A. Wheeler, "Formulas for the skin effect," *Proceedings of the IRE*, vol. 30, no. 9, pp. 412–424, 1942.

[51] G. J. Gbur, *Mathematical methods for optical physics and engineering.* Cambridge University Press, 2011.

[52] P. M. Morse and H. Feshbach, *Methods of theoretical physics.* Technology Press, 1946.

[53] G. B. Arfken and H.-J. Weber, *Mathematical methods for physicists.* Academic Press New York 1970, 1972.

[54] O. D. Miller, A. G. Polimeridis, M. H. Reid, C. W. Hsu, B. G. DeLacy, J. D. Joannopoulos, M. Soljačić, and S. G. Johnson, "Fundamental limits to optical response in absorptive systems," *Opt. Express*, vol. 24, no. 4, pp. 3329–3364, 2016.

[55] A. Silva, F. Monticone, G. Castaldi, V. Galdi, A. Alù, and N. Engheta, "Performing mathematical operations with metamaterials," *Science*, vol. 343, no. 6167, pp. 160–163, 2014.

[56] C. Cortes, W. Newman, S. Molesky, and Z. Jacob, "Quantum nanophotonics using hyperbolic metamaterials," *J. Opt.*, vol. 14, no. 6, p. 063001, 2012.

[57] M. Fiddy, "Inversion of optical scattered field data," *J. Phys. D: Applied Physics*, vol. 19, no. 3, p. 301, 1986.

[58] J. B. Morris, F. C. Lin, D. A. Pommet, R. V. McGahan, and M. A. Fiddy, "A homomorphic filtering method for imaging strongly scattering penetrable objects," *IEEE Trans. Antennas Propag.*, vol. 43, no. 10, pp. 1029–1035, 1995.

[59] D. Colton and A. Kirsch, "A simple method for solving inverse scattering problems in the resonance region," *Inverse problems*, vol. 12, no. 4, p. 383, 1996.

[60] L. Landau and E. Lifshitz, *Electrodynamics of continuous media.* Pergamon Press, 1960.

[61] J.-S. Zhao and W. C. Chew, "Integral equation solution of Maxwell's equations from zero frequency to microwave frequencies," *IEEE Trans. Antennas Propag.*, vol. 48, no. 10, pp. 1635–1645, 2000.

[62] A. Nisbet, "Electromagnetic potentials in a heterogeneous non-conducting medium," in *Proc. Royal Soc. A: Mathematical, Physical and Engineering Sciences*, vol. 240, pp. 375–381, The Royal Society, 1957.

[63] R. Dyczij-Edlinger and O. Biro, "A joint vector and scalar potential formulation for driven high frequency problems using hybrid edge and nodal finite elements," *IEEE Trans. Microw. Theory Techn.*, no. 1, pp. 15–23, 1996.

[64] R. Dyczij-Edlinger, G. Peng, and J.-F. Lee, "A fast vector-potential method using tangentially continuous vector finite elements," *IEEE Trans. Microw. Theory Techn.*, vol. 46, no. 6, pp. 863–868, 1998.

[65] Y. Aharonov and D. Bohm, "Significance of electromagnetic potentials in the quantum theory," *Phys. Rev.*, vol. 115, no. 3, p. 485, 1959.

[66] M. Berry, R. Chambers, M. Large, C. Upstill, and J. Walmsley, "Wavefront dislocations in the Aharonov-Bohm effect and its water wave analogue," *Eur. J. Phys.*, vol. 1, no. 3, p. 154, 1980.

[67] R. Jackiw, A. Milstein, S.-Y. Pi, and I. Terekhov, "Induced current and Aharonov-Bohm effect in graphene," *Phys. Rev. B*, vol. 80, no. 3, p. 033413, 2009.

[68] K. Fang, Z. Yu, and S. Fan, "Photonic Aharonov-Bohm effect based on dynamic modulation," *Phys. Rev. Lett.*, vol. 108, no. 15, p. 153901, 2012.

[69] J. D. Jackson and L. B. Okun, "Historical roots of gauge invariance," *Rev. Mod. Phys.*, vol. 73, no. 3, p. 663, 2001.

[70] J. D. Jackson, "From Lorenz to Coulomb and other explicit gauge transformations," *Am. J. Phys.*, vol. 70, no. 9, pp. 917–928, 2002.

[71] K.-H. Yang, "The physics of gauge transformations," *Am. J. Phys.*, vol. 73, no. 8, pp. 742–751, 2005.

[72] O. Brill and B. Goodman, "Causality in the Coulomb gauge," *Am. J. Phys.*, vol. 35, no. 9, pp. 832–837, 1967.

[73] D. M. Drury, "The unification of the Lorentz and Coulomb gauges of electromagnetic theory," *IEEE Trans. Educ.*, vol. 43, no. 1, pp. 69–72, 2000.

[74] F. Liu and J. Li, "Gauge field optics with anisotropic media," *Phys. Rev. Lett.*, vol. 114, no. 10, p. 103902, 2015.

[75] K. Y. Bliokh, "Geometrodynamics of polarized light: Berry phase and spin hall effect in a gradient-index medium," *J. Opt. A: Pure Appl. Opt.*, vol. 11, no. 9, p. 094009, 2009.

[76] F. Liu, S. Wang, S. Xiao, Z. H. Hang, and J. Li, "Polarization-dependent optics using gauge-field metamaterials," *Appl. Phys. Lett.*, vol. 107, no. 24, p. 241106, 2015.

[77] A. Vedernikov, A. Govorov, and A. Chaplik, "Plasma oscillations in nanotubes and the Aharonov-Bohm effect for plasmons," *J. Exp. Theor. Phys.*, vol. 93, no. 4, pp. 853–859, 2001.

[78] Y. Gorodetski, S. Nechayev, V. Kleiner, and E. Hasman, "Plasmonic Aharonov-Bohm effect: Optical spin as the magnetic flux parameter," *Phys. Rev. B*, vol. 82, no. 12, p. 125433, 2010.

[79] O. von Roos, "Derivation of boundary conditions in electromagnetic theory," *Am. J. Phys.*, vol. 34, no. 6, pp. 535–536, 1966.

[80] M. Born and E. Wolf, *Principles of optics: electromagnetic theory of propagation, interference and diffraction of light.* Elsevier, 2013.

[81] C.-T. Tai, *Dyadic Green functions in electromagnetic theory.* Institute of Electrical & Electronics Engineers (IEEE), 1994.

[82] J. A. Stratton, *Electromagnetic theory. International series in pure and applied physics.* McGraw-Hill Book Company: New York, 1941.

[83] P. M. Morse and H. Feshbach, *Methods of theoretical physics.* Technology Press, 1946.

[84] W. Chew, *Waves and Fields in Inhomogeneous Media.* IEEE Press series on electromagnetic waves, Van Nostrand Reinhold, 1990.

[85] A. Sommerfeld, *Partial differential equations in physics*, vol. 1. Academic press, 1949.

[86] L. W. Pearson, "On the spectral expansion of the electric and magnetic dyadic Green's functions in cylindrical harmonics," *Radio Sci.*, vol. 18, no. 02, pp. 166–174, 1983.

[87] N. Chandra, "Scattering and skin depth at the meso-and nanoscale," in *High Contrast Metastructures VI*, vol. 10113, p. 101130U, International Society for Optics and Photonics, 2017.

[88] S. Jahani and Z. Jacob, "Photonic skin-depth engineering," *J. Opt. Soc. Am. B*, vol. 32, no. 7, pp. 1346–1353, 2015.

[89] D. Smirnova and Y. S. Kivshar, “Multipolar nonlinear nanophotonics,” *Optica*, vol. 3, no. 11, pp. 1241–1255, 2016.

[90] Y. Kivshar and A. Miroshnichenko, “Meta-optics with mie resonances,” *Optics and Photonics News*, vol. 28, no. 1, pp. 24–31, 2017.

[91] R. E. Raab and O. L. De Lange, *Multipole theory in electromagnetism: classical, quantum, and symmetry aspects, with applications*, vol. 128. Oxford University Press on Demand, 2005.

[92] P. J. Bruna and F. Grein, “Quadrupole, octopole, and hexadecapole electric moments of σ, π, δ, and ϕ electronic states: Cylindrically asymmetric charge density distributions in linear molecules with nonzero electronic angular momentum,” *J. Chem. Phys.*, vol. 127, no. 7, p. 074107, 2007.

[93] G. Russakoff, “A derivation of the macroscopic maxwell equations,” *Am. J. Phys.*, vol. 38, no. 10, pp. 1188–1195, 1970.

[94] F. N. H. Robinson, *Macroscopic electromagnetism*, vol. 57. Pergamon, 1973.

[95] A. Gelessus, W. Thiel, and W. Weber, “Multipoles and symmetry,” *J. Chem. Educ.*, vol. 72, no. 6, p. 505, 1995.

[96] W. Dehnen, “A fast multipole method for stellar dynamics,” *Computational Astrophysics and Cosmology*, vol. 1, no. 1, p. 1, 2014.

[97] J. Petschulat, C. Menzel, A. Chipouline, C. Rockstuhl, A. Tünnermann, F. Lederer, and T. Pertsch, “Multipole approach to metamaterials,” *Phys. Rev. A*, vol. 78, no. 4, p. 043811, 2008.

[98] A. Chipouline, J. Petschulat, A. Tuennermann, T. Pertsch, C. Menzel, C. Rockstuhl, and F. Lederer, “Multipole approach in electrodynamics of metamaterials,” *Appl. Phys. A*, vol. 103, no. 3, pp. 899–904, 2011.

[99] S. Mühlig, C. Menzel, C. Rockstuhl, and F. Lederer, “Multipole analysis of meta-atoms,” *Metamaterials*, vol. 5, no. 2-3, pp. 64–73, 2011.

[100] J. Petschulat, A. Chipouline, A. Tünnermann, T. Pertsch, C. Menzel, C. Rockstuhl, T. Paul, and F. Lederer, “Simple and versatile analytical approach for planar metamaterials,” *Phys. Rev. B*, vol. 82, no. 7, p. 075102, 2010.

[101] C. F. Bohren and D. R. Huffman, *Absorption and scattering of light by small particles*. John Wiley & Sons, 2008.

[102] E. Kreyszig, *Differential Geometry*. Heritage, University of Toronto Press, Scholarly Publishing Division, 1959.

[103] R. Da Costa, “Quantum mechanics of a constrained particle,” *Phys. Rev. A*, vol. 23, no. 4, p. 1982, 1981.

[104] H. Haddar, P. Joly, and H.-M. Nguyen, "Generalized impedance boundary conditions for scattering problems from strongly absorbing obstacles: The case of maxwell's equations," *Math. Models Meth. Appl. Sci.*, vol. 18, no. 10, pp. 1787–1827, 2008.

[105] A. Bendali and K. Lemrabet, "The effect of a thin coating on the scattering of a time-harmonic wave for the helmholtz equation," *SIAM Journal on Applied Mathematics*, vol. 56, no. 6, pp. 1664–1693, 1996.

[106] E. Faou, "Elasticity on a thin shell: Formal series solution," *Asymptotic analysis*, vol. 31, no. 3, 4, pp. 317–361, 2002.

[107] V. Fedotov, N. Papasimakis, E. Plum, A. Bitzer, M. Walther, P. Kuo, D. Tsai, and N. Zheludev, "Spectral collapse in ensembles of metamolecules," *Phys. Rev. Lett.*, vol. 104, no. 22, p. 223901, 2010.

[108] Z. Szabó, G.-H. Park, R. Hedge, and E.-P. Li, "A unique extraction of metamaterial parameters based on kramers–kronig relationship," *IEEE Trans. Microw. Theory Techn.*, vol. 58, no. 10, pp. 2646–2653, 2010.

[109] S. Savo, N. Papasimakis, and N. I. Zheludev, "Localization of electromagnetic fields in disordered metamaterials," *Phys. Rev. B*, vol. 85, no. 12, p. 121104, 2012.

[110] M. Albooyeh, V. Asadchy, R. Alaee, S. Hashemi, M. Yazdi, M. Mirmoosa, C. Rockstuhl, C. Simovski, and S. Tretyakov, "Purely bianisotropic scatterers," *Physical Review B*, vol. 94, no. 24, p. 245428, 2016.

[111] S. F. Kettle, *Symmetry and structure: readable group theory for chemists*. John Wiley & Sons, 2008.

[112] N. Liu, H. Liu, S. Zhu, and H. Giessen, "Stereometamaterials," *Nature Photonics*, vol. 3, no. 3, p. 157, 2009.

[113] W. J. Padilla, "Group theoretical description of artificial electromagnetic metamaterials," *Optics Express*, vol. 15, no. 4, pp. 1639–1646, 2007.

[114] D. Smirnova, A. I. Smirnov, and Y. S. Kivshar, "Multipolar second-harmonic generation by mie-resonant dielectric nanoparticles," *Phys. Rev. A*, vol. 97, p. 013807, Jan 2018.

[115] D. R. Jackson and D. R. Dowling, "Phase conjugation in underwater acoustics," *J. Acoust. Soc. Am.*, vol. 89, no. 1, pp. 171–181, 1991.

[116] A. Derode, P. Roux, and M. Fink, "Robust acoustic time reversal with high-order multiple scattering," *Phys. Rev. Lett.*, vol. 75, no. 23, p. 4206, 1995.

[117] G. Lerosey, J. De Rosny, A. Tourin, A. Derode, G. Montaldo, and M. Fink, "Time reversal of electromagnetic waves," *Phys. Rev. Lett.*, vol. 92, no. 19, p. 193904, 2004.

[118] N. Taket and M. Fiddy, "Theory of distortion correction by phase conjugation for strongly scattering media," *J. Opt. Soc. Am. A*, vol. 4, no. 10, pp. 1869–1872, 1987.

[119] M. Nieto-Vesperinas and E. Wolf, "Phase conjugation and symmetries with wave fields in free space containing evanescent components," *J. Opt. Soc. Am. A*, vol. 2, no. 9, pp. 1429–1434, 1985.

[120] G. Lerosey, J. De Rosny, A. Tourin, and M. Fink, "Focusing beyond the diffraction limit with far-field time reversal," *Science*, vol. 315, no. 5815, pp. 1120–1122, 2007.

[121] J. B. Pendry, "Negative refraction makes a perfect lens," *Phys. Rev. Lett.*, vol. 85, no. 18, p. 3966, 2000.

[122] J. Pendry, "A chiral route to negative refraction," *Science*, vol. 306, no. 5700, pp. 1353–1355, 2004.

[123] A. Serdiïž uïž¡kov, I. Semchenko, S. Tertyakov, and A. Sihvola, *Electromagnetics of bi-anisotropic materials-Theory and Application*, vol. 11. Gordon and Breach science publishers, 2001.

[124] S. A. Tretyakov, F. Mariotte, C. R. Simovski, T. G. Kharina, and J.-P. Heliot, "Analytical antenna model for chiral scatterers: Comparison with numerical and experimental data," *IEEE Trans. Antennas Propag.*, vol. 44, no. 7, pp. 1006–1014, 1996.

[125] W. Chew and T. Habashy, "Phase-conjugate mirror and time reversal," *J. Opt. Soc. Am. A*, vol. 2, no. 6, pp. 808–809, 1985.

[126] D. Ö. Güney, T. Koschny, and C. M. Soukoulis, "Reducing ohmic losses in metamaterials by geometric tailoring," *Phys. Rev. B*, vol. 80, no. 12, p. 125129, 2009.

[127] O. D. Miller, C. W. Hsu, M. T. H. Reid, W. Qiu, B. G. DeLacy, J. D. Joannopoulos, M. Soljačić, and S. G. Johnson, "Fundamental limits to extinction by metallic nanoparticles," *Phys. Rev. Lett.*, vol. 112, p. 123903, Mar 2014.

[128] D. O. Güney, T. Koschny, and C. M. Soukoulis, "Reducing ohmic losses in metamaterials by geometric tailoring," *Phys. Rev. B*, vol. 80, p. 125129, Sep 2009.

[129] Y. Ra'di and S. A. Tretyakov, "Balanced and optimal bianisotropic particles: maximizing power extracted from electromagnetic fields," *New J. Phys.*, vol. 15, no. 5, p. 053008, 2013.

[130] P. Lui, "Passive intermodulation interference in communication systems," *Electronics & Communication Engineering Journal*, vol. 2, no. 3, pp. 109–118, 1990.

[131] Y. Yang, W. Wang, A. Boulesbaa, I. I. Kravchenko, D. P. Briggs, A. Puretzky, D. Geohegan, and J. Valentine, “Nonlinear fano-resonant dielectric metasurfaces,” *Nano Lett.*, vol. 15, no. 11, pp. 7388–7393, 2015.

[132] M. Z. Alam, I. De Leon, and R. W. Boyd, “Large optical nonlinearity of indium tin oxide in its epsilon-near-zero region,” *Science*, vol. 352, no. 6287, pp. 795–797, 2016.

[133] I. Kolmychek, A. Y. Bykov, E. Mamonov, and T. Murzina, “Second-harmonic generation interferometry in magnetic-dipole nanostructures,” *Opt. letters*, vol. 40, no. 16, pp. 3758–3761, 2015.

[134] M. Khajavikhan, A. Simic, M. Katz, J. Lee, B. Slutsky, A. Mizrahi, V. Lomakin, and Y. Fainman, “Thresholdless nanoscale coaxial lasers,” *Nature*, vol. 482, no. 7384, p. 204, 2012.

[135] J. S. T. Gongora, A. E. Miroshnichenko, Y. S. Kivshar, and A. Fratalocchi, “Anapole nanolasers for mode-locking and ultrafast pulse generation,” *Nat. Commun.*, vol. 8, p. 15535, 2017.

[136] S. Wuestner, A. Pusch, K. L. Tsakmakidis, J. M. Hamm, and O. Hess, “Gain and plasmon dynamics in active negative-index metamaterials,” *Philosophical Transactions of the Royal Society of London A: Mathematical, Physical and Engineering Sciences*, vol. 369, no. 1950, pp. 3525–3550, 2011.

[137] G. Harari, M. A. Bandres, Y. Lumer, M. C. Rechtsman, Y. Chong, M. Khajavikhan, D. N. Christodoulides, and M. Segev, “Topological insulator laser: Theory,” *Science*, p. eaar4003, 2018.

[138] M. A. Bandres, S. Wittek, G. Harari, M. Parto, J. Ren, M. Segev, D. N. Christodoulides, and M. Khajavikhan, “Topological insulator laser: Experiments,” *Science*, p. eaar4005, 2018.

[139] M. Fox, *Optical properties of solids*, vol. 3. Oxford university press, 2010.

APPENDIX A: CALCULATION OF TRADITIONAL SKIN DEPTH

There are a variety of ways to calculate the expression for skin depth in literature but here we will derive the expression using free carrier conductivity method using the formulation in Ref. [139]. For an electron with charge $-e$, mass $m_0$and damping factor Γ under the excitation $\mathbf{E} = E_0 e^{-i\omega t}$

$$m_0 \frac{\partial^2 x}{\partial t^2} + m_0 \Gamma \frac{\partial x}{\partial t} = -e\mathbf{E} \tag{A.1}$$

Using, the definition of momentum $m_0 \frac{\partial x}{\partial t} = \mathbf{p}$, we get

$$\frac{\partial \mathbf{p}}{\partial t} = -\frac{\mathbf{p}}{\tau} - e\mathbf{E} \tag{A.2}$$

where, damping rate Γ by $1/\tau$, where τ is the damping time. This shows that electrons accelerated by electric fields losses momentum in the momentum scattering time τ. For a field with harmonic time dependence, the variation of position also has harmonic time dependence, $\frac{\partial \mathbf{x}}{\partial t} = \mathbf{v} = \mathbf{v}_0 e^{-i\omega t}$. Upon substitution in equation of motion,

$$\mathbf{v}(t) = \frac{-e\tau}{m_0} \frac{1}{1 - i\omega\tau} \mathbf{E} \tag{A.3}$$

The current density $\mathbf{j}$ for N electrons per unit volume is related to the field through conductivity

$$\mathbf{j} = -Ne\mathbf{v} = \sigma \mathbf{E} \tag{A.4}$$

Thus, using the expression for $\mathbf{v}$, we frequency dependent expression for conductivity $\sigma(\omega)$ in terms of DC conductivity $\sigma_0 = \frac{Ne^2\tau}{m_0}$,

$$\sigma(\omega) = \frac{\sigma_0}{1 - i\omega\tau} \tag{A.5}$$

For a typical metal or doped semiconductor, the value of τ at room temperature varies from 10^{-14} to 10^{-13}. Using the definition of electric displacement,

$$\mathbf{D} = \epsilon_0 \mathbf{E} + \mathbf{P} \tag{A.6}$$

the expression for relative permittivity ϵ_r can be obtained

$$\epsilon_r(\omega) = 1 + \frac{i\sigma(\omega)}{\epsilon_0 \omega} \tag{A.7}$$

which is the exact expression obtained from the waveumber in chapter 2. For frequencies which satisfy the relation $\omega\tau << 1$, the relative permittivity can be split into real and imaginary parts $\epsilon_r = \epsilon_1 + i\epsilon_2$. This leads to the imaginary part being grater than the real part and the absorption (α) can be approximated as

$$\alpha = \frac{2\omega(\epsilon_2/2)^{\frac{1}{2}}}{(\epsilon_0\mu_0)^2} = (2\sigma_0\omega\mu_0)^{\frac{1}{2}} \tag{A.8}$$

The strength field inside a conductor varies as $e^{-\frac{z}{\delta_s}}$, and power falls as $e^{-\frac{2z}{\delta_s}}$ giving rise to skin depth.

$$\delta_s = \frac{2}{\alpha} = \sqrt{\frac{2}{\sigma_0\omega\mu_0}} \tag{A.9}$$

APPENDIX B: MANIPULATION OF BESSEL FUNCTIONS

As it is evident from the derivations in chapter 2 that the Bessel functions of first and second kind and their derivatives required has to be analyzed. In this series expansion we will follow the notation from Ref. [51]. The argument of the Bessel and Hankel functions can be real and imaginary, hence the argument x has to be general complex. Using Bessel's differential equation of order m is given by the expression

$$x^2 R''(x) + xR'(x) + (x^2 - m^2)R(x) = 0 \tag{B.1}$$

Frobenius method can be used to find the series solution of Bessel's equation

$$J_m(x) = \sum_{n=0}^{\infty} \frac{(-1)^n}{n!(n+m)!} (\frac{x}{2})^{2n+m} \qquad m = 0, 1, 2 \cdots \tag{B.2}$$

Using the series expansion for J_m and J_{-m}, the series expansion for Bessel function of second kind can be derived.

$$\begin{aligned} N_m(x) = {} & \frac{2}{\pi}[\gamma + ln(\frac{x}{2})]J_m(x) - \frac{1}{\pi}\sum_{n=0}^{m-1} \frac{(n-m-1)!}{n!}(\frac{x}{2})^{-m+2n} \\ & -\frac{1}{\pi}\sum_{n=1}^{\infty} \frac{(-1)^n}{(n+m)!n!}[\sum_{k=0}^{n}(\frac{1}{k} + \frac{1}{m+k})](\frac{x}{2})^{m+2n} \end{aligned} \tag{B.3}$$

where γ is the so-called Euler-Mascheroni constant which is defined as,

$$\gamma \equiv \lim_{N\to\infty} (\sum_{k=1}^{N} \frac{1}{k} - lnN) \tag{B.4}$$

In the case of $m = 0$ the second term in equation B.3 is not present and negative index Bessel function is defined as,

$$J_{-m}(x) = (-1)^m J_m(x) \tag{B.5}$$

$$N_{-m}(x) = (-1)^m N_m(x) \tag{B.6}$$

The presence of metals makes the wave vector complex which leads to first derivative of Hankel function not converge to zero when the complex number becomes large. Calculations performed using SciPY of Python have shown that derivative of Hankel function of second kind will become extermely large for an argument $699 + i697$ giving an output of $4.9569805312926237 \times 10^{-300} - i1.1818047444764686e \times 10^{-301}$ and becoming a non-number immediately afterwards. This makes it imperative to use the series solutions of Bessel's functions to prevent the function from becoming extremely small by carefully terminating the series after required number of terms. Assuming a general complex argument $x = re^{i\theta}$ for the Bessel's functions and the values become extremely large when the magnitude of $|x| \leq 10$, the series expansion will be used and asymptotic expansion can be utilized for $|x| > 10$. Substituting the complex notation in the series expansions, making the real $\Re(\cdot)$ and imaginary $\Im(\cdot)$ parts

$$\Re[J_m(x)] = \sum_{n=0}^{\infty} \frac{(-1)^n}{n!(n+m)!} (\frac{r}{2})^{2n+m} \cos[(2n+m)\theta] \tag{B.7}$$

$$\Im[J_m(x)] = \sum_{n=0}^{\infty} \frac{(-1)^n}{n!(n+m)!} (\frac{r}{2})^{2n+m} \sin[(2n+m)\theta] \tag{B.8}$$

The series has to be truncated such that the value of the Bessel function to keep the error to a minimum. Let us analyze $J_0(x)$ and $J_1(x)$ truncated to 30 terms, the maximum error for this approximation is of the order 1.23×10^{-23} for $J_0(x)$ and 1.99×10^{-24} for $J_1(x)$. Now, for real and imaginary parts of zeroth and first order Neumann functions for complex arguments becomes

$$\Re[N_0(x)] = \frac{2}{\pi}[\Re[J_0(x)](\gamma+ln(\frac{r}{2}))-\theta\Im[J_0(x)]-\sum_{n=1}^{\infty}\frac{(-1)^n r^{2n}}{2^{2n}(n!)^2}\sum_{k=0}^{30}(\frac{1}{k})\cos(2n\theta)] \tag{B.9}$$

$$\Im[N_0(x)] = \frac{2}{\pi}[\Im[J_0(x)](\gamma+ln(\frac{r}{2}))-\theta\Re[J_0(x)]-\sum_{n=1}^{\infty}\frac{(-1)^n r^{2n}}{2^{2n}(n!)^2}\sum_{k=0}^{30}(\frac{1}{k})\sin(2n\theta)] \tag{B.10}$$

$$\begin{aligned}\Re[Y_1(x)] = {} & \frac{2}{\pi}[\Re[J_1(x)](\gamma+ln(\frac{r}{2}))-\theta\Im[J_1(x)]-\frac{1}{r}\cos\theta \\ & -\sum_{n=1}^{\infty}\frac{(-1)^n r^{2n+1}}{2^{2n+2}(n!)^2}\sum_{k=0}^{30}(\frac{1}{k}+\frac{1}{k+1})\cos((2n+1)\theta)]\end{aligned} \tag{B.11}$$

$$\begin{aligned}\Im[N_1(x)] = {} & \frac{2}{\pi}[\Im[J_1(x)](\gamma+ln(\frac{r}{2}))-\theta\Re[J_1(x)]+\frac{1}{r}\sin\theta \\ & -\sum_{n=1}^{\infty}\frac{(-1)^n r^{2n+1}}{2^{2n+2}(n!)^2}\sum_{k=0}^{30}(\frac{1}{k}+\frac{1}{k+1})\sin((2n+1)\theta)]\end{aligned} \tag{B.12}$$

Trucntaing the series for Bessel's function of second kind to 30 terms makes the value of $\gamma = 0.593789618$.

For large values of the argument of Bessel's functions, asymptotic expansion is used, given below in terms of Γ function

$$\begin{aligned}J_m(x) \approx {} & \sqrt{\frac{2}{\pi x}}[\cos(x-\frac{m\pi}{2}-\frac{\pi}{4})\sum_{n=0}^{\infty}\frac{(-1)^n}{(2n)^{2n}}\frac{\Gamma(m+2n+1/2)}{n!\Gamma(m-2n+\frac{1}{2})} \\ & -\sin(x-\frac{m\pi}{2}-\frac{\pi}{4})\sum_{n=0}^{\infty}\frac{(-1)^n}{(2n)^{2n+1}}\frac{\Gamma(m+(2n+1)+1/2)}{n!\Gamma(m-(2n+1)+\frac{1}{2})}]\end{aligned} \tag{B.13}$$

$$N_m(x) \approx \sqrt{\frac{2}{\pi x}}[\sin(x - \frac{m\pi}{2} - \frac{\pi}{4})\sum_{n=0}^{\infty}\frac{(-1)^n}{(2n)^{2n}}\frac{\Gamma(m+2n+1/2)}{n!\Gamma(m-2n+\frac{1}{2})}$$
$$+\cos(x - \frac{m\pi}{2} - \frac{\pi}{4})\sum_{n=0}^{\infty}\frac{(-1)^n}{(2n)^{2n+1}}\frac{\Gamma(m+(2n+1)+1/2)}{n!\Gamma(m-(2n+1)+\frac{1}{2})}] \tag{B.14}$$

Thus, the Hankel functions becomes

$$H_m^{(1)}(x) \approx \sqrt{\frac{2}{\pi x}}e^{i(x-\frac{m\pi}{2}-\frac{\pi}{4})}\sum_{n=0}^{\infty}\frac{(\frac{1}{2}-m)n\Gamma(m+n+\frac{1}{2})}{m!\Gamma(m+\frac{1}{2})(2ix)^n} \tag{B.15}$$

$$H_m^{(2)}(x) \approx \sqrt{\frac{2}{\pi x}}e^{-i(x-\frac{m\pi}{2}-\frac{\pi}{4})}\sum_{n=0}^{\infty}\frac{(\frac{1}{2}-m)n\Gamma(m+n+\frac{1}{2})}{m!\Gamma(m+\frac{1}{2})(-2ix)^n} \tag{B.16}$$

The derivatives of these functions can be derived from recurrence relations,

$$J_0'(x) = -J_1(x) \qquad J_n'(x) = J_{n-1}(x) - \frac{n}{2}J_n(x) \qquad n = 1, 2, 3\cdots \tag{B.17}$$

$$N_0'(x) = -N_1(x) \qquad N_n'(x) = N_{n-1}(x) - \frac{n}{2}N_n(x) \qquad n = 1, 2, 3\cdots \tag{B.18}$$

$$H_0'(x) = -H_1(x) \qquad H_n'(x) = H_{n-1}(x) - \frac{n}{2}H_n(x) \qquad n = 1, 2, 3\cdots \tag{B.19}$$

Applying stationary phase approximation and for large values of the arguments x Bessel's functions can be further simplified without loosing much accuracy

$$J_m(x) \approx \sqrt{\frac{2}{\pi x}}[\cos(x - \frac{m\pi}{2} - \frac{\pi}{4})] \tag{B.20}$$

To simplify the analysis of complex numbers we can use Euler's formula

$$J_m(x) \approx \sqrt{\frac{1}{2\pi x}}[e^{i(x-\frac{m\pi}{2}-\frac{\pi}{4})} + e^{-i(x-\frac{m\pi}{2}-\frac{\pi}{4})}] \tag{B.21}$$

Hence Hankel function is given by

$$H_m^{(1)}(x) \approx \sqrt{\frac{2}{\pi x}} e^{i(x-\frac{m\pi}{2}-\frac{\pi}{4})} \tag{B.22}$$

$$H_m^{(2)}(x) \approx \sqrt{\frac{2}{\pi x}} e^{-i(x-\frac{m\pi}{2}-\frac{\pi}{4})} \tag{B.23}$$

APPENDIX C: HELMHOLTZ THEOREM

An arbitrary vector $\boldsymbol{\psi}(\mathbf{r})$ can be decomposed into the sum of two vector fields, one with zero divergence and another with zero curl.

$$\boldsymbol{\psi}(\mathbf{r}) = \boldsymbol{\psi}_\perp(\mathbf{r}) + \boldsymbol{\psi}_\parallel(\mathbf{r}) \tag{C.1}$$

where,

$$\nabla \cdot \boldsymbol{\psi}_\perp(\mathbf{r}) = 0 \qquad \textit{and} \qquad \nabla \times \boldsymbol{\psi}_\parallel(\mathbf{r}) = 0 \tag{C.2}$$

In order to analyze the electromagnetic potentials and fields the vector field can be written as

$$\boldsymbol{\psi}(\mathbf{r}) = \nabla \times \mathbf{A}(\mathbf{r}) - \nabla\Phi(\mathbf{r}) \tag{C.3}$$

Both $\mathbf{A}(\mathbf{r})$ and $\Phi(\mathbf{r})$ can be derived uniquely using integration over entire three dimensional space which is valid for both static and time dependent vector fields.

$$\phi(\mathbf{r}) = \frac{1}{4\pi}\int d^3r' \frac{\nabla' \cdot \mathbf{C}(\mathbf{r}')}{|\mathbf{r} - \mathbf{r}'|} \tag{C.4}$$

$$\mathbf{A}(\mathbf{r}) = \frac{1}{4\pi}\int d^3r' \frac{\nabla' \times \mathbf{C}(\mathbf{r}')}{|\mathbf{r} - \mathbf{r}'|} \tag{C.5}$$

Using properties of delta function

$$\boldsymbol{\psi}(\mathbf{r}) = \int d^3r' \boldsymbol{\psi}(\mathbf{r}')\delta(\mathbf{r} - \mathbf{r}') = -\frac{1}{4\pi}\int d^3r' \boldsymbol{\psi}(\mathbf{r}')\nabla^2 \frac{1}{|\mathbf{r} - \mathbf{r}'|} \tag{C.6}$$

Exchanging $\boldsymbol{\psi}(\mathbf{r}')$ and ∇^2 in the last term and using the identity $\nabla \times \nabla = \nabla(\nabla\cdot) - \nabla^2$

$$\boldsymbol{\psi}(\mathbf{r}) = -\frac{1}{4\pi}\int d^3r'\nabla\cdot[\frac{\boldsymbol{\psi}(\mathbf{r}')}{|\mathbf{r}-\mathbf{r}'|}] + \frac{1}{4\pi}\nabla\times\int d^3r'\nabla\times[\frac{\boldsymbol{\psi}(\mathbf{r}')}{|\mathbf{r}-\mathbf{r}'|}] \tag{C.7}$$

Using $\nabla f(|\mathbf{r}-\mathbf{r}'|) = \nabla' f(|\mathbf{r}-\mathbf{r}'|)$

$$\nabla'\cdot[\frac{\boldsymbol{\psi}(\mathbf{r}')}{|\mathbf{r}-\mathbf{r}'|}] = \frac{\nabla'\cdot\boldsymbol{\psi}(\mathbf{r}')}{|\mathbf{r}-\mathbf{r}'|} - \boldsymbol{\psi}(\mathbf{r}')\cdot\nabla\frac{1}{|\mathbf{r}-\mathbf{r}'|} \tag{C.8}$$

After moving $\boldsymbol{\psi}(\mathbf{r}')$ to the right of ∇ in the last term and rearranging terms

$$\nabla\cdot[\frac{\boldsymbol{\psi}(\mathbf{r}')}{|\mathbf{r}-\mathbf{r}'|}] = \frac{\nabla'\cdot\boldsymbol{\psi}(\mathbf{r}')}{|\mathbf{r}-\mathbf{r}'|} - \nabla'\cdot\frac{\boldsymbol{\psi}(\mathbf{r}')}{|\mathbf{r}-\mathbf{r}'|} \tag{C.9}$$

Similarly,

$$\nabla\times[\frac{\boldsymbol{\psi}(\mathbf{r}')}{|\mathbf{r}-\mathbf{r}'|}] = \frac{\nabla'\times\boldsymbol{\psi}(\mathbf{r}')}{|\mathbf{r}-\mathbf{r}'|} - \nabla'\times\frac{\boldsymbol{\psi}(\mathbf{r}')}{|\mathbf{r}-\mathbf{r}'|} \tag{C.10}$$

Inserting equations C.9 and C.10 in equation C.7, we get

$$\begin{aligned}\boldsymbol{\psi}(\mathbf{r}) = -\frac{1}{4\pi}\nabla\int d^3r'\frac{\nabla'\cdot\boldsymbol{\psi}(\mathbf{r}')}{|\mathbf{r}-\mathbf{r}'|} + \frac{1}{4\pi}\nabla\times\int d^3r'\frac{\nabla'\times\boldsymbol{\psi}(\mathbf{r}')}{|\mathbf{r}-\mathbf{r}'|}\\ +\frac{1}{4\pi}\nabla\int d^3r'\nabla'\cdot\frac{\boldsymbol{\psi}(\mathbf{r}')}{|\mathbf{r}-\mathbf{r}'|} - \frac{1}{4\pi}\nabla\times\int d^3r'\nabla'\times\frac{\boldsymbol{\psi}(\mathbf{r}')}{|\mathbf{r}-\mathbf{r}'|}\end{aligned} \tag{C.11}$$

The last two terms reduce to zero when first two integrals converge and using divergence theorem changes volume integral to surface integral with the surface of integrals at infinity.

$$\int d\mathbf{S}'\cdot\frac{\boldsymbol{\psi}(\mathbf{r}')}{|\mathbf{r}-\mathbf{r}'|} \tag{C.12}$$

and

$$\int d\mathbf{S}'\times\frac{\boldsymbol{\psi}(\mathbf{r}')}{|\mathbf{r}-\mathbf{r}'|} \tag{C.13}$$

APPENDIX D: LIST OF PUBLICATIONS

1. **N. Chandra**, “Time Reversal using multipole method for bianisotropic metasurfaces." *being prepared for J. Opt. Soc. Am. A*.
2. **N. Chandra**, “Skin depth enhancement in cylindrical shells." *being prepared for J. Opt. Soc. Am. A*.
3. **N. Chandra**, “Electromagnetic potentials across a general boundary." *Re-submitted to J. Opt. Soc. Am. A*.
4. **N. Chandra**, “Time Reversal using Bianisotropic Metasurfaces." *In Mathematics in Imaging*, Optical Society of America, 2018.
5. [Invited Paper] **N. Chandra**, “Low-loss bianisotropic metamaterials for time reversal." In High Contrast Metastructures VII, vol. 10542, p. 1054208. International Society for Optics and Photonics, 2018.
6. **N. Chandra**, “Inverse scattering method to design or determine properties of metamaterials." *In Frontiers in Optics*, pp. JW3A-88. Optical Society of America, 2017.
7. **N. Chandra**, “Effects of Geometry on Scattering." *In Mathematics in Imaging*, pp. MW4C-2. Optical Society of America, 2017.
8. **N. Chandra**, “Dictionary based approach to edge detection." *In Mathematics in Imaging*, pp. MW2C-2. Optical Society of America, 2017.
9. **N. Chandra**, “Scattering and skin depth at the meso-and nanoscale." In High Contrast Metastructures VI, vol. 10113, p. 101130U. International Society for Optics and Photonics, 2017.

APPENDIX E: LIST OF PRESENTATIONS

1. **N. Chandra**, “Inverse Scattering Approach to measure $\epsilon(\mathbf{r})$ and $\mu(\mathbf{r})$." Center for Metamaterials IAB meeting, May 2018.
2. **N. Chandra**, “Analog time reversal using bianisotropic metasurfaces." Center for Metamaterials IAB meeting, May 2018.
3. **N. Chandra**, “The goals and achievements of Center for Metamaterials." NSF Biennial meeting July 2017.
4. **N. Chandra**, “Inverse Scattering Approach to measure $\epsilon(\mathbf{r})$ and $\mu(\mathbf{r})$." Center for Metamaterials IAB meeting, October 2017
5. **N. Chandra**, “Analog time reversal using bianisotropic metasurfaces." Center for Metamaterials IAB meeting, October 2017
6. **N. Chandra**, “Inverse Scattering Approach to measure ϵ and μ." Center for Metamaterials IAB meeting, April 2017
7. **N. Chandra**, “Sub-wavelength packing of antennas/far field HR imaging." Center for Metamaterials IAB meeting, April 2017.
8. **N. Chandra**, “Ring Resonator Sensor Array." Center for Metamaterials IAB meeting, April 2017.
9. **N. Chandra** and M. A. Fiddy, “Inverse Scattering Approach to measure ϵ and μ." Center for Metamaterials IAB meeting, October 2016.